GaInN/GaN Schottky Barrier Solar Cells

Kevin T. Chern

Dissertation submitted to the faculty of the Virginia Polytechnic Institute and State University in partial fulfillment of the requirements for the degree of

Doctor of Philosophy

In

Electrical Engineering

Louis J. Guido

Levon Asryan

Gary Brown

Guo-Quan Lu

Khai Ngo

April 6, 2015

Blacksburg, Virginia

Key Words: GaInN, Semiconductor Solar Cell, Schottky Diode, Transparent Conducting Oxide

GaInN/GaN Schottky Barrier Solar Cells

Kevin T. Chern

Abstract

GaInN has the potential to revolutionize the solar cell industry, enabling higher efficiency solar cells with its wide bandgap range spanning the entire solar spectrum. However, material quality issues stemming from the large lattice mismatch between its binary endpoints and questionable range of p-type doping has thus far prevented realization of high efficiency solar cells. Nonetheless, amorphous and multi-crystalline forms of GaInN have been theorized to exhibit a defect-free bandgap, enabling GaInN alloys at any indium composition to be realized. But the range of possible p-type doping has not yet been determined and no device quality material has been demonstrated thus far. Nonetheless, a Schottky barrier design (to bypass the p-type doping issue) on single-crystal GaInN can be used to provide some insight into the future of amorphous and micro-crystalline GaInN Schottky barrier solar cells. Through demonstration of a functional single crystalline GaInN Schottky barrier solar cell and comparison of the results to the best published reports for more conventional p-i-n GaInN solar cells, this work aims to establish the feasibility of amorphous and multi-crystalline GaInN solar cells.

Acknowledgements

I would like to thank the following people and companies for their contributions to my work at Virginia Tech. Completing this enormous amount of research would not have been possible without their support.

- Dr. Louis Guido, my advisor and friend who has taught me so much about the ways of Graduate school and life. His advice and suggestions were invaluable to overcoming any obstacle encountered in my research work.

- The members of my committee, Dr. Levon Asryan, Dr. Gary Brown, Dr. Guo-Quan Lu, and Dr. Khai Ngo, for their different perspectives and extremely helpful advice with the writing of this work.

- Noah, AJ, Tim, and the other members of Dr. Guido's research group whose work was critical to the completion of this work.

- Don whose assistance with device fabrication and equipment greatly helped with the many hours spent in the clean room.

- Kopin Corperation for their generous donation of the solar cell material structure, MicroLink Devices for calibrated solar cell measurements, and 4Wave for optical measurements on the transparent films.

- My girlfriend, Evelyn, whose constant love helped me through the best and worst of times and kept me on a focus for completion.

- All of my friends whose support has helped me keep my sanity and my life together.

- My family whose financial support and constant reminders have helped me stay on top of the ball game. My father, SJ, for his advice and help through the most difficult situations; my mother, Jin-Jy, for her constant encouragement and love; and my sister, Connie, for her ability to keep a smile on my face.

- And all of the many others who helped me during my time at Virginia Tech.

TABLE OF CONTENTS

LIST OF FIGURES

x

LIST OF TABLES

1. INTRODUCTION

1.1 Case for Solar Energy Conversion

Global warming has recently become a major concern with rising temperatures resulting in increased sea levels due to glacier melt and impact on ecosystems sensitive to temperature fluctuations. One major contribution to global warming has been greenhouse gas emissions, often released as a byproduct of carbon based energy generation. In the United States, emissions resulting from energy production are the largest source of greenhouse gasses [1], accounting for 32% of current emissions. Pressure to cut back on greenhouse emissions continues to increase as direct consequences of the increased temperatures have already been reported. A recent observation by National Aeronautics and Space Administration (NASA) stated that the Amundsen Sea Antarctic glacier is no longer grounded due to increasing temperatures and is now sliding towards the ocean potentially resulting in a four foot sea ocean rise [2]. The switch to cleaner energy sources needs to happen quickly to help stem the impact of greenhouse gasses before permanent global change arises from an increase in temperatures.

The largest energy source available on Earth is the sun. The total energy incident on earth from the sun is approximately 650×10^{18} kW-hour [3], significantly greater than the total energy generation capability of the entire world in 2011 (21.1×10^{15} kW-hour) as reported by the US Energy Information Administration [4]. However, actual worldwide solar energy production in 2011 only amounted to 96×10^{12} kW-hour, accounting for significantly less than a single percent of total energy generation and an even smaller fraction of the total energy that could be harvested from the sun. With such a tremendous and ubiquitous energy source, more effort should be devoted to harvesting this essentially free energy.

1.2 Classification of Solar Cell R&D

Solar cell research can be split into three classifications, each of which have focused on different aspects of the performance/cost tradeoff. These classifications can be summarized by their area of focus:

- Class 1: Low cost solar cells with adequate efficiency where low cost is the driving factor, found in the form of large-area solar panels installed on buildings to augment traditional electrical power generation, or as compact photovoltaic modules used to energize portable electronic devices.

- Class 2: High efficiency solar cells regardless of cost, typically used for power generation on satellites where the weight reduction due to higher efficiency coupled with a much larger project budget can finance more expensive power sources.

- Class 3: A merger of the previous two generations to realize solar cells with high energy conversion efficiency at lower cost.

Class 1 solar cells are manufactured using inexpensive raw materials consistent with the emphasis on cost reduction. Contemporary materials include Si, CdTe, and $CuIn_{1-x}Ga_xSe_2$ (CIGS), with individual research-grade solar cells having efficiencies in the 10-20% range. All Class 1 solar cells share a common trait in that their semiconductor absorbers are made from either polycrystalline or amorphous materials to reduce the cost of manufacturing. Such materials can by synthesized at very high growth rates (many microns per hour) using chemical solution baths, chemical vapor deposition, or other low-cost techniques.

In contrast, Class 2 solar cells require nearly perfect crystalline structure and the highest chemical purity, with material growth carried out under very tightly controlled conditions. These solar cell materials are commonly prepared using advanced thin-film growth methods, such as

metal organic chemical vapor deposition (MOCVD) or molecular beam epitaxy (MBE), which require expensive metal-organic liquid and highly toxic hydride gas sources or very pure metals, respectively. Moreover, relatively slow deposition rates must be used to prepare the highest quality semiconductor films (1-2 microns per hour for MOCVD and 0.2-0.5 microns per hour for MBE). Class 2 solar cells are also characterized by their complex device architecture: the highest efficiency solar cells employ multi-junction (MJ) designs, simultaneously utilizing different III-V compounds such as GaAs, InGaP, and InGaAs to boost efficiency through spectral matching of bandgaps to the appropriate solar spectrum. The higher complexity involving many different absorber materials combined with low growth rate, high purity sources, and expensive deposition equipment drives up manufacturing cost. As such, these solar cells are only used in applications where the total project budget is considerably larger than the cost of the solar cell. However, the performance of these solar cells is unmatched with typical module-level efficiencies greater than 30% and hand-picked research cells reaching 44% under concentrated solar light [5].

Class 3 solar cells are supposed to bridge the gap in cost and efficiency between the other two classifications. Ideally, this could be achieved by utilizing low-cost synthesis techniques to make polycrystalline absorber materials (Class 1) with different bandgaps and stacking these individual cells into multi-junction designs (Class 2). However, in practice this approach is limited by the range of available bandgaps (E_G) associated with conventional semiconductor materials, which in turn impacts the maximum achievable efficiency for such solar cells.

1.3 Potential of GaInN Materials

GaInN semiconductor alloys have emerged over the past ten years as a candidate Class 3 solar cell material, primarily because of the revised bandgap of InN [6-8]. A MJ solar cell made solely

out of GaInN absorber materials, with bandgaps ranging from 0.7 to 3.4 eV, would theoretically span the entire solar spectrum as shown in Figure 1.1. GaInN alloys also exhibit near bandgap absorption coefficients up to an order of magnitude larger than semiconductors used in present-generation high efficiency solar cells [9]. Large absorption coefficients enable structures with much thinner layers, thereby decreasing the cost associated with material growth.
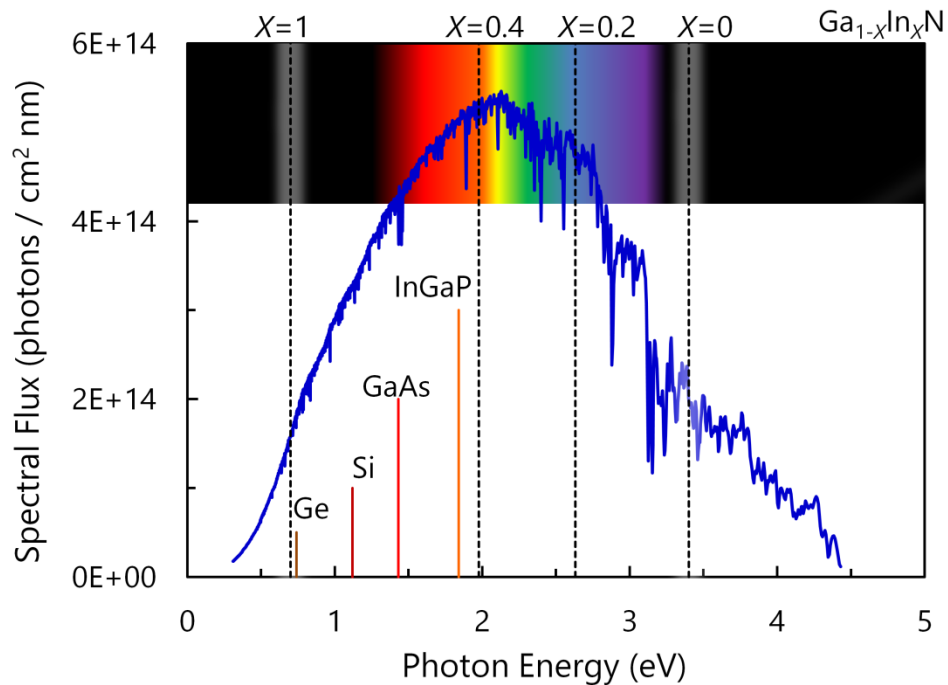
Figure 1.1. Photon Energy vs. Spectral Flux plot of the AM1.5G solar spectrum. The bandgaps Ge, Si, GaAs, and InGaP (vertical solid lines extending from bottom) representing materials commonly found in solar cells, are compared against the bandgaps of different compositions of $Ga_{1-x}In_xN$ (vertical dotted lines).

GaInN is very robust compared to other materials when subjected to high energy radiation showing orders of magnitude more radiation hardness. Consequently, GaInN MJ solar cells should fare better in space for satellite applications where the amount of overprovisioning required to guarantee sufficient power generation over the course of the mission could be decreased, yielding a direct weight savings from fewer solar panels [10-12]. GaInN solar cells

have also proven to be useful well above room temperature; early designs show an increase in efficiency with temperature up to 100 ℃ as well as good rectifying behavior at up to 330 ℃. These observations suggest that even higher temperature operation may be possible [13]. In contrast, Si based solar cells do not operate well beyond 80 ℃ and existing III-V compound MJ solar cells do not function well above 200 ℃.

2. PROBLEM STATEMENT

2.1 Rationale for Study

The class of materials known as group-III nitride semiconductors suffers from a number of well documented problems which have thus far prevented solar cells made thereof from being competitive with existing technology. One of the most difficult challenges is synthesis of high indium bearing ternary alloys (GaInN, AlInN). Both the primary strength and major weakness of this class of materials are best illustrated by the energy bandgap vs. lattice parameter diagrams shown in Figure 2.1. The GaInN alloy system offers a wide range of bandgaps, which is of great interest for MJ solar cell technology. This benefit is accompanied, however, by an enormous lattice parameter mismatch between its binary compound endpoints – *as the bandgap of GaInN decreases from 2.6 to 0.8 eV its lattice parameter increases by a whopping 8.3%!*
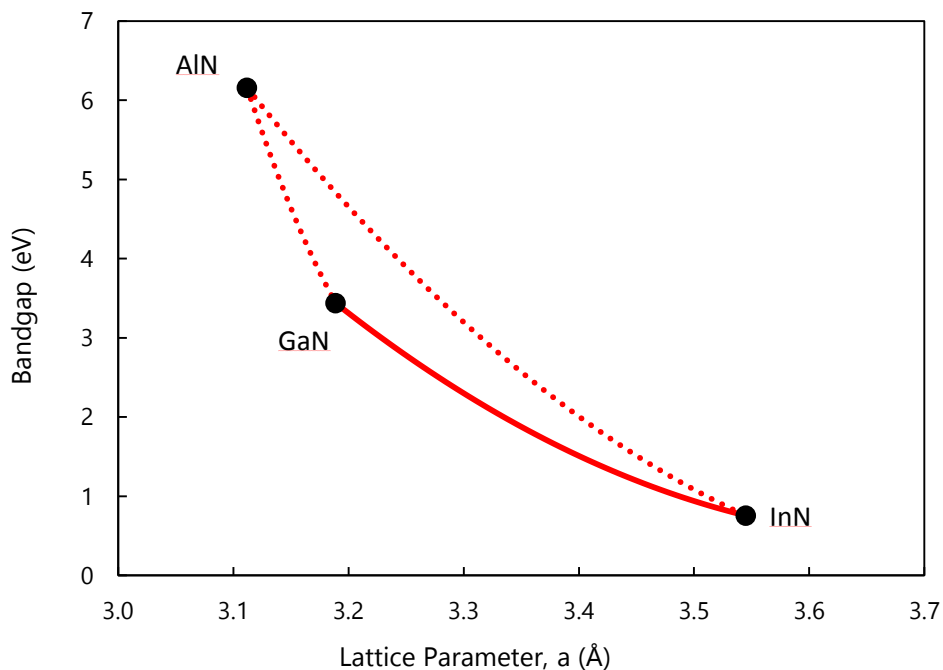
Figure 2.1. Lattice Parameter (*a* in the wurtzite crystal structure) vs Bandgap of GaInN, AlGaN, and AlInN ternary alloys.

This means that $Ga_{1-x}In_xN$ absorber layers must be kept extremely thin, and their indium content mole faction (x) must be kept low, to avoid stress relaxation via the formation of misfit and/or threading dislocations, which are known to severely limit minority carrier lifetimes [14-16]. For example, $Ga_{0.8}In_{0.2}N$ that is *pseudomorphic* with GaN (i.e. elastically distorted to match the in-plane lattice constant of GaN without dislocation formation) has a critical thickness of only 3.5 nm, as shown in Figure 2.2. Unfortunately, this same $Ga_{0.8}In_{0.2}N$ alloy has a (strain-free) bandgap of at least 2.6 eV; such an absorber layer would be expected to pass *without collection* 97% of the photon flux from the AM1.5G solar spectrum.
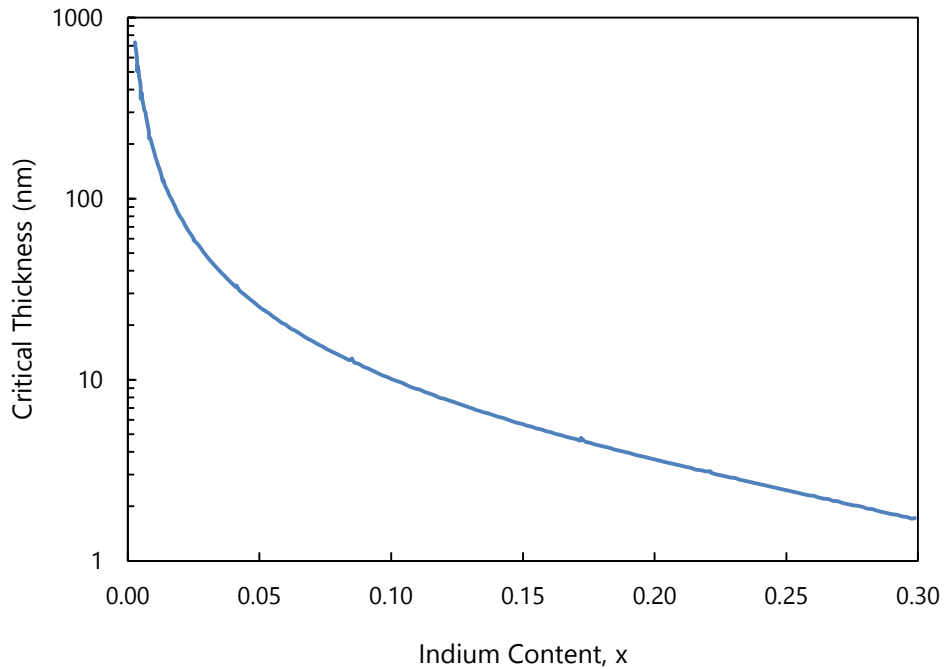
Figure 2.2. Calculated critical thickness values for $Ga_{1-x}In_xN$ films grown on top of bulk GaN as a function of indium composition [15]. Theoretical models predict that beyond the critical thickness, the material quality will degrade by means of dislocation formation.

Another major challenge for GaInN alloy system lies with the difficulty of making well-conducting p-type material, especially at high indium compositions. Even high p-type doping of GaN remains an issue today due to electronic compensation of Mg acceptors during growth

combined with an extremely large ionization energy (~200 meV), resulting in a maximum hole concentration of low 10^{18} cm^{-3} at room temperature [17-19]. This limited range of doping will impact MJ solar cell designs, which are electrically connected by n$^+$/p$^+$ tunneling diodes, lowering their overall efficiency due to additional loss. High indium content GaInN has also shown a tendency to be heavily n-type without purposeful introduction of donor species, likely caused by the presence of a native point defect with its energy level positioned very close to or in the conduction band depending on indium content [12, 20]. This defect level makes p-type doping of GaInN even more difficult, as the acceptor concentration will need to be higher to overcome the inherent n-type doping. Moreover, the difficulty of forming quality ohmic contacts to p-type GaInN has also been well documented [21-22], increasing the difficulty of fabricating high quality p-*i*-n or p-n GaInN solar cells.

In spite of these challenges, it may be possible to build high-performance MJ solar cells at low manufacturing cost using multi-crystalline (*mc*) or amorphous (*a*) GaInN materials. It has been theorized that *a*-GaInN possess a direct bandgap, without a mid-gap "defect" band, allowing for direct valence-band to conduction-band energy transitions [23-24]. Unfortunately, acceptor (p-type) doping of *mc*-GaInN or *a*-GaInN remains as a major technical roadblock – the research community has not yet even begun to explore this topic.

A novel approach to overcoming this challenge would be to construct GaInN Schottky barrier solar cells using only n-type material. This concept can be extended to MJ designs to increase efficiency by employing a single optically transparent electrode material with metallic-like electrical conductivity to interconnect junctions. The donor concentrations in the adjacent semiconductor layers determine whether this electrode behaves as an ohmic or Schottky contact.

In short, this design uses a *composite Schottky plus ohmic electrode* to electrically connect sub-cells thereby eliminating the need for n$^+$/p$^+$ tunnel junctions.

The equilibrium energy band diagram for this device structure, Figure 2.3, was generated using APSYS, a commercial software package from Crosslight Software, Inc. APSYS employs the finite element method to execute numerical analysis of semiconductor optoelectronic devices.
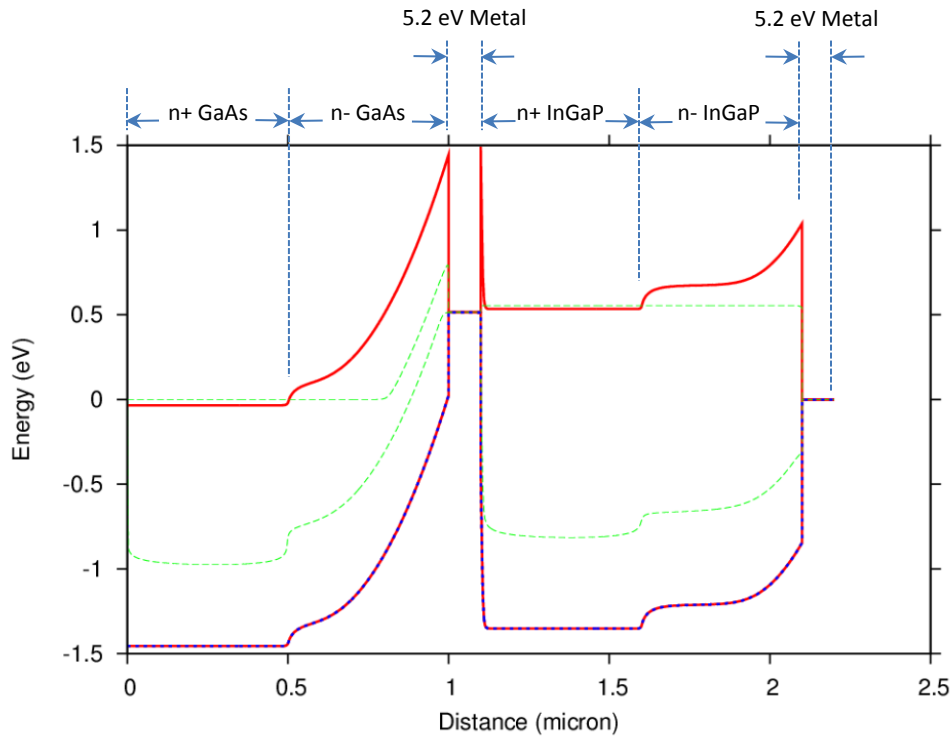
Figure 2.3. Equilibrium energy band diagram for a tandem GaInP-GaAs Schottky solar cell. The metal contact (5.2 eV metal at 1 μm from the bottom of the structure) serves as both an ohmic contact to the GaInP top-cell and a Schottky contact to the GaAs bottom-cell.

The combination of GaAs and Ga$_{0.49}$In$_{0.51}$P was employed as the narrow bandgap (1.43 eV) and wide bandgap (1.89 eV) semiconductors, respectively. This choice was made because numerical simulations do not converge when using APSYS material files for Ga$_{1-x}$In$_x$N alloys with similar bandgaps. The novel Schottky electrode is denoted as "5.2 eV metal" in this diagram. Note that

this material serves two different purposes: *Schottky contact* to GaInP top-cell (boundary condition at uppermost surface of structure on the right) and *Ohmic/Schottky interconnect* between GaInP top-cell and GaAs bottom-cell (at a distance of 1 μm above the bottom of the structure on the left).

The performance of this new style of tandem solar cell is reflected by the simulated J-V characteristics shown in Figure 2.4. At this juncture, no effort has been made to "current match" the top and bottom sub-cells; nevertheless *tandem* solar cell operation is evidenced by the addition of open-circuit voltages ($V_{OC} = 0.48$ V for bottom cell / $V_{OC} = 0.56$ V for top cell / $V_{OC} = 0.98$ V for tandem cell).
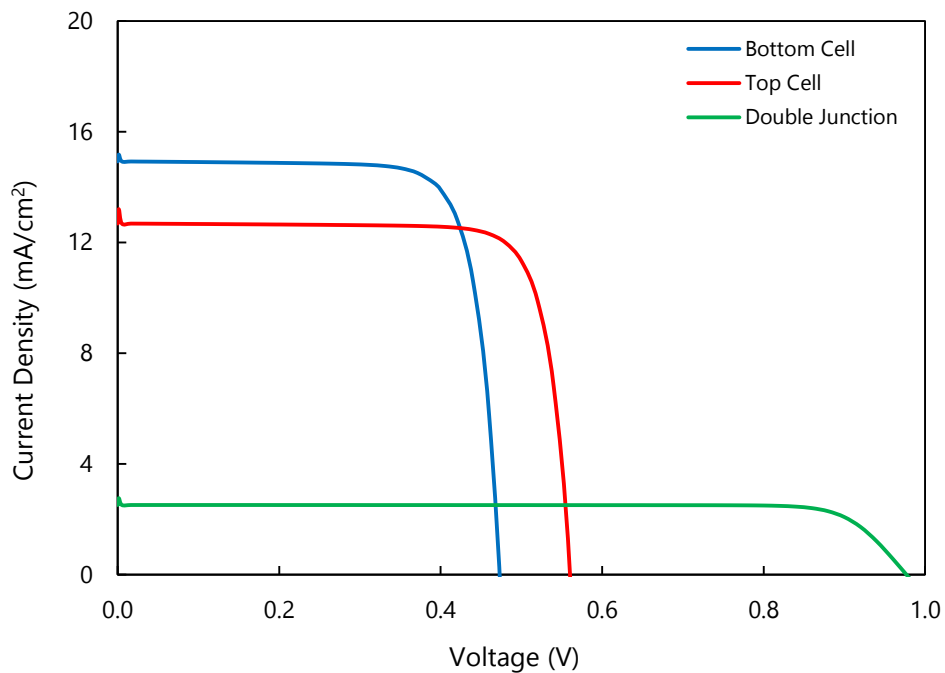
Figure 2.4. Simulated current density vs. voltage characteristics under AMG1.5 (1-Sun) illumination. Independent bottom cell (GaAs) operation is represented by the blue curve. Independent top cell (GaInP) operation is denoted by the red curve. Combined two-junction (tandem) solar cell performance is evidenced by the green curve.

Another important observation is that adopting *mc*-GaInN or *a*-GaInN materials would circumvent the need to satisfy conflicting requirements of lattice matching *plus* high indium content. Moreover, growth rates for *mc*-GaInN or *a*-GaInN will likely be higher than for *single-crystal* materials. These two attributes should give rise to lower manufacturing cost. The combination of novel MJ device architecture (higher conversion efficiency) with *mc*-GaInN or *a*-GaInN materials (low-cost synthesis) offers a pathway to a new Class 3 solar cell technology.

2.2 Research Objectives

Since the quality of contemporary *mc*-GaInN or *a*-GaInN materials are not yet suitable for solar cells, this work aims to demonstrate photovoltaic devices using single-crystal GaInN/GaN structures. A Schottky barrier device architecture will be employed that incorporates only n-type semiconductor materials in order to circumvent issues related to poor p-type doping of single-crystal GaInN (which are also likely to exist in the multi-crystalline and amorphous states [25-28]).

Using single-crystal GaInN material with a Schottky electrode, this thesis aims to:

> *Demonstrate the feasibility of multi-crystalline or amorphous GaInN solar cells through comparison of single-crystal GaInN/GaN Schottky barrier devices to conventional single-crystal GaInN/GaN p-i-n solar cells.*

The specific tasks which will be completed for this work are:

> *Develop and optimize fabrication techniques for GaInN/GaN Schottky barrier devices to demonstrate operational solar cells.*

> *Characterize electrical and optical parameters of Schottky electrode material, which are likely to impact solar cell performance metrics.*

Compare and contrast the performance of GaInN/GaN Schottky solar cells against theoretical expectations based on electrical and optical parameters of the Schottky electrodes.

3. TECHNICAL BACKGROUND

3.1 Principles of Solar Cell Operation

In its most basic form, a solar cell is a light absorbing medium that creates electron-hole pairs by absorbing photons with sufficient energy to excite such carriers. These carriers are then swept apart and moved to the electrical contacts to produce useable electrical power. A simple diode forms the basic structure for all semiconductor solar cells of which the most common form is a n^+-p diode. As indicated in Figure 3.1a, the n^+-p junction creates an electric field within the depletion region centered at the "metallurgical" doping interface. Photo-generated minority carriers (electrons in the p-type absorber layer) that diffuse to the edge of the depletion region are swept across to the opposite (n^+) side of the junction. These same electrons, which are majority carriers in the n^+ emitter, undergo dielectric relaxation to reach the metal anode where they are collected and contribute to actual generated power.
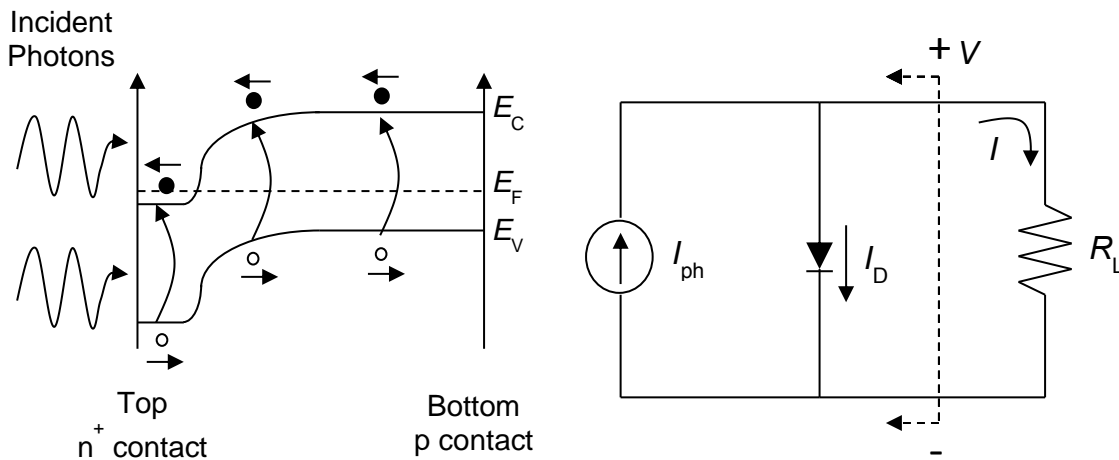
Figure 3.1. Left (a): Energy band diagram of an n^+-p diode. Right (b): Simple circuit model of a semiconductor solar cell.

A simple circuit model used to represent a solar cell is shown in Figure 3.1b, where a current source (I_{ph}) denoting the photo-generated carrier flux is in parallel with the opposing diode

current (I_D) and the difference between the two is the current (I) delivered to the load. Equation 3.1 relates all of these currents using the ideal diode equation where I_0 is the saturation current, n is the diode ideality factor, and kT/q represents the thermal voltage. Equation 3.2 gives I_0 in terms of basic material parameters, where the pre-factor C depends on doping concentration, carrier mobility, carrier lifetime, and more, q is the electron charge, and A is the area of the device.

$$I(V) = I_{ph} - I_D = I_{ph} - I_0 \left(e^{\frac{qV}{nkT}} - 1 \right) \qquad (3.1)$$

$$I_0 = C * q^2 A e^{\frac{-E_G}{kT}} \qquad (3.2)$$

An ideal current-voltage (I-V) characteristic of a solar cell is plotted in Figure 3.2a. Photo-generated current introduces a vertical shift in the I-V curve. Standard conventions place the power generating portion of the curve into the positive x and y axis of the Cartesian coordinate system so the I-V curve is flipped to represent generated power as shown in Figure 3.2b. The intersection of the y-axis and the curve yields the short circuit current, I_{SC}, and the intersection with the x-axis gives the open circuit voltage, V_{OC}. The value of I_{SC} represents the maximum possible current that the solar cell can deliver (which also happens to occur if the load were shorted). The value of V_{OC} represents the maximum voltage which can be developed across the solar cell under open circuit conditions (i.e., infinite load impedance).
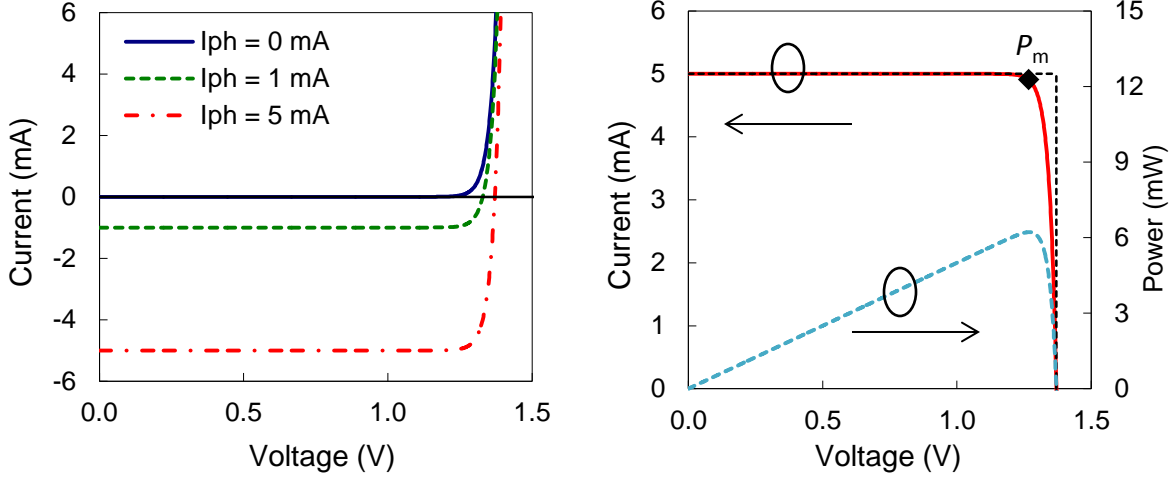
Figure 3.2. Left (a): Calculated I-V characteristics of a solar cell where I_{ph} is set to 0, 1, and 5 mA. Right (b): The same I-V curve (for I_{ph} = 5 mA) is re-plotted as a power-generating device in quadrant one of the Cartesian coordinate system, along with the corresponding power vs. voltage curve. The horizontal and vertical dashed lines represent V_{OC} and I_{SC} respectively and P_m indicates the maximum power point.

If $V = 0$ in Equation 3.1, then $I (V = 0)$ is defined as I_{SC} and $I_{SC} = I_{ph}$. This latter definition holds for all conditions since I_{ph} is treated as an ideal current source. If Equation 3.1 is set to zero, then $V (I = 0)$ is defined as V_{OC}. Now, solving Equation 3.1 for V_{OC} yields Equation 3.3, showing the clear dependence of V_{OC} on I_{SC} and I_0. Remember that I_0 is exponentially dependent on E_G and thus V_{OC} has a strong linear dependence on the bandgap of the solar cell material.

$$V_{OC} = \frac{nkT}{q} \ln \left(1 + \frac{I_{SC}}{I_0} \right) \tag{3.3}$$

The fill factor, FF, which is another key device parameter, is defined in Equation 3.4. It compares the product of the voltage (V_M) and current (I_M) at the maximum generated power against the product of the open circuit voltage and short circuit current. If there is a significant amount of series resistance or shunt resistance, the fill factor will decrease and the overall shape of the I-V curve will become less rectangular-like. It's important to note that the fill factor will

never be 100% due to the exponential nature of the diode I-V curve. Fill factors greater than 70% are considered to be very good in practice. The most important solar cell parameter is the power conversion efficiency, η, defined by Equation 3.5, which is the maximum electrical power delivered to the load divided by the input optical power.

$$FF = \frac{P_M}{V_{oc}I_{sc}} = \frac{V_M I_M}{V_{oc}I_{sc}} \tag{3.4}$$

$$\eta = \frac{P_{out}}{P_{in}} = FF \frac{V_{oc}I_{sc}}{P_{in}} \tag{3.5}$$

The generated photocurrent within any solar cell can be related to its spectral response, defined as the number of electron-hole pairs collected at the contacts per incident photon over a narrow linewidth range centered at the photon wavelength. The spectral response is thus, a function of the incident photon wavelength. Equation 3.6 summarizes this relationship in terms of the spectral distribution of incident light $F(\lambda)$, the spectral response of the solar cell, $SR(\lambda)$, and the total device area, A.

$$I_{ph} = qA \int_0^\infty F(\lambda)SR(\lambda)d\lambda \tag{3.6}$$

Common spectral distributions for solar illumination include Air Mass 1.5 (AM1.5) which corresponds to the solar spectrum reaching the Earth's surface throughout the United States and Air Mass 0 (AM0) which corresponds to the solar spectrum in space. As solar energy passes from space through the atmosphere, specific frequencies of light are absorbed resulting in the AM1.5 spectrum. Thus, AM1.5 contains roughly 30% less overall incident power compared to AM0. Additionally due to the different spectra, solar cells optimized for absorption of the AM1.5 spectrum are not necessarily optimized for AM0.

The spectral response of a solar cell can be represented as the product of two sub-components. The first contribution to $SR(\lambda)$ depends upon the absorption spectrum of the material and the total thickness of the absorbing medium. The second contribution to $SR(\lambda)$, known as the carrier collection efficiency (CCE), reflects the effectiveness of the device architecture at separating carriers and moving them to the contacts before they are lost via recombination.

3.2 Comparison of Device Architectures

3.2.1 Single-junction n-p diodes

Single-junction n^+-p diode solar cells typically employ a thin, heavily doped (n^+) layer, referred to as the "emitter", followed by a much thicker but lightly doped (p) "base" region as shown in Figure 3.3a. In such designs, the quasi-neutral region of the base is where most of the light absorption takes place. Low p-type doping helps to increase the minority carrier (electron) diffusion length within the material. Photo-generated electrons must reach the depletion region, before recombining with holes, where they are swept across the junction by the internal electric field. Similarly, photo-generated holes in emitter must reach the depletion region where they are also swept across the junction, eventually reaching the base electrical contact. Carrier collection efficiency can be enhanced by the addition of a back surface field layer below the p-type base (window layer above the n-type emitter) which prevents diffusion of photo-generated electrons (holes) in the wrong direction. To take full advantage of a thick quasi-neutral base region, the minority carrier lifetime (and corresponding diffusion length) must be as long as possible. Thus, this type of device architecture is used only when the semiconductor materials are of the highest quality (i.e., Si based solar cells or III-V devices made using lattice matched alloys).

17

3.2.2 Single-junction n-*i*-p diodes

If instead one is forced to work with lower quality materials having especially short carrier lifetimes ($\tau \leq 10^{-9}$ s) then alternative designs must be employed that rely almost exclusively on the internal electric field to separate and collect photo-generated electrons and holes. In other words, short lifetimes result in very short carrier diffusion lengths, making traditional n$^+$-p designs unsuitable. The modified device structure must contain a thick "intrinsic" region across which an electric field is established by embedding it between n-type and p-type layers (relatively thin but heavily doped), as illustrated in Figure 3.3b. In practice, the intrinsic or *i* region is actually lightly doped n-type (p-type) owing to the incorporation of residual donors (acceptors) during crystal growth. In the early days of semiconductor research such lightly doped layers were designated as ν (n-type) or π (p-type) to distinguish them from truly intrinsic material. It is now common, however, to refer to these device structures as n-*i*-p or p-*i*-n diodes.
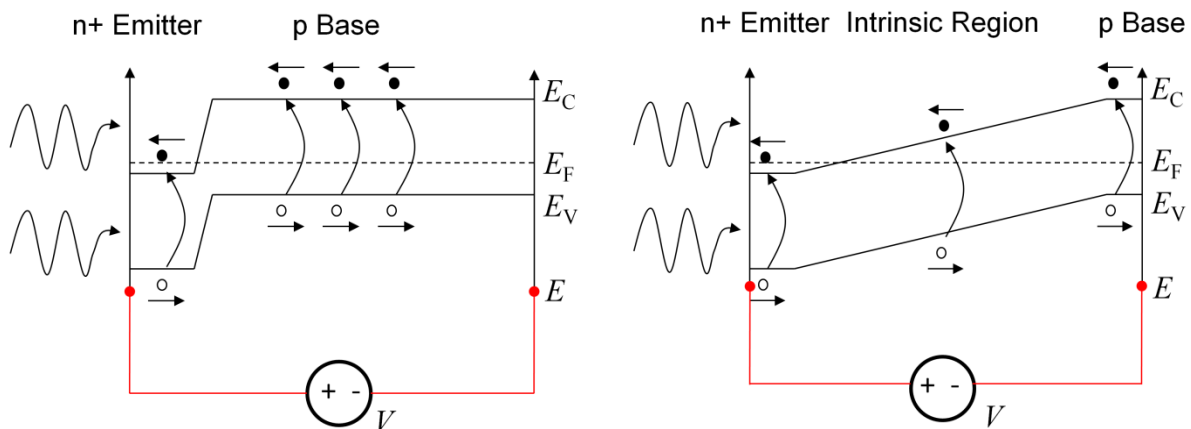
Figure 3.3. Left (a): Energy band diagram of an n$^+$-p solar cell. Right (b): Energy band diagram of an n$^+$-*i*-p solar cell. Most of the absorption for the n$^+$-p structure happens in the base region while absorption takes place in the intrinsic region for the n$^+$-*i*-p design.

There are two important considerations that must be balanced when optimizing the thickness and the background doping level of the *intrinsic* region.

1.) Sufficiently large thickness for complete absorption of photons.

2.) Strong enough electric field distributed across its thickness for effective carrier separation and collection.

This type of device architecture should be implemented when using lower quality semiconductor materials to reduce manufacturing costs: e.g., highly defective single-crystal layers (GaAs-on-Si) or polycrystalline (CIGS) or amorphous (*a*-Si) films.

3.2.3 Single-junction Schottky diodes

A Schottky barrier solar cell has advantages over the standard n$^+$-p or n-*i*-p designs. For example, the depletion region, and associated electric field, extends to the surface of the semiconductor, as shown in Figure 3.4. This removes the need for a window layer to prevent carrier flow in the wrong direction and also enhances collection of carriers generated by higher energy photons which are absorbed very close to the surface.
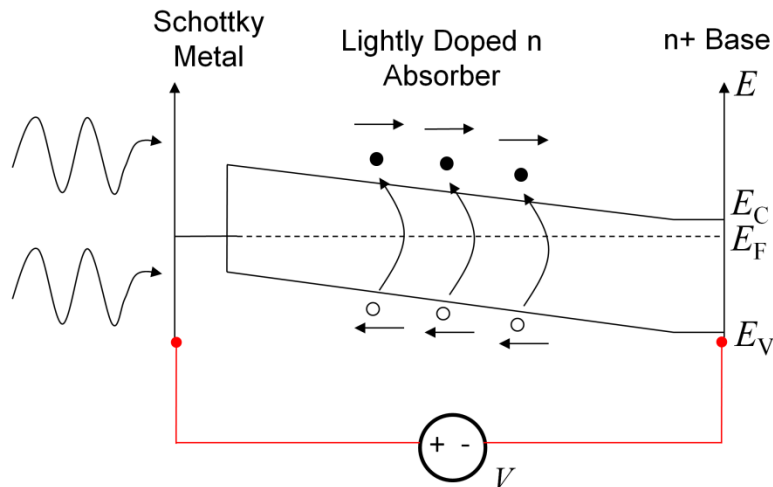
Figure 3.4. Energy band diagram of a Schottky diode solar cell with n-type semiconductor. Photo-generated holes are swept towards the top Schottky electrode while electrons flow to the bottom ohmic contact.

If one assumes thermionic emission as the sole current flow mechanism, then the I-V characteristic for a Schottky solar cell can be given by Equation 3.7, where I_{sat} is the saturation current, T is the temperature, q is the electron charge, k is Boltzmann's constant, and n is the diode ideality factor. Equation 3.8 gives I_{sat} in terms of basic material parameters, where R is the Richardson constant (assumed to be 24 A m^{-2} K^{-2} for GaN using an effective electron mass of 0.2 m_e), A is the area of the device, T is the temperature, q is the electron charge, k is Boltzmann's constant, and φ is the Schottky barrier height. Equation 3.9, which is derived from Equation 3.7, makes it evident that for Schottky solar cells, V_{OC} is dependent on the barrier height, as opposed to being dependent on E_G as in the case of n-p or n-i-p diodes. This change in dependence for V_{OC} can be viewed as a power conversion loss given that the Schottky barrier height is always less than the bandgap of the underlying semiconductor material.

$$I(V) = I_{ph} - I_D = I_{ph} - I_{sat}\left(e^{\frac{qV}{nkT}} - 1\right) \qquad (3.7)$$

$$I_{sat} = ART^2\left(e^{\frac{-q\varphi}{kT}}\right) \qquad (3.8)$$

$$V_{OC} = \frac{nkT}{q}\ln\left(1 + \frac{I_{SC}}{I_{sat}}\right) \qquad (3.9)$$

The second important loss to consider is the transparency of the Schottky contact. The Schottky electrode must cover the entire surface to form a uniform, one-dimensional electric field profile, resulting in absorption loss through this layer which cannot be avoided. This optical loss directly impacts the number of photons entering the absorption region causing a reduction in the photo-generated current. The impact of this loss can be quantified by modifying Equation 3.6 to produce Equation 3.10, where $T(\lambda)$ represents the transmission of light through the Schottky electrode material at a given wavelength.

$$I_{ph} = qA \int_0^{\infty} F(\lambda)T(\lambda)SR(\lambda)d\lambda \qquad\qquad (3.10)$$

3.3 Case for Multi-Junction Technology

In order for solar radiation to be absorbed by a semiconductor, some of the incident photons must have energies greater than its bandgap (the absorption coefficient rapidly drops off to zero at lower energies). This unique property has two important consequences:

1. Photons with energies significantly larger than E_G create electrons (holes) high up in the conduction (valence) band. These hot carriers rapidly "thermalize" down to energy states much closer to their respective band edges, giving up their extra energy as heat. Therefore, this excess photon energy ($E_{ph} - E_G$) does not contribute to the power generated by the solar cell.

2. Photons with energies smaller than E_G pass through the material without generating any photo-current.

Multi-junction solar cells help mitigate the impact of these two loss mechanisms on power conversion efficiency. For example, in a two-junction or *tandem* solar cell, the larger bandgap semiconductor is stacked closest to the light source and made thick enough to absorb all photons with energies above E_G (top cell), while passing lower energy photons to the underlying smaller bandgap material. This "filtering" approach reduces the energy loss that would otherwise happen in the bottom cell as hot carriers, generated by the absorption of photons with energies between E_G (top cell) and E_G (bottom cell), thermalize down to their respective band edges. The additional efficiency manifests itself only after satisfying the "current matching" condition. That is each individual sub-cell must generate the same amount of photo-current (because the current

21

flowing through the device must be constant everywhere within the structure). Otherwise, the short circuit current of a MJ solar cell would be limited by the lowest photo-current in any single sub-cell. The open circuit voltage of a MJ solar cell should equal the sum of the open circuit voltages of each individual sub-cell (minus some parasitic losses). In practice, a significant amount of effort is dedicated to identifying optimum bandgaps and thicknesses of absorber regions, matching these to a specific illumination spectrum for peak efficiency.

Multi-junction solar cells are grown in a continuous epitaxial stack and electrically connected using tunnel junctions. The two most common device architectures are shown in Figures 3.5a and 3.5b: upright cells where the substrate is included in the solar cell itself (typical of Ge based bottom junction designs) and inverted solar cells where the solar cell is grown in an inverted stack and the epitaxial film is then lifted off from the substrate (typical of growth on GaAs substrates). In both cases, some variance is allowed in the crystal lattice parameter to optimize bandgaps for each junction. However, these variations are generally no greater than 1% to limit the accumulated stress that accompanies in-plane lattice matching via elastic deformation. [29]. MJ devices incorporating sub-cells with lattice mismatch beyond 1% require the use of graded composition buffer layers which are usually of poor electrical quality [30].

n AlGaP (Window)	p InGaAs (Base)
n InGaP (Emitter)	n InGaAs (Emitter)
p InGaP (Base)	n^+/p^+ GaAs (TJ)
p AlInGaP (BSF)	p InGaP (BSF)
n^+/p^+ GaAs (TJ)	p GaAs (Base)
n InGaP (Window)	n GaAs (Emitter)
n Ga(In)As (Emitter)	n InGaP (Window)
p Ga(In)As (Base)	n^+/p^+ GaAs (TJ)
p InGaP (BSF)	p AlInGaP (BSF)
n^+/p^+ GaAs (TJ)	p InGaP (Base)
n Ge (Emitter)	n InGaP (Emitter)
p Ge (Base/Substrate)	n AlGaP (Window)
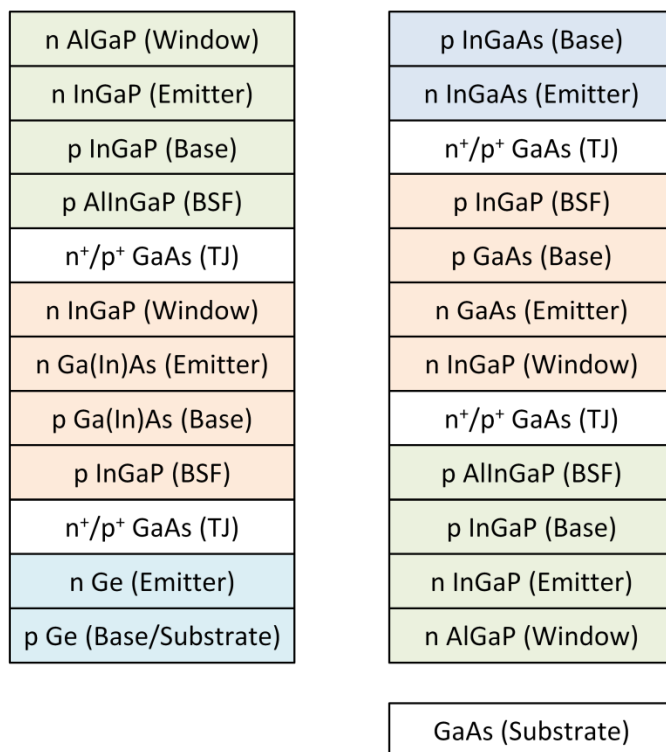
GaAs (Substrate)

Figure 3.5. Left (a): Upright MJ stack for a Ge bottom cell and substrate. Right (b): Inverted MJ stack grown on a GaAs substrate. In both cases, the top junction is highlighted in green, middle junction in orange, and bottom junction in blue.

Record efficiencies for triple-junction devices are now greater than 44% under *concentrated* AM1.5 solar illumination [5]; however, solar cells made using well developed materials are approaching their theoretical efficiency limits as predicted by detailed-balance calculations. In order to further increase solar cell efficiencies, new materials must be explored and integrated into advanced multi-junction designs. Table 3.1 outlines the ideal band gaps for solar cells to reach maximum efficiency for a given number of junctions [31]. In solar cells with four or more junctions, it is necessary to have *direct-gap* semiconductors with $E_G \geq 2.0$ eV to achieve maximum efficiency. $Ga_{1-x}In_xN$ alloys with $x \leq 0.4$ satisfy this requirement; however, they are a poor match to contemporary solar cell materials with regard to both crystal structure and lattice parameter. Therefore, adding GaInN junctions via direct epitaxial growth is probably not

23

feasible. Nevertheless, alternative integration paths could be pursued such as wafer bonding or mechanical stacking.

Number of Junctions	Values of Bandgaps (eV)	Max Theoretical η (%)
3	0.7, 1.37, 2	56
4	0.6, 1.11, 1.69, 2.48	62
5	0.53, 0.95, 1.4, 1.93, 2.68	65
6	0.47, 0.84, 1.24, 1.66, 2.18, 2.93	67.3
7	0.47, 0.82, 1.191, 1.56, 2, 2.5, 3.21	68.9
8	0.44, 0.78, 1.09, 1.4, 1.74, 2.14, 2.65, 3.35	70.2

Table 3.1. Optimal bandgap distribution and the maximum theoretical efficiency based on number of junctions under 1-Sun, AM1.5G illumination conditions [31]. In practice, the maximum achievable efficiency is only about 75-80% of the theoretical number.

3.4 Contemporary GaInN/GaN Solar Cells

3.4.1 GaInN/GaN p-*i*-n diodes

GaInN has both a high radiative recombination coefficient and low structural quality compared to other single-crystalline materials used for solar cells, resulting in a very short minority carrier lifetime, often on the order of 10^{-9} s or less. Additionally, due to the difficulty of growing high quality p-type material (in comparison to n-type), the thicker epitaxial layers in contact with the substrate are kept n-type to preserve material quality. Thus, p-*i*-n type designs are required to enhance carrier collection. Thankfully, balancing the total thickness of the absorbing region for a higher short circuit current while maintaining a sufficiently large electric field per unit length across the "intrinsic" region is facilitated by the very high absorption coefficient of GaInN ($> 10^5$ cm^{-1}). This large absorption coefficient enables $> 98\%$ absorption at a thickness of only 400 nm. In contrast, most other direct bandgap semiconductor materials such as GaAs have absorption

coefficients in the range of 10^4 cm^{-1}, requiring thicknesses around 3 μm for similar > 98% absorption! With such a large absorption coefficient, the total thickness of the absorbing region can be kept small; thereby increasing the electric field strength for a given acceptor (donor) concentration in the adjacent p-type (n-type) layer.

Most of the early work on GaInN solar cells employed "bulk" (or non-quantum confined) absorbers in the form of p-*i*-n homojunction or heterojunction designs. However, the material quality is generally poor in these cases owing to the lattice parameter mismatch problem identified earlier. More recent work has focused on the use of multi-quantum well (MQW) designs to improve material quality, or even superlattice (SL) structures to further enhance carrier collection. Figure 3.6 illustrates these structures with common thicknesses found in the literature.

Table 3.2 summaries the best published GaInN photovoltaic device results under solar illumination, grouped by general structure. It is clear that the homojunction and heterojunction designs are inferior to MQW and SL structures. Theory predicts a maximum film thickness of about 10 nm (1.7 nm) for $Ga_{0.9}In_{0.1}N$ ($Ga_{0.7}In_{0.3}N$) coherently strained to match the lattice parameter of GaN. These indium compositions bracket most values found in the literature, and yet the corresponding GaInN absorber regions are much thicker (see Figure 3.6). The insertion of barrier layers into MQW or SL designs that divide up the GaInN absorber material into numerous ultra-thin layers appears to improve material quality, as evidenced by significantly higher sort-circuit current densities. It's important to note however that all of these designs have indium compositions of less than 35% and most are below 20%! Future iterations must push for much higher indium content for better matching with the solar spectrum (1.0-1.5 eV).

(a)

(b)

(c)

(d)

Figure 3.6. Schematic layer structure for contemporary GaInN/GaN solar cells. Upper Left (a): GaInN homojunction. Upper Right (b): GaInN/GaN double heterojunction. Lower Left (c): GaInN/GaN MQW structure. Lower Right (d): GaInN/GaInN superlattice structure.

	$Ga_{1-x}In_xN$ & Illumination	V_{OC} (V)	J_{SC} (mA/cm²)	η	Reference
Homojunction	$x = 0.15$ 1 Sun, AM1.5	1.5	1.25	1.05%	[32]
	$x = 0.17$ 1 Sun, AM1.5	2.08	0.74	1.09%	[33]
Heterojunction	$x = 0.12$ 1 Sun, AM1.5	1.89	1.06	1.57%	[34]
	$x = 0.11$ 1 Sun, AM0	1.75	1.11	1.0%	[35]
Multi-Quantum Well	$x = 0.35$ 1 Sun, AM1.5	1.8	2.56	2.95%	[36]
	$x = 0.28$ 1.2 Suns, AM1.5	1.93	2.53	2.29%	[37]
Super-Lattice	$x = 0.07/0.17$ 1 Sun, AM1.5	1.77	3.08	2.46%	[38]

Table 3.2. Summary of best GaInN/GaN solar cells reported in literature (organized by material structure).

3.4.2 GaInN/GaN Schottky diodes

As of the writing of this dissertation, only one published article was found regarding a Schottky barrier based GaInN/GaN solar cell [39]. The work demonstrates a photo-response under UV lamp and UV laser excitation, but the I-V curves are not well behaved. In addition, the authors did not show actual solar cell performance under AM0 or AM1.5 illumination.

4. EXPERIMENTAL PROCEDURES AND RESULTS

4.1 Schottky Electrodes

One goal of this work is to make connections between select physical properties of the chosen Schottky electrode materials and the performance of GaInN/GaN solar cells made therefrom. Given the operating principles of Schottky solar cells, it would be desirable for a Schottky electrode to exhibit the following properties;

1. Large Schottky barrier to n-type GaN; the open circuit voltage of a Schottky solar cell depends strongly on the barrier height, as it is this quantity that has the largest impact on dark current.

2. High optical transparency for photon energies larger than E_G of the semiconductor absorber; if the Schottky electrode behaves as an ideal metal then solar radiation absorbed therein does not contribute to photo-generated current delivered to the load.

3. Low electrical resistivity at the requisite film thickness; if the Schottky electrode can be modeled as a "lumped circuit element" then a large effective resistance would distort the I-V characteristic and thereby reduce power conversion efficiency.

A high work function metal is required to form a good Schottky contact to n-type GaN. Platinum has a particularly large work function at 5.64 eV [40], and there is a wealth of published literature on Schottky diodes made from n-type GaN with Pt as the rectifying contact. Given that Pt is a simple metal (with no gap in its electronic band structure), an ideal Pt/n-type GaN interface should not present an impediment to the collection of photo-generated holes. Moreover, as a single metal layer with no requirement for post-deposition annealing, it is reasonable to assume that the Pt films employed herein are homogenous throughout their thickness and that

28

they do not contain other material phases. For all of these reasons, platinum should be a good baseline Schottky electrode.

The first "transparent" Schottky electrode of interest is an *oxidized* Ni/Au bilayer for which there is already a good amount of published literature [41-44]. This electrode material is most commonly used to make ohmic contacts to p-type GaN [44]; nevertheless, a few groups have also observed Schottky behavior on n-type GaN [45-47]. Another "transparent" material with good electrical conductivity is a thin *oxidized* layer of ruthenium and nickel. This electrode material has also been used for making ohmic contacts to p-type GaN [48-49]. Published results indicate that an oxidized 5 nm Ru / 5 nm Ni layer is even more transparent than its 5 nm Ni / 5 nm Au counterpart. There has not been any mention yet in the literature of oxidized Ru/Ni serving as a Schottky electrode on n-type GaN.

4.1.1 Evaluation of Schottky Barriers

Schottky diode test structures were made using n-type GaN material grown in Dr. Lou Guido's MOCVD reactor at Virginia Tech. First, a thin undoped GaN nucleation layer was deposited at low temperature on a 2 inch diameter c-plane sapphire wafer, followed by a 1 μm thick undoped GaN buffer layer grown at high temperature to achieve good structural quality. Next, a silicon-doped GaN test layer (1 μm thick) was grown at high temperature with $(N_D - N_A) = 9.2$ x 10^{16} cm^{-3} as established by capacitance-voltage measurements at room temperature. The uppermost GaN test layer serves as the device platform in contact with both the Schottky and ohmic electrodes.

Samples were cleaned using an agitated ultrasonic soak in acetone and isopropyl alcohol, followed by etching in aqua regia (3 HCl: 1 HNO$_3$), and then concentrated HF acid (all three

steps were 5 minutes in duration). Next, a thick 30 nm Ti / 400 nm Al metallic bilayer was deposited by electron-beam evaporation and annealed at 600 ºC in a hydrogen (5%) / argon (95%) gas mixture to form ohmic contacts. Then, the Schottky electrode material was deposited by electron-beam evaporation; 10 nm of Pt *or* 5 nm of Ni followed by 5 nm of Au *or* 5 nm of Ru followed by 5 nm of Ni. The Schottky electrode films were patterned using a standard photoresist lift-off process. Test diodes with Ni/Au *or* Ru/Ni bilayers were annealed at 500 ºC (10 minutes) or 600 ºC (3 minutes) respectively in normal laboratory air to "oxidize" the Schottky electrodes. Test diodes with Pt electrodes did not undergo thermal annealing. Finally, thick 50 nm Ni / 400 nm Ag pads were deposited on the Schottky electrodes for probe testing. A schematic side-view of the fully processed device is shown in Figure 4.1a, along with a plan-view optical image of its metallized surface in Figure 4.1b. Circular *planar-style* diode structures were fabricated with (inner) Schottky electrodes ranging from 250 to 500 μm in diameter and (outer) ohmic contacts of much larger area.
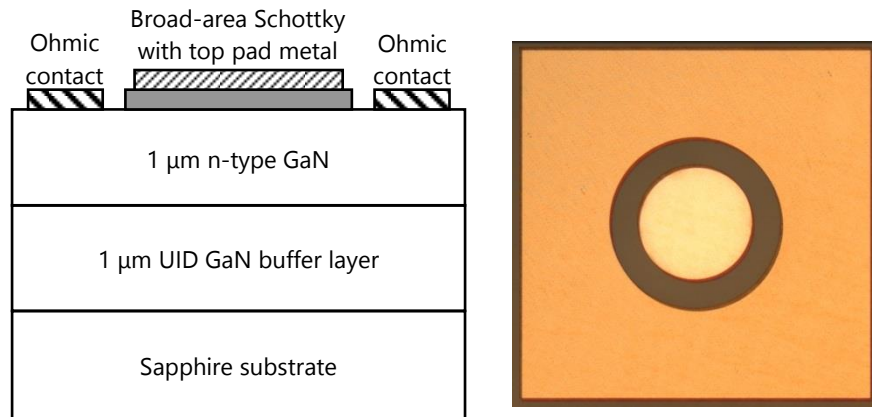
Figure 4.1. Fully processed GaN Schottky diode test structure. Left (a): Schematic cross-section of the *planar* device architecture. Right (b): Nomarski phase contrast image of the metallized surface with circular Schottky electrode.

Current vs. Voltage (I-V) measurement sweeps were performed at room temperature in the dark using a Keithley 2400 source meter unit (SMU). Raw current values were converted to current density by dividing out the area of the Schottky electrode. Direct fitting of Equation 4.1 to the resulting current density vs. voltage (J-V) curves was used to extract Schottky barrier heights and ideality factors (all symbols have been defined previously).

$$I(V) = ART^2 e^{\frac{-q\varphi}{kT}} \left(e^{\frac{qV}{nkT}} - 1 \right) \tag{4.1}$$

A representative set of J-V characteristics is shown in Figure 4.2 for the Pt Schottky electrode case. Each curve represents one distinct device under test, so the tight grouping indicates good sample uniformity.
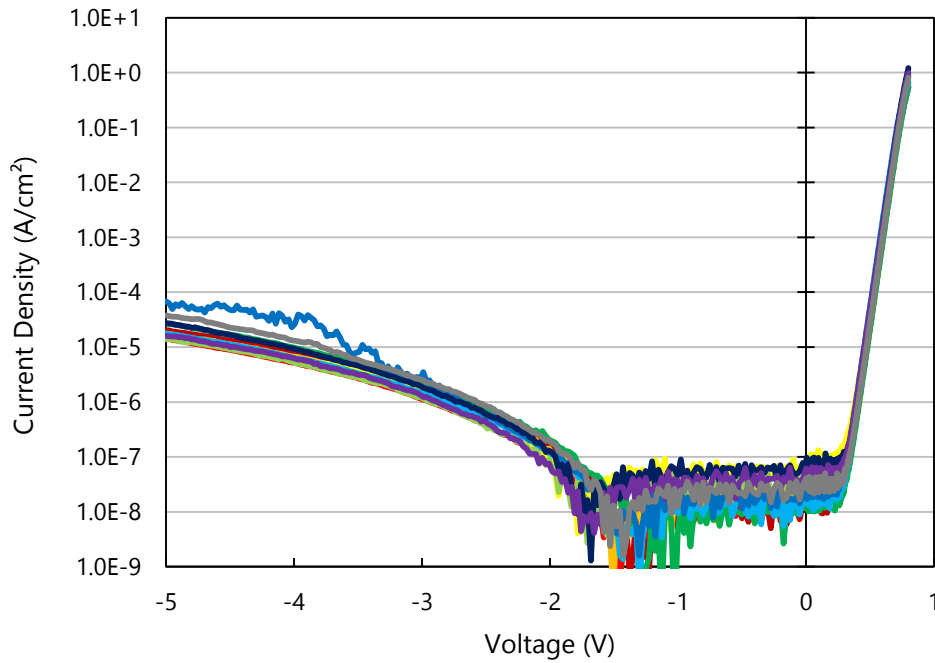
Figure 4.2. J-V characteristics for 10 nm Pt Schottky diodes on n-type GaN tested under reverse and forward bias with no illumination.

These Schottky diodes exhibit good rectifying behavior with reverse current density (J_R) around 3×10^{-5} A/cm^2 at -5 V and forward current density (J_F) greater than 1 A/cm^2 at +1 V. The curve fitting procedure yields a Schottky barrier height of 1.12 ± 0.02 eV with an ideality factor of 1.06 $\pm$ 0.02 (both φ and n values are comparable to published results [50-51]).

A representative set of J-V characteristics is shown in Figure 4.3 for the oxidized Ni/Au Schottky electrode case. These Schottky diodes exhibit more variation than in the Pt case, especially in the reverse bias direction. Overall the oxidized Ni/Au Schottky diodes show good rectifying behavior with J_R less than 1×10^{-6} A/cm^2 at -5 V (30x lower than in the Pt case) compared to J_F greater than 0.5 A/cm^2 at +1 V. Data analysis yields $\varphi = 1.12 \pm 0.04$ eV which is similar to the Pt case; however, the curve-fitted ideality factor is considerably larger ($n = 1.29 \pm 0.07$).
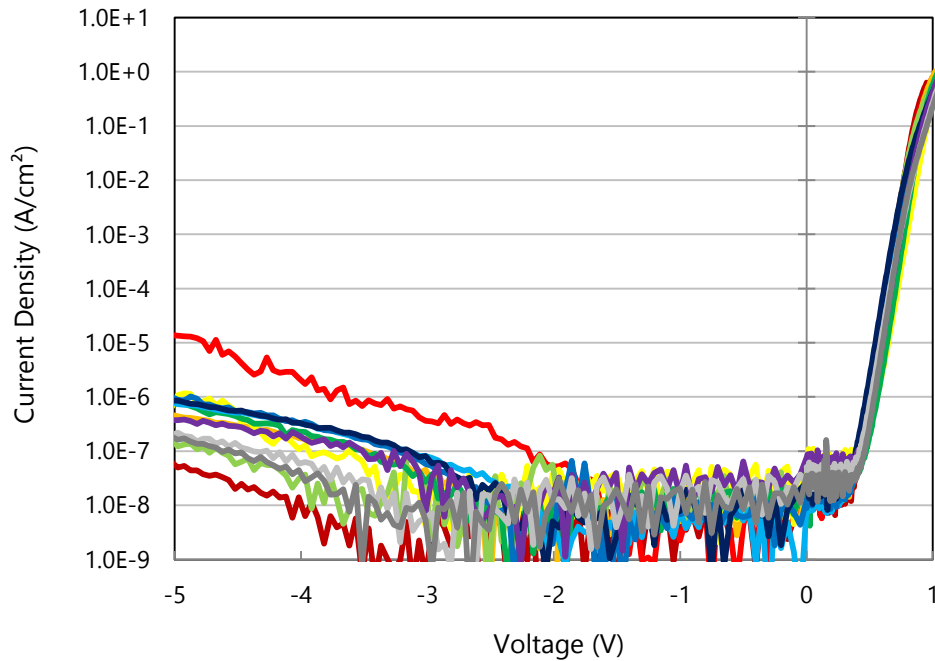
Figure 4.3. J-V characteristics for oxidized 5 nm Ni /5 nm Au Schottky diodes on n-type GaN tested under reverse and forward bias with no illumination.

A representative set of J-V characteristics is shown in Figure 4.4 for the oxidized Ru/Ni Schottky electrode case. These devices exhibit the worst uniformity of all three cases, even showing substantial variation under forward bias operation. The reverse blocking characteristics are slightly worse than the oxidized Ni/Au Schottky diodes but better than the Pt case, conducting 2.0×10^{-6} A/cm^2 at -5 V. It is also interesting that J_F is 1000x smaller at the same bias voltage (10^{-3} A/cm^2 at +1 V) compared to both the oxidized Ni/Au and Pt Schottky diodes. Curve fitting reveals that oxidized Ru/Ni Schottky diodes have the lowest barrier height (1.06 ± 0.04 eV) and highest ideality factor (1.78 ± 0.09) of the three cases under consideration.
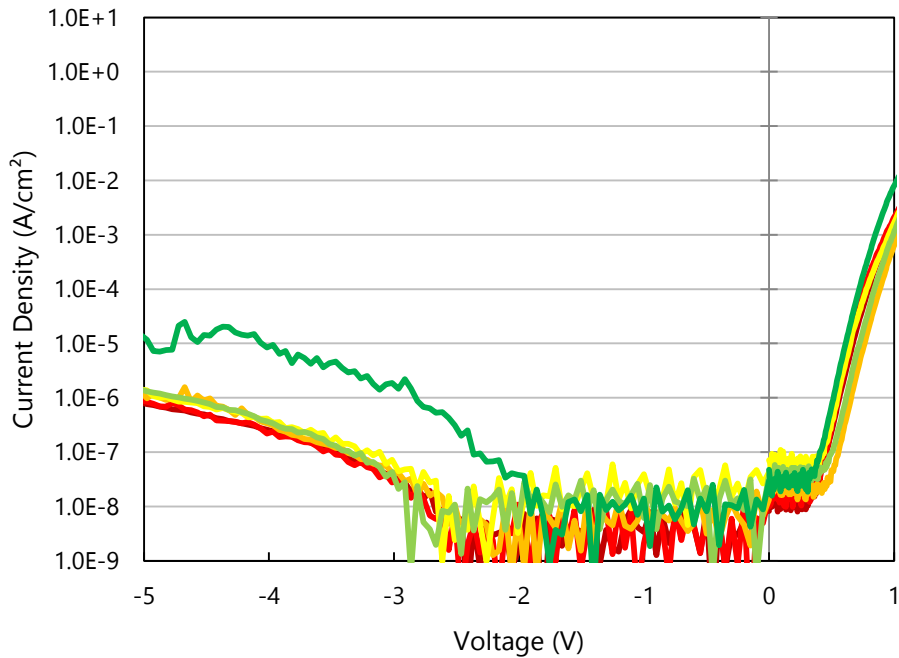
Figure 4.4. J-V characteristics for oxidized 5 nm Ru /5 nm Ni Schottky diodes on n-type GaN tested under reverse and forward bias with no illumination.

4.1.2 Evaluation of Optical Transparency

Test samples for evaluating the optical transparency of Schottky electrodes were prepared on one-quarter sections taken from 2 inch diameter double-side polished (DSP) sapphire wafers.

33

Prior to thin-film deposition, the substrates were thoroughly cleaned with acetone, isopropyl alcohol, de-ionized water, aqua regia, and concentrated HF acid. The Schottky electrode material was deposited by electron-beam evaporation; 10 nm of Pt *or* 5 nm of Ni followed by 5 nm of Au *or* 5 nm of Ru followed by 5 nm of Ni. The Pt films were measured in their as-deposited state. The Ni/Au and Ru/Ni bi-layers were oxidized at 500 ºC (10 minutes) and 500 ºC (5 minutes) respectively as described previously. In all three cases, the optical samples appeared uniform to the naked eye with no evidence of large-area defects.

Optical transmission spectra were recorded using a Filmetrics F20-UVX instrument at two locations (center and edge) on each sample. The raw data reflects the optical response of the film/substrate composite, so measurements were also taken on bare sapphire wafers for reference purposes. Photons with $\lambda < 430$ nm will be absorbed by the GaInN/GaN structures; hence, this wavelength range is of most interest when evaluating Schottky electrode materials. Transmission spectra for the Pt test sample are shown in Figure 4.5. After normalizing out the contribution from the sapphire, this Schottky electrode material has an optical transparency of 33% at 410 nm and it increases slightly to 36% at 340 nm.

Transmission spectra for the oxidized Ni/Au test sample are shown in Figure 4.6. The overall response is quite different from the Pt case; the *normalized* transparency is higher at longer wavelengths (73% at 410 nm), but it *decreases* steadily with wavelength (down to 63% at 340 nm). The data shown here are similar to those for oxidized Ni/Au films prepared by others on GaN (instead of sapphire) using the same deposition method and similar annealing conditions [44].
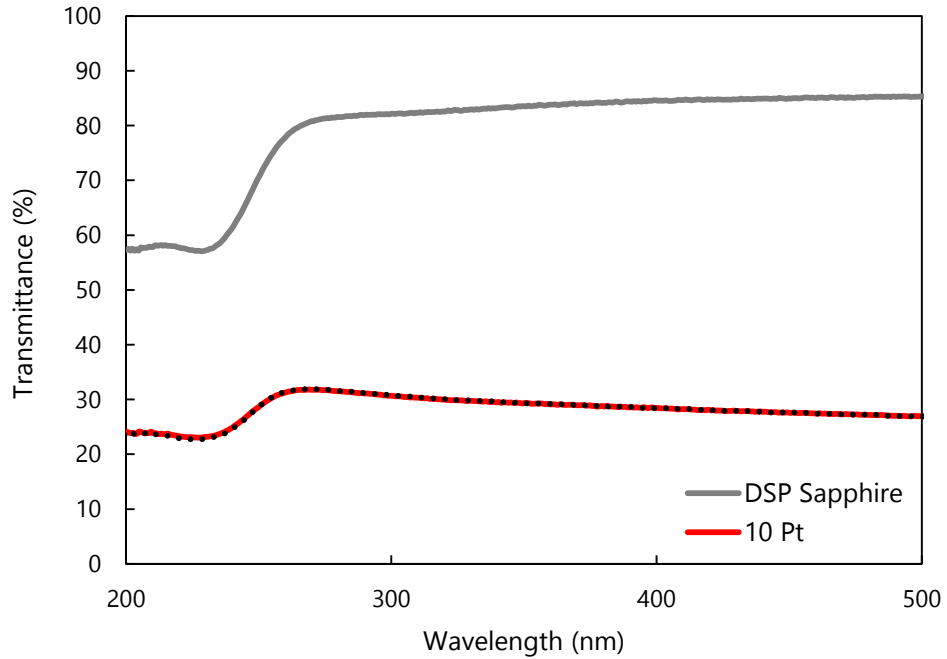
Figure 4.5. Raw transmission spectra of a 10 nm thick layer of Pt at the center (solid red line) and edge (dotted black line) of the sample. Data from a bare double-side polished sapphire substrate is also given for reference (gray line).
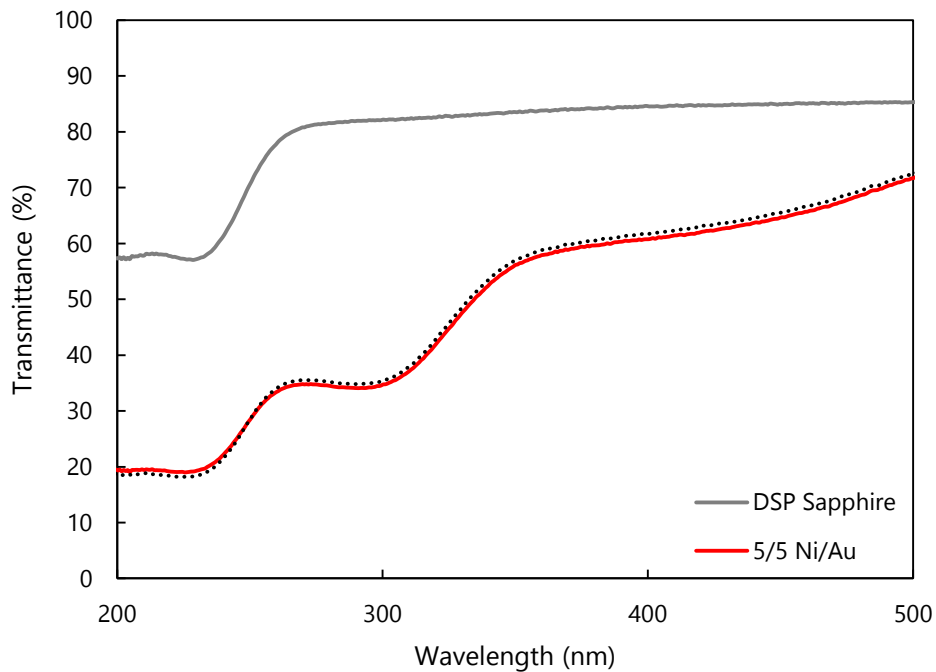
Figure 4.6. Raw transmission spectra of an oxidized 5 nm Ni / 5 nm Au film at the center (solid red line) and edge (dotted black line) of the sample. For reference, the transmission spectrum of a bare double-side polished sapphire substrate is also given (gray).

Transmission spectra for the oxidized Ru/Ni test sample are shown in Figure 4.7. The optical response is similar to the oxidized Ni/Au case; however, the *normalized* transparency is lower over the entire wavelength range (63% at 410 nm decreasing to 55% at 340 nm). An attempt was made to improve the situation by re-annealing the test sample at 600 °C for 3 minutes. Interestingly enough, the spectral response does not change much. The transparency of the oxidized Ru/Ni test samples described herein is somewhat lower than values reported by others [48-49] for films deposited on GaN but annealed under similar conditions.
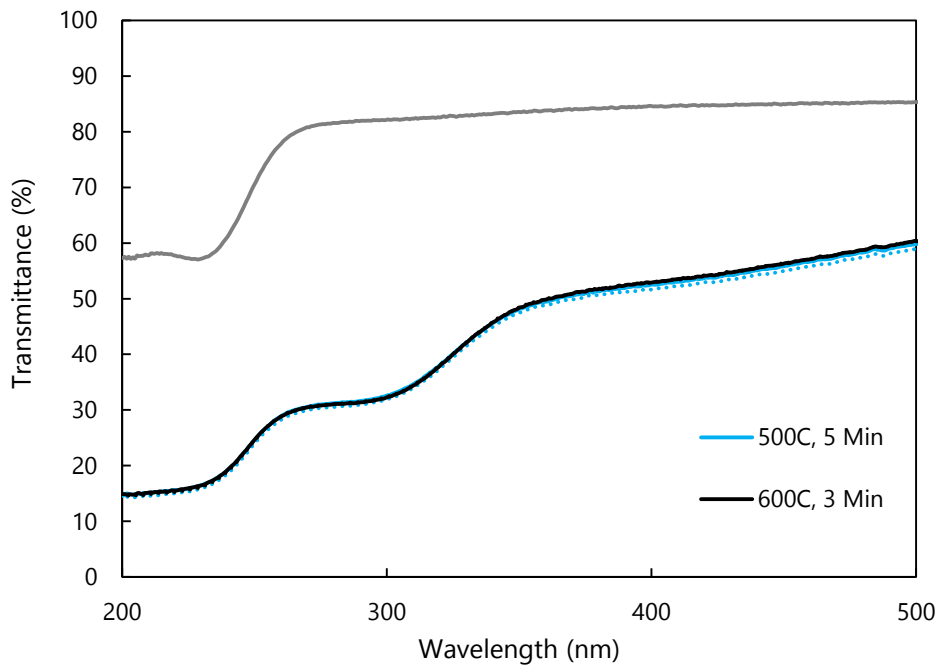
Figure 4.7. Raw transmission spectra of an oxidized 5 nm Ru / 5 nm Ni film after a 500 ºC, 5 min anneal (blue line), followed by an additional 600 ºC, 3 min anneal (black line). Both annealing steps were performed under normal laboratory air. Measurements were taken at the center (solid lines) and edge (dotted lines) of the sample. For reference, the transmittance of the double-side polished sapphire is also included (gray line).

4.1.3 Evaluation of Sheet Resistance

Test samples for evaluating the sheet resistance of Schottky electrodes were prepared on one-quarter sections from 2 inch diameter sapphire wafers, after cleaning them using ultrasonic agitation with acetone and isopropyl alcohol followed by a dip in aqua regia and then HF acid. First, a 200 nm thick nickel film was deposited (and pattered as described previously) to serve as an etch mask. The sapphire wafer was then etched to a depth of 0.25 μm using an inductively-coupled plasma (ICP) process with BCl_3/Cl_2 chemistry to form mesas which serve as alignment marks for subsequent fabrication steps. The nickel mask layer was stripped off using aqua regia and the sample was thoroughly cleaned again in acetone, isopropyl alcohol, aqua regia, and HF acid. Next, the Schottky electrode material was deposited (patterned) by electron-beam evaporation (photoresist lift-off); 10 nm of Pt *or* 5 nm of Ni followed by 5 nm of Au *or* 5 nm of Ru followed by 5 nm of Ni. The Pt films were left in their as-deposited state. The Ni/Au bilayers were oxidized at 500 ºC (10 minutes) and the Ru/Ni bilayers were oxidized at either 500 ºC (for 5 minutes) or 600 ºC (for 3 minutes). Finally, a 50 nm Ni / 400 nm Ag metal bilayer was deposited (patterned) by electron-beam evaporation (photoresist lift-off) on top of the Schottky electrode material to form probe contact pads. A finished transmission line measurement (TLM) structure is shown in Figure 4.8.
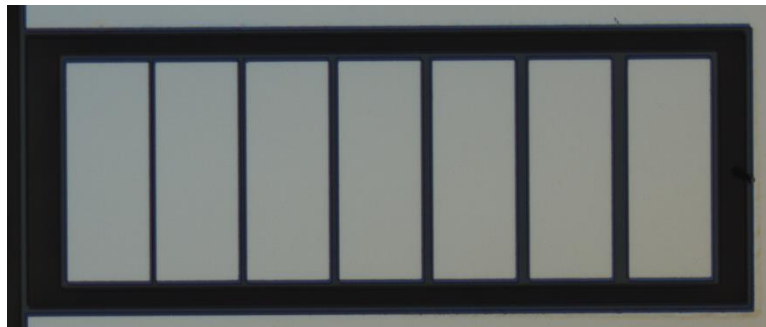
Figure 4.8. Nomarski phase contrast optical image of a TLM ladder structure with incremental spacing between contacts of 7, 10, 13, 16, 20, and 25 μm. A mesa has been etched around the ladder to prevent undesired fringe current flow.

Current vs. voltage sweeps were performed on these TLM "ladder" structures at room temperature using a Keithley 2400 SMU. A set of measured I-V curves from one ladder is shown in Figure 4.9. All of the curves are linear, as should be the case, and the inverse of the slope for a particular curve is proportional to the resistance across the corresponding ladder spacing. The entire set of curves represents all of the measured I-V curves for a single ladder structure.
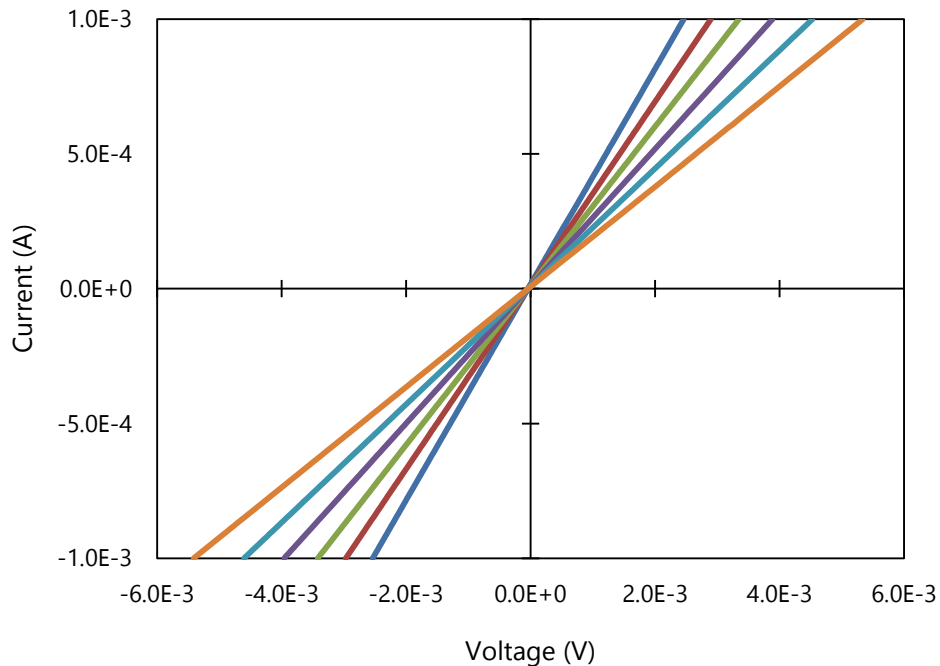
Figure 4.9. Family of measured I-V curves from one TLM structure, showing the increasing resistance as the ladder spacing increases.

The electrical resistance data in Figure 4.10 were obtained from measurements performed on the Pt test sample. Each symbol type (e.g. blue diamonds) represents data collected from one particular TLM ladder, with measurements taken from eight ladders in total to examine uniformity across the sample. The data is well behaved with a clear linear dependence exhibited between measured resistance and ladder spacing. A sheet resistance of $R_{SH} = 56.0 \pm 3.7$ Ω/sq was

obtained by fitting Equation 4.2 to the data plotted in Figure 4.10, where R_T is the total resistance from measurements, R_C is the contact resistance, L is the separation between two contacts on the ladder, and W is the width of each contact. Overall, the sheet resistance showed about 7% variation across the sample.

$$R_T = 2R_C + R_{SH}\frac{L}{W} \qquad (4.2)$$

Multiplying R_{SH} by the film thickness provides an *effective bulk resistivity* of 5.6 x 10^{-5} Ω-cm. For reference purposes, an electrical resistivity of 1.07 x 10^{-5} Ω-cm has been reported for "bulk" polycrystalline platinum [52].
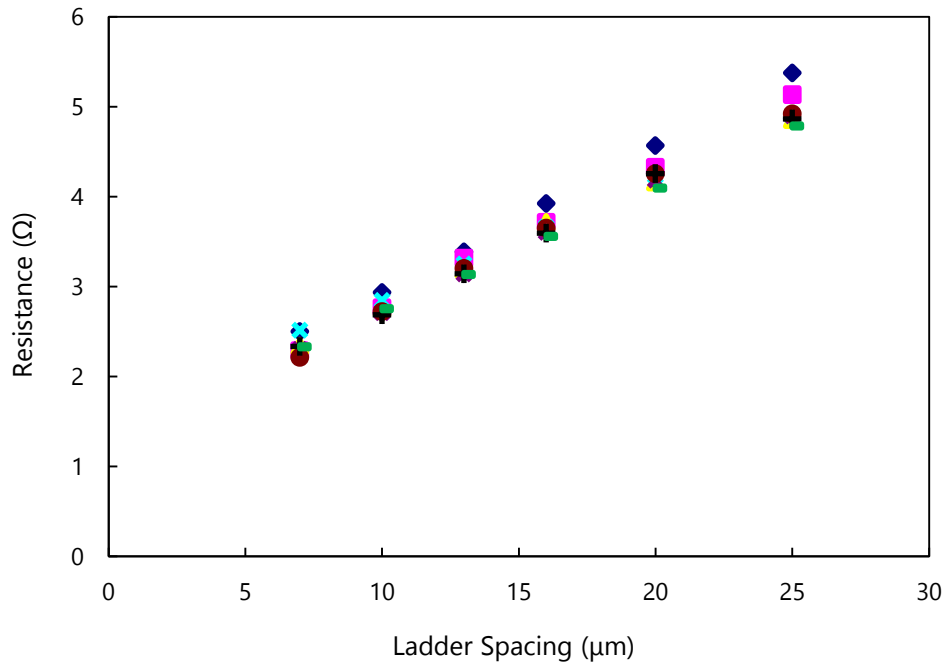
Figure 4.10. Resistance vs. ladder spacing for a 10 nm Pt film. Each set of data points of the same shape and color represents one entire ladder.

The electrical resistance data in Figure 4.11 were obtained from I-V curves recorded on the oxidized Ni/Au test sample. All of the TLM data sets exhibit a linear relationship between

resistance and ladder spacing. Application of the curve-fitting procedure yields $R_{SH} = 28.0 \pm 3.9$ Ω/sq, which is similar to a published result of 32.1 Ω/sq [44]. However, there is considerably more variation across the sample in comparison to the 10 nm Pt film. This is not surprising as TEM analysis and images reported by others [43] reveal a complex non-homogenous microstructure in Ni/Au films (annealed under almost identical conditions) on GaN epitaxial layers.
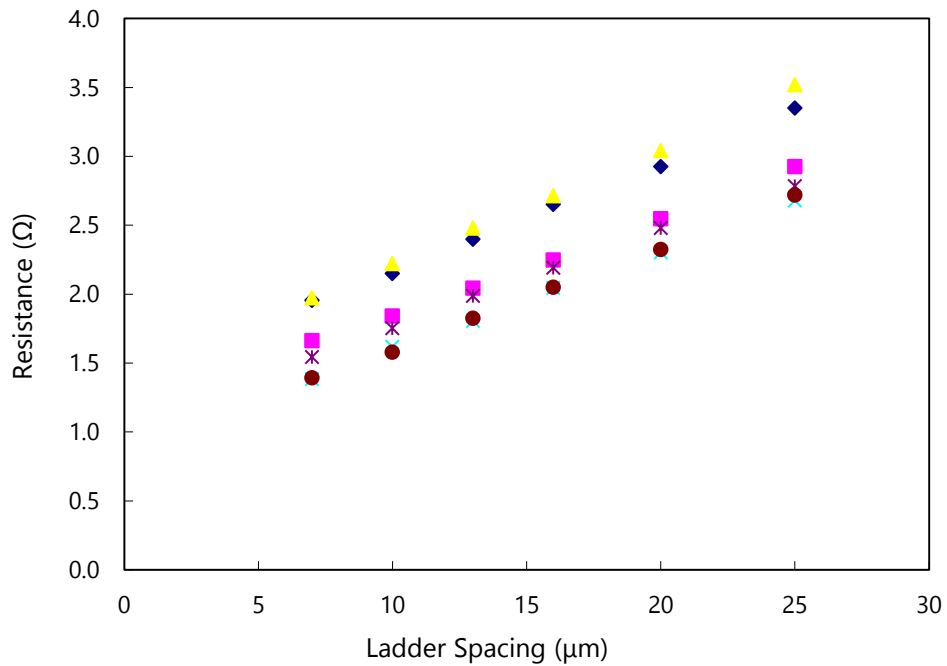
Figure 4.11. Resistance vs. ladder spacing for an oxidized 5 nm Ni / 5 nm Au film. Each set of data points of the same shape and color represents one entire ladder.

The electrical resistance data in Figure 4.12 were obtained from I-V measurements taken on the oxidized Ru/Ni test sample (after the 600 ℃, 3 minutes anneal). TLM data sets are once again linear in nature. Curve fitting to data taken after a 500 ℃, 5 minute anneal (data not shown) gives a sheet resistance of 370 $\pm$ 30 Ω/sq which is almost 10x larger than for the oxidized Ni/Au case. As shown in Figure 4.12, however, annealing at 600 ℃ for 3 minutes reduces R_{SH} by more

than 2x down to 171 ± 0.9 Ω/sq. It is also interesting that the ladder-to-ladder variation becomes *really small* after the second annealing step, indicating excellent uniformity across the sample. Comparisons to other work are not possible, because values of R_{SH} for oxidized Ru/Ni films have not been reported in the literature.
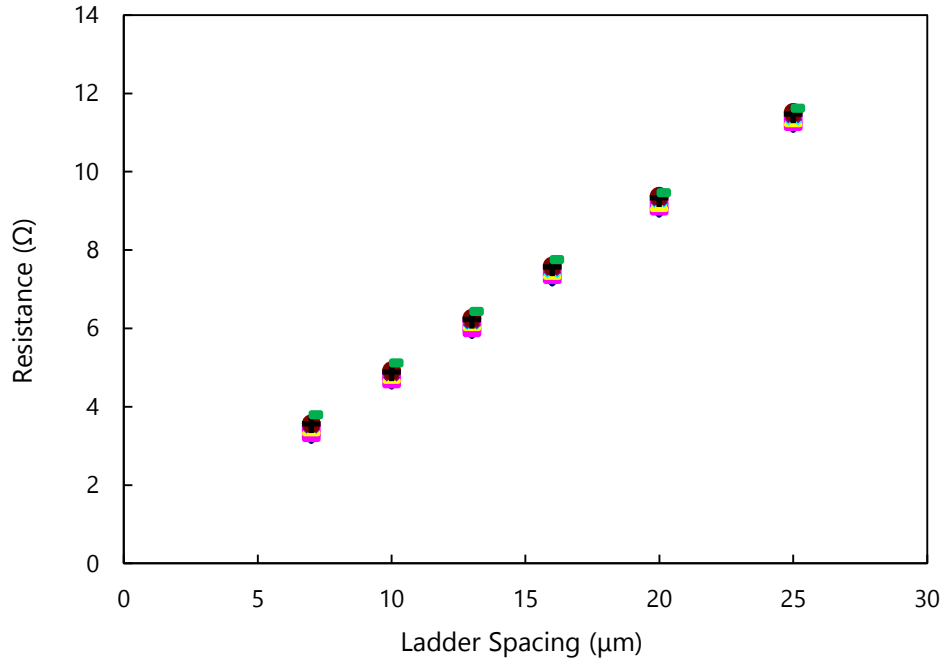
Figure 4.12. Resistance vs. ladder spacing for an oxidized 5 nm Ru / 5 nm Ni film (after 600 °C, 3 minute anneal). Each set of data points of the same shape and color represents one entire ladder.

4.2 GaInN/GaN Absorbers

Most GaInN/GaN solar cells reported to date have been prepared via *heteroepitaxy – that is, growth of nitride semiconductor films on foreign substrates* (e.g., sapphire) – because bulk GaN wafers have only recently become available (and they are very expensive > $3,000 per 2 inch diameter wafer). Sapphire is one of the few substrate materials that can withstand the extreme temperatures required for epitaxial growth (greater than 1000 °C for high-quality GaN prepared via MOCVD). Unfortunately, the best possible c-plane alignment still leaves a 13.9% lattice

parameter mismatch between Al_2O_3 and GaN, giving rise to a dense tangle of dislocations near the interface. A significant fraction of these dislocations extend upward through the device active region and hence are referred to as "threading" dislocations. The areal density of threading dislocations (N_{TD}) is known to be quite high in all GaN-based electronic material structures prepared via heteroepitaxy. For example, N_{TD} is typically larger than 10^9 cm^{-2} in commercial GaN/GaInN LEDs emitting photons in the $340 \leq \lambda \leq 540$ nm spectral range.

Such large values of N_{TD} would be expected to degrade "best-case" solar cell performance by decreasing carrier lifetime and mobility, both of which should reduce photo-carrier collection efficiency. In addition, a localized cluster of threading dislocations would likely result in high dark current (at low forward bias) which should lead to a reduction in open circuit voltage. Moreover, owing to the large junction areas required for solar cells, a non-uniform *distribution* of threading dislocations could give rise to substantial variations in performance (even between devices fabricated next to each other). Finally, as these solar cells contain absorbing regions made from the GaInN ternary alloy system, with its highly mismatched binary endpoints, the possibility of phase separation cannot be ignored. The resulting inhomogeneous distribution of indium would give rise to local variations in E_G that could negatively impact carrier collection. It is important to emphasize that *these shortcomings are intrinsic to the material* and are therefore characteristic of contemporary GaInN/GaN solar cells grown by MOCVD or MBE techniques.

4.2.1 Synthesis & Characterization

The solar cell materials used in this work were generously provided by Kopin Corporation. The epitaxial layers were grown in a commercial MOCVD reactor dedicated to the synthesis of GaN/AlGaN high electron mobility field-effect transistors (consequently, this reactor does not have p-type doping capability). It is important to emphasize that the GaInN/GaN material

42

structures under consideration were designed for use in *Schottky diode* solar cells and thus have an unusual *i-i-n* doping configuration (i.e., there is no p-type doping anywhere in the structure).

The precursor chemicals, trimethyl-gallium, trimethyl-indium, ammonia, and disilane, were used in a mixed hydrogen/nitrogen gas ambient held at a chamber pressure of 300 torr. Using the two-step method, a thin GaN buffer layer was first deposited at low temperature on c-plane sapphire followed by a 4 μm Si-doped *n*-layer of GaN (with $[\text{Si}] = 2 \times 10^{18}$ cm^{-3}) grown at high temperature to achieve good structural quality. Next, an unintentionally doped (*i*-layer) GaInN/GaN absorber region was grown in one of two configurations. Sample VT_365 contains a GaN/GaInN/GaN double-heterostructure (DH) absorber with a single 200 nm thick $Ga_{0.9}In_{0.1}N$ alloy layer. Sample VT_367 contains a GaInN/GaN MQW absorber with fifteen 2.5 nm thick $Ga_{0.9}In_{0.1}N$ quantum wells separated by sixteen 12 nm thick GaN barriers. Finally, a 67 nm undoped layer (*i*-layer) of GaN was deposited on top to serve as the material in intimate contact with the Schottky electrode.

Photoluminescence (PL) measurements were performed at 300 K to assess the "as-grown" material prior to device fabrication. The PL spectra shown in Figure 4.13 reveal a local maximum at a wavelength of 365 nm with a narrow line width (both samples), indicative of high-quality GaN. A second intense but broad PL peak is also observed, corresponding to emission from the GaInN/GaN absorber regions ($\lambda = 420$ nm and 438 nm for VT_365 and VT_367, respectively). The associated spectral line widths are 24 nm for the former and 14 nm for the latter; suggesting the DH absorber in VT_365 is of lower overall quality than the MQW active region in VT_367. Further evidence of lower quality material in VT_365 is the very broad

peak centered at 560 nm, which is attributable to transitions mediated by point defects within the bulk $Ga_{0.9}In_{0.1}N$ layer.
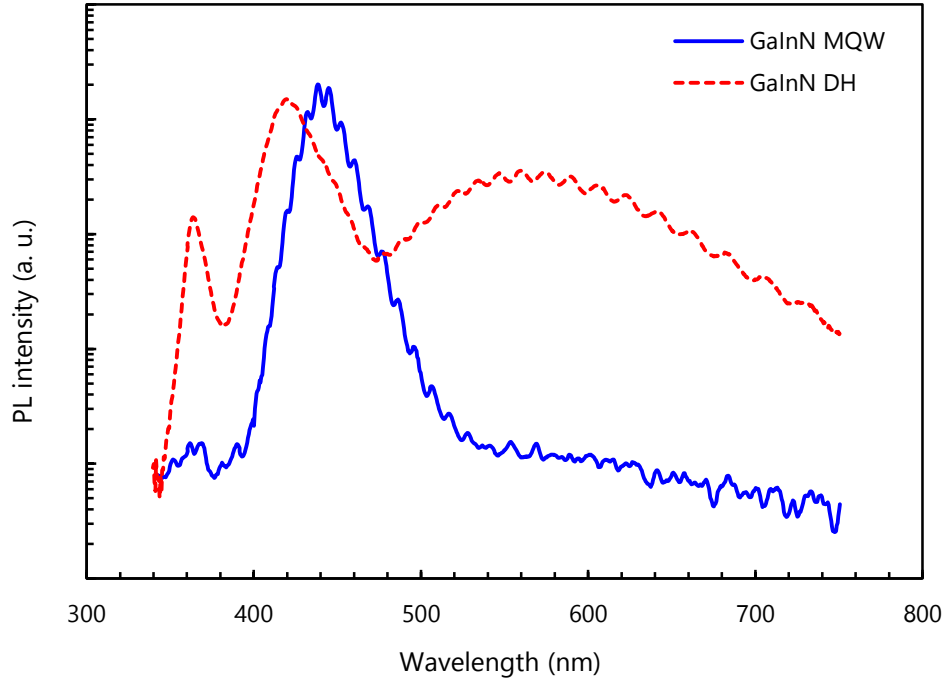
Figure 4.13. Room temperature PL spectra for VT_365 (GaInN DH) and VT_367 (GaInN MQW). Measurements were taken using an Accent RPM 2000 wafer mapping system.

Optical transmission spectra for VT_365 and VT_367 are shown in Figure 4.14 (along with data for a 2 μm thick GaN reference sample). Light transmission drops to zero at 365 nm (for all three samples) owing to strong absorption in the thick GaN layers. Introduction of the GaInN/GaN active regions shifts the onset of absorption to roughly 430 nm, enabling additional capture of lower energy photons. Sample VT_365 is less transparent (more absorbing) compared to VT_367 at wavelengths between 365 and 430 nm. This observation is not surprising given the relative thicknesses of GaInN alloy material in the two samples (200 nm in VT_365 vs 37.5 in VT_367). Nonetheless, in both cases, the total GaInN thickness would have to be increased to

achieve complete absorption of photons with $\lambda < 430$ nm. Accomplishing this feat without further degrading material quality is a major technical challenge.
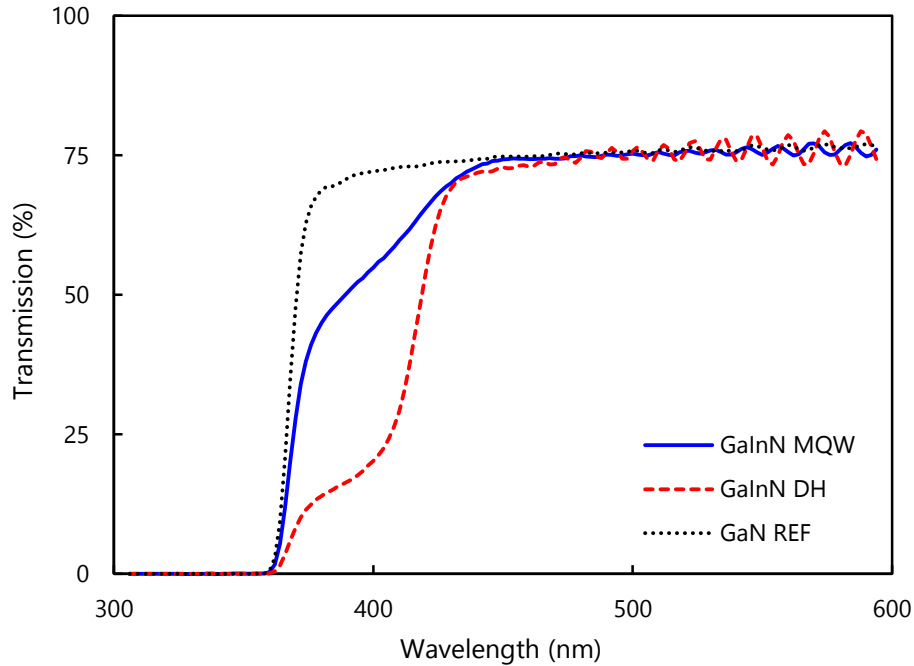
Figure 4.14. Optical transmission spectra of VT_365 (GaInN DH), VT_367 (GaInN MQW) and a reference GaN sample. Samples were measured prior to processing, in their as grown states.

4.3 GaInN/GaN Schottky Solar Cells

4.3.1 Device Layout & Fabrication

Solar cells were fabricated at Virginia Tech in the Micron Technology Semiconductor Processing Lab using a custom lithographic mask generated via L-Edit software (a commercial product from Tanner Tools). Wafer sections approximately 3 cm^2 in total area were processed yielding about 60 devices per fabrication run. Samples were cleaned under ultrasonic agitation with acetone followed by isopropyl alcohol, and then rinsed in de-ionized water. They were then soaked in aqua regia (3:1 HCl : HNO$_3$) followed by concentrated HF acid to etch off residual metals and the native oxide. Next, a thick nickel mask was deposited via electron-beam

deposition and patterned using a photolithographic liftoff process. The samples were dry etched (ICP process with BCl$_3$/Cl$_2$ gas mixture) through the GaInN/GaN active region to form mesas and to expose the n$^+$ GaN layer for ohmic contact formation. The nickel etch mask was stripped off using aqua regia and the samples were then dipped in buffered oxide etch to remove the native oxide. Next, a 30 nm Ti / 400 nm Al metal bilayer was deposited using electron-beam evaporation and patterned via photoresist lift-off. Thermal annealing was performed at 600 ℃ for 3 minutes in forming gas to achieve low contact resistance. Samples were again dipped in buffered oxide etch to remove the native oxide, and then the Schottky electrode material was deposited (patterned) on the mesas (top surface only) by electron-beam evaporation (photoresist lift-off); 10 nm of Pt *or* 5 nm of Ni followed by 5 nm of Au *or* 5 nm of Ru followed by 5 nm of Ni. The Pt films were left in their as-deposited state. The Ni/Au and Ru/Ni bilayers were oxidized at 500 ℃ (10 minutes) and 600 ℃ (3 minutes), respectively. Finally, a thick 50 nm Ni / 400 nm Ag metal bilayer was deposited on the Schottky electrode and patterned to form (periodic) low-resistance metal traces. Additional fabrication details can be found in Appendix A. A schematic illustration of a fully processed solar cell is presented in Figure 4.15.
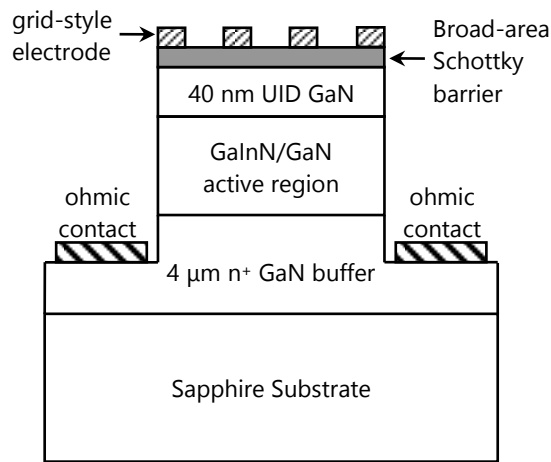
Figure 4.15. Schematic cross-section of a fully processed GaInN/GaN Schottky solar cell.

The photo-mask layout was designed to create four different solar cell geometries, adjacent to one another in a 2.5 x 2.5 mm^2 subfield region, which are repeated in a 6 x 6 array to make up the complete lithographic pattern. The four device architectures can be separated into two categories: a *finger* geometry and a *grid* geometry, each with two different pitch values for finger mesa separation or grid trace line spacing. The four geometrical structures are referred to hereafter as "Coarse Finger" (CF), "Fine Finger" (FF), "Coarse Grid" (CG), and "Fine Grid" (FG). Nomarski optical images of completed solar cell devices are shown in Figure 4.16. Each geometry was repeated about sixteen times across one 3 cm^2 sample to evaluate process uniformity and to increase device yield per fabrication run.
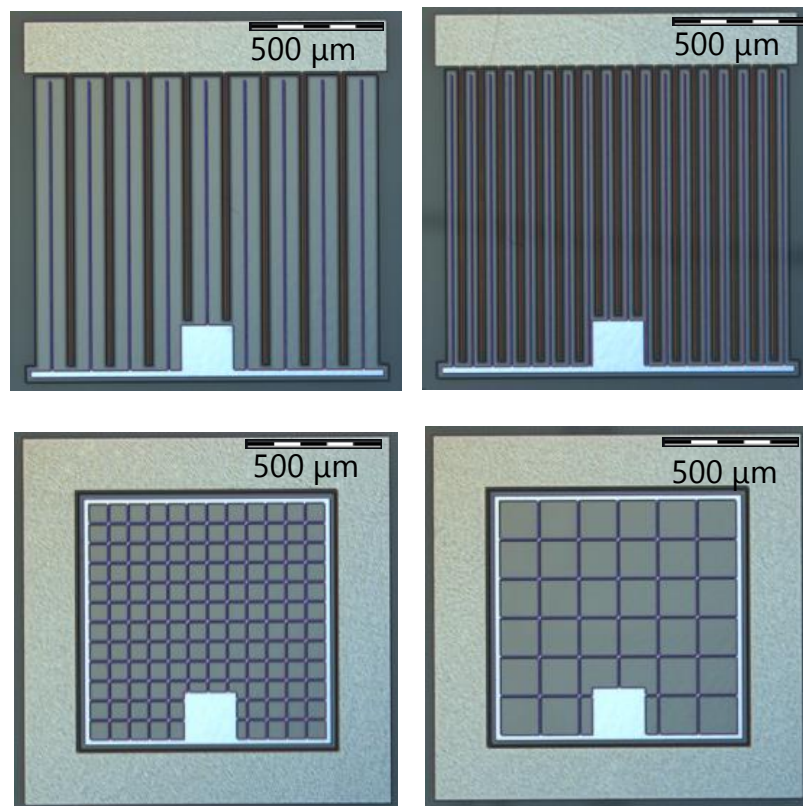
Figure 4.16. Nomarski phase contrast images in plan-view of completed solar cell devices CF (top left), FF (top right), FG (bottom left), and CG (bottom right).

In the case of solar cells having the finger geometry, there are two different pitch values separating the *finger-like* mesas (FF = 75 μm and CF = 150 μm). A 5 μm wide Ni/Ag trace along the centerline of each mesa finger helps to collect current from the thin Schottky electrode (covering the entire mesa finger), and transport it to the 200 μm x 200 μm Ni/Ag contact pad (bottom center). Each mesa finger is surrounded by 15 μm wide etched trenches with 5 μm wide Ti/Al ohmic contact traces running along their centerlines (to reduce series resistance from the n^+ GaN layer). A 200 μm wide Ti/Al bus bar extends across each device, serving as the common electrode for all ohmic contact traces. Electrical probing was done at the 200 μm wide bus bar (ohmic contact) and the 200 μm x 200 μm square pad (Schottky electrode).

For solar cells having the grid geometry, there are two different pitch values for the *grid-like* trace spacing (FG = 75 μm and CG = 150 μm). In this case, there is only one single (large-area) square mesa and the thin Schottky electrode covers its entire surface. A collection of 5 μm wide Ni/Ag metal traces are arranged in a crossbar pattern to help transport current from the Schottky electrode to the 200 μm x 200 μm Ni/Ag contact pad (bottom center). The ohmic contact takes the form of a 200 μm wide Ti/Al bus ring that encircles the entire mesa area.

A summary of the relevant device areas for each geometry can be found in Table 4.1. It is clear that the CF geometry has the largest illuminated area followed by the FF, CG, and finally FG case. Under ideal circumstances, the short circuit currents should follow the same order as the illuminated mesa areas with the CF and FG geometries exhibiting the largest and smallest I_{SC} values, respectively.

Device Geometry	Pitch Spacing (µm)	Total Mesa Area (mm^2)	Illuminated Area (mm^2)
Coarse Finger (CF)	150	1.36	1.240
Fine Finger (FF)	75	1.11	0.940
Coarse Grid (CG)	150	0.960	0.808
Fine Grid (FG)	75	0.960	0.759

Table 4.1. Summary of pitch spacing, total mesa area, and illuminated mesa area (unshaded region) for all four device geometries.

4.3.2 Testing Methods & Apparatus

In preparation for electrical testing samples were examined under a Nomarski phase contrast microscope to identify physical defects including mesa deformities associated with plasma etching (due to Ni mask patterning), poor adhesion of metal layers (evidenced by broken or incomplete Ni/Ag trace lines), and other processing irregularities (caused by photoresist buildup near sample edges). Such abnormalities would skew testing results, so devices exhibiting them were excluded from further consideration.

Preliminary electrical testing was performed using tungsten metal probes in a 4-point measurement arrangement (two source probes, two sense probes) attached to a Keithely 2400 SMU in Dr. Lou Guido's characterization laboratory at Virginia Tech. Data collection and measurement control was handled by a computer using a custom program written in LabView which communicated with the Keithley 2400 SMU. Samples were illuminated using a cluster of LEDs with a central wavelength of 398 nm and illumination intensity of 13 mW/cm^2. This illumination source gives direct insight into the quality of the GaInN absorber material as the surrounding GaN does not absorb photons at this wavelength. Light power intensity was independently verified with a Newport 818-UV photodetector attached to a Newport 2832-C light power meter. Electrical testing with this apparatus has been verified to be reproducible

within 1% through comparison of I-V measurements preformed on TLM ladder structures and Schottky diodes.

LED illuminated I-V testing was carried out on all "clean" devices to evaluate sample uniformity and to screen out solar cells not worthy of additional testing. Devices with high reverse leakage current, which may be indicative of localized areas of poor quality "as-grown" material or of non-visible processing related defects, were excluded from further analysis.

Electrical testing under calibrated solar radiation was performed at MicroLink Devices in Niles, IL. Samples were illuminated using a Newport AM1.5G solar spectrum simulator at 1-Sun intensity (verified using a Newport solar intensity power meter and a reference Si solar cell). I-V measurement was coordinated and data collected using a Keithley SMU in a two-point probe configuration controlled by a computer. Full sample characterization was not possible as these measurements were made in a manufacturing environment with limited availability to the equipment. Instead two solar cells for each geometrical configuration (total of eight devices) were selected for testing on the basis of their "best-in-class" performance under LED illumination.

4.3.3 Measurement Results

Given the simplicity of single-layer, as-deposited Pt Schottky electrodes, along with the results of GaInN/GaN absorber evaluation via PL measurements, the decision was made to define "10 Pt VT_367" as the internal reference against which to compare other devices made at Virginia Tech (this notation is compact and yet identifies both Schottky electrode material and GaInN/GaN absorber structure).

10 Pt VT_365 *vs* 10 Pt VT_367

Current vs. voltage curves under LED illumination are shown in Figure 4.17 for a set of 10 Pt VT_367 *reference* solar cells. A decision was made to present data for the CG device geometry only in the interest of brevity. Each curve represents a distinct solar cell. Nine devices in total were analyzed as the rest were either leaky or suffered from physical defects.
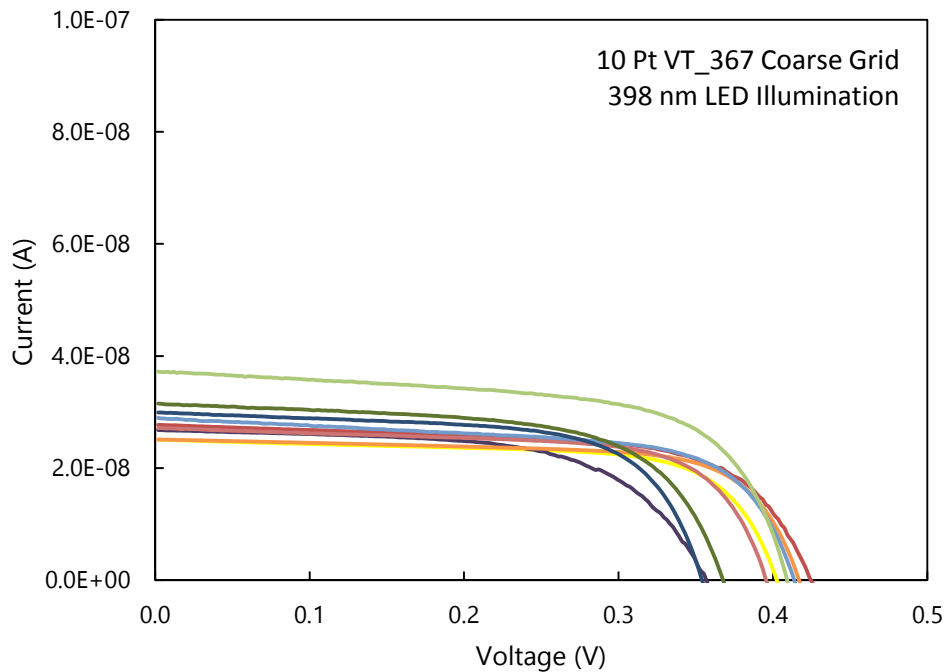
Figure 4.17. Measured I-V curves for 10 Pt VT_367 CG solar cells under 398 nm LED illumination. Each curve represents a distinct device and thus illustrates variability across the sample.

The most striking finding is that I_{SC} is very low (28.8 $\pm$ 3.8 nA). However, one must keep in mind that the LED source intensity is only 13 mW/cm^2 and that photons with $\lambda \approx$ 398 nm are absorbed only by the GaInN quantum wells (15 QWs x 2.5 nm per QW = 37.5 nm in total thickness). The second important result is that V_{OC} is lower than anticipated (0.39 $\pm$ 0.03 V), given the barrier height and ideality factor reported herein for Pt Schottky electrodes on n-type GaN (φ = 1.12 eV, n = 1.06). The last observation is the extent to which I_{SC} and V_{OC} vary across

51

the sample. The degree of variation shown here for the CG case is similar to that observed for the other device geometries.

Figure 4.18 shows I-V characteristics under LED illumination for 10 Pt VT_365 CG solar cells with CG geometry. It is immediately evident that I_{SC} is quite broadly distributed and yet in all cases it is substantially larger than values obtained for 10 Pt VT_367 (from 4x on the low side to 64x on the high side). Solar cells having the DH absorber should exhibit larger I_{SC} compared to the MQW case due to its larger GaInN thickness. It is also obvious that V_{OC} is *really small* in comparison to 10 Pt VT_367. Large I_{SC} in combination with small V_{OC} is contrary to theoretical predictions for an ideal Schottky solar cell. In practice, however, such coupling between I_{SC} and V_{OC} would occur in the presence of a large shunt conductance.
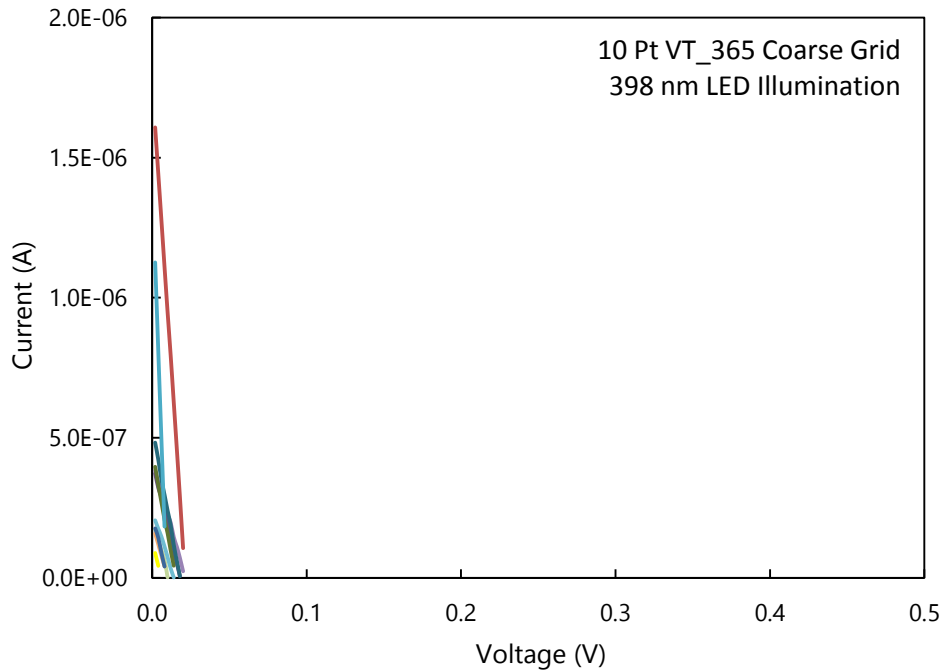
Figure 4.18. Measured I-V curves for 10 Pt VT_365 solar cells under 398 nm LED illumination. Each curve represents a distinct device and thus illustrates variability across the sample.

52

Schottky diodes fabricated from highly defective semiconductor material should exhibit "leaky" reverse blocking characteristics combined with a high forward bias current at low voltages. This is in fact the case as evidenced in Figure 4.19 by *dark* I-V curves for a large number of 10 Pt VT_365 CG solar cells. Not only are the forward currents at low voltages comparable to the short circuit currents observed in Figure 4.18, but forward and reverse operating characters are similar, indicating very poor reverse current blocking characteristics.
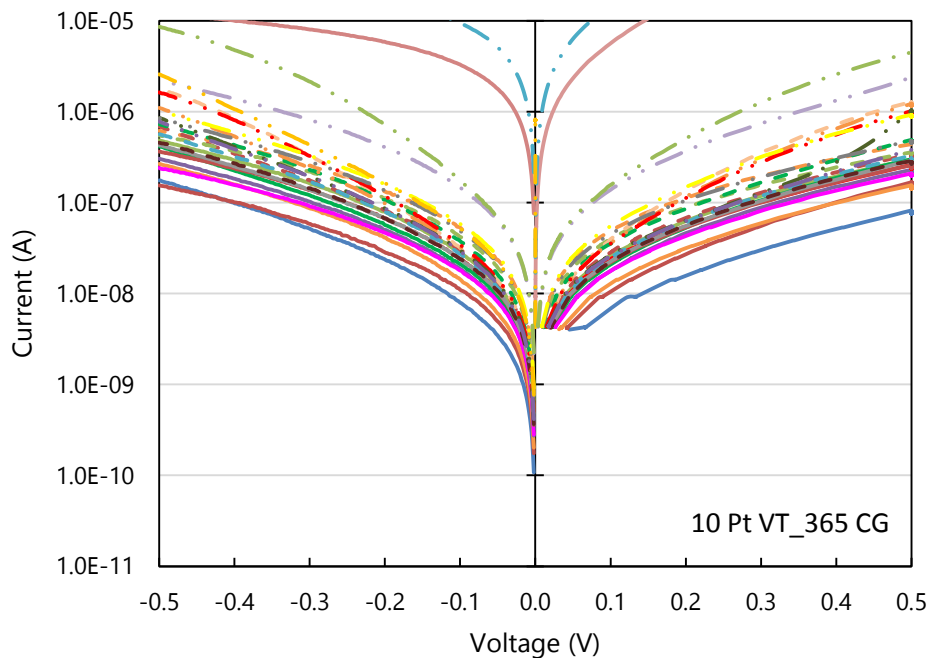
Figure 4.19. Dark current measurements (no illumination) under forward and reverse bias for 10 Pt VT_365 solar cells. Measurement error is responsible for the absence of data in the low current, low voltage forward bias regime.

While the results presented for 10 Pt VT_365 solar cells are poor, they are not wholly unexpected. Recall that critical thickness calculations for $Ga_{0.9}In_{0.1}N$ suggest film thicknesses in excess of 10 nm are likely to exhibit some material relaxation. At a thickness of 200 nm, stress caused by the lattice mismatch between GaN and $Ga_{0.9}In_{0.1}N$ is simply too great, resulting in highly defective material whose quality is unsuitable for making solar cells. As a consequence of

these findings, the GaInN/GaN DH absorber, and solar cells made therefrom, will not be given further consideration.

Moving forward with only the GaInN/GaN MQW absorber, a set of "champion" devices were subjected to additional testing. Figure 4.20 shows I-V curves for eight 10 Pt VT_367 solar cells (two each of the CF, CG, FG and FF geometry) under 1 Sun, AM1.5G illumination.
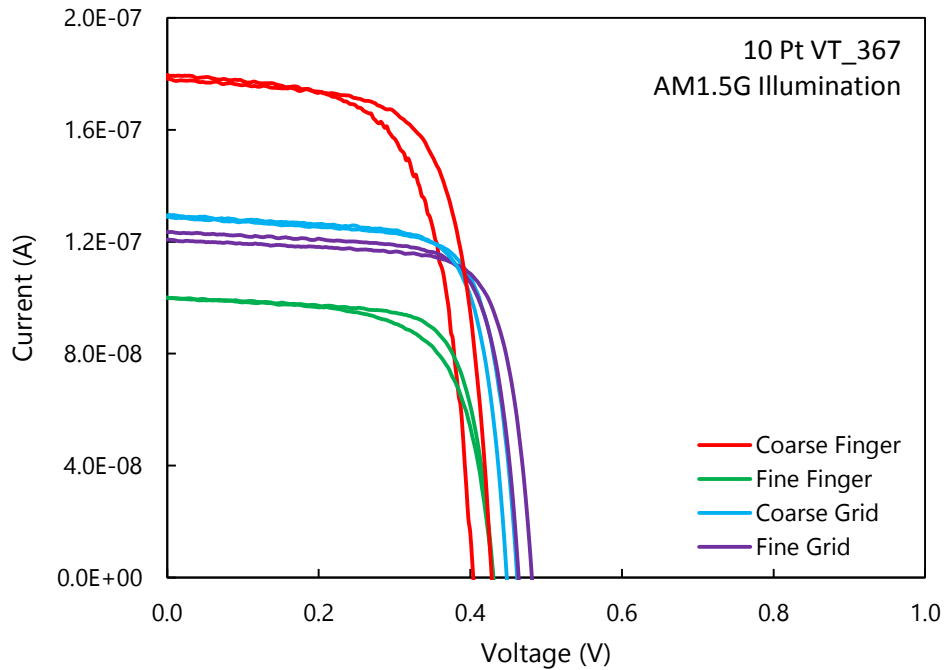
Figure 4.20. I-V characteristics for the best two solar cells from each geometry on 10 Pt VT_367 under AM1.5G illumination.

Consistent with expectations, the short circuit current for CG solar cells under AM1.5 illumination is larger (about 4x) than the average I_{SC} found when using 398 nm LED excitation. The corresponding small increase in open circuit voltage – *that is, the weak coupling between I_{SC} and V_{OC}* – is in accordance with ideal Schottky solar cell behavior. It is also obvious that I_{SC}, and to a lesser extent V_{OC}, can be influenced by device geometry. Using the I_{SC} x V_{OC} product as a

first-order means of comparison, the CF architecture gives the best performance (CF = 0.08 / CG = 0.06 / FG = 0.06 / FF = 0.04 in units of 10^{-6} W).

5/5 NiAu VT_367 *vs* 10 Pt VT_367

The combination of GaInN/GaN MQW absorber with oxidized Ni/Au Schottky electrode was tested next to evaluate the connection between Schottky electrode material and solar cell performance. I-V characteristics are shown in Figure 4.21 for eight "champion" 5/5 NiAu VT_367 solar cells tested under AM1.5G (1-Sun) illumination.
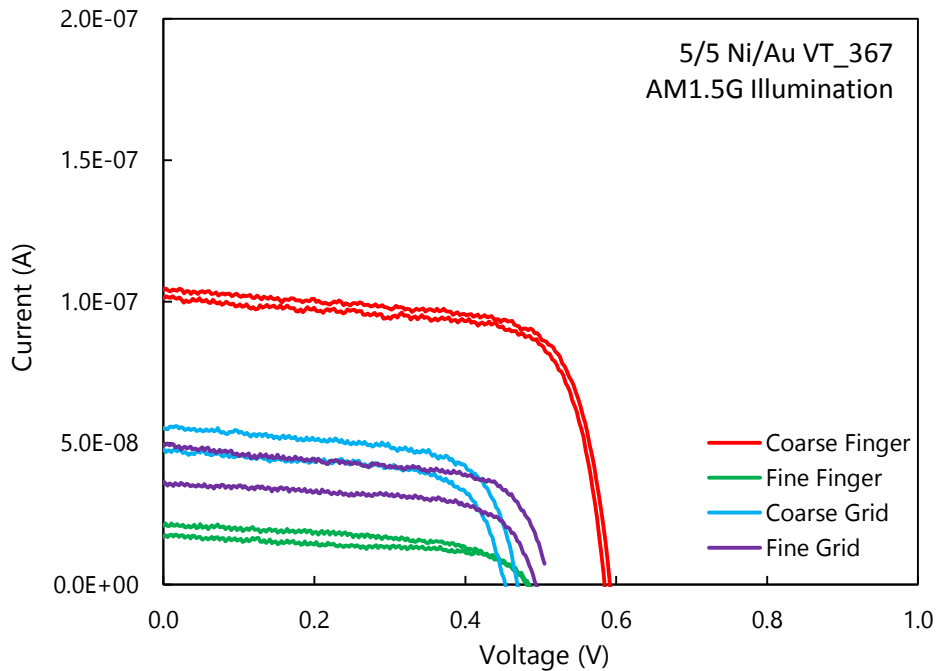
Figure 4.21. I-V characteristics for the best two solar cells from each geometry on 5/5 NiAu VT_367 under AM1.5G illumination.

The observed I_{SC} values are low in comparison to 10 Pt VT_367 devices, which is surprising given the higher optical transparency and lower electrical sheet resistance of the oxidized Ni/Au Schottky electrode. We speculate that this may be caused by trapping of photo-generated holes at the Schottky interface, resulting in a lower carrier collection efficiency. Other workers have

shown that oxidized Ni/Au films on GaN are composed of Au nanoparticles embedded within a NiO matrix [43]. Crystalline nickel oxide is known to be a wide bandgap semiconductor ($E_G \approx$ 4.0 eV); hence, it is possible that the energy band alignment at the Schottky interface creates a potential notch for holes [42]. The observed V_{OC} values for 5/5 NiAu VT_367 solar cells are similar to those found in the 10 Pt VT_367 devices, except for the CF geometry which exhibits a 40% larger open circuit voltage (V_{OC} = 0.59 and 0.42 V for the 5/5 NiAu and 10 Pt cases, respectively). Once again, the CF device geometry gives the best I_{SC} x V_{OC} product (CF = 0.06 / CG = 0.02 / FG = 0.02 / FF = 0.01 µW).

5/5 RuNi VT_367 *vs* 10 Pt VT_367

The final type of Schottky solar cell evaluated herein combines a GaInN/GaN MQW absorber with an oxidized Ru/Ni Schottky electrode. This device architecture is of interest because ruthenium oxide is known as a transparent conducting oxide (TCO) − *giving a third class of material for Schottky electrodes*. The other two cases being Pt, a simple metal, and oxidized Ni/Au, a wide bandgap semiconductor with its electrical conductivity enhanced by randomly dispersed Au nanoparticles.

Before settling on Ru/Ni bilayers, we studied Ru-only films (10 nm) prepared using the same deposition and oxidation methods. These Schottky electrodes are more opaque than their oxidized Ru/Ni counterparts, but have lower sheet resistance (111 $\pm$ 2.2 Ω/sq). Unfortunately, GaInN/GaN solar cells made using oxidized Ru-only Schottky electrodes do not perform well. This problem was addressed by reducing the ruthenium thickness (5 nm) and adding a nickel cover layer (5 nm) to make an oxidized Ru/Ni composite film. Others have shown that oxidized Ru/Ni makes good *ohmic* contact to *p-type* GaN (contact resistivity on par with the best Ni/Au

films *plus* better stability under accelerated aging [48-49]). Aside from pairing ruthenium (instead of gold) with nickel, the order of deposition is different – *in the Ru/Ni (Ni/Au) case, Ni is deposited last (first)*. After annealing in an oxidizing ambient, ruthenium metal is converted to RuO (in direct contact with the GaN surface) and the nickel film is transformed into NiO [48].

The results of electrical testing under AM1.5G (1-Sun) illumination are shown in Figure 4.22 for eight "champion" 5/5 RuNi VT_367 solar cells. The observed I_{SC} values are higher than in the Ni/Au case but lower than those found when using Pt Schottky electrodes. The former result can be attributed to better collection of holes relative to oxidized Ni/Au (with its NiO-to-GaN interface). The latter finding suggests that RuO in intimate contact with n-type GaN still presents some barrier to hole collection.
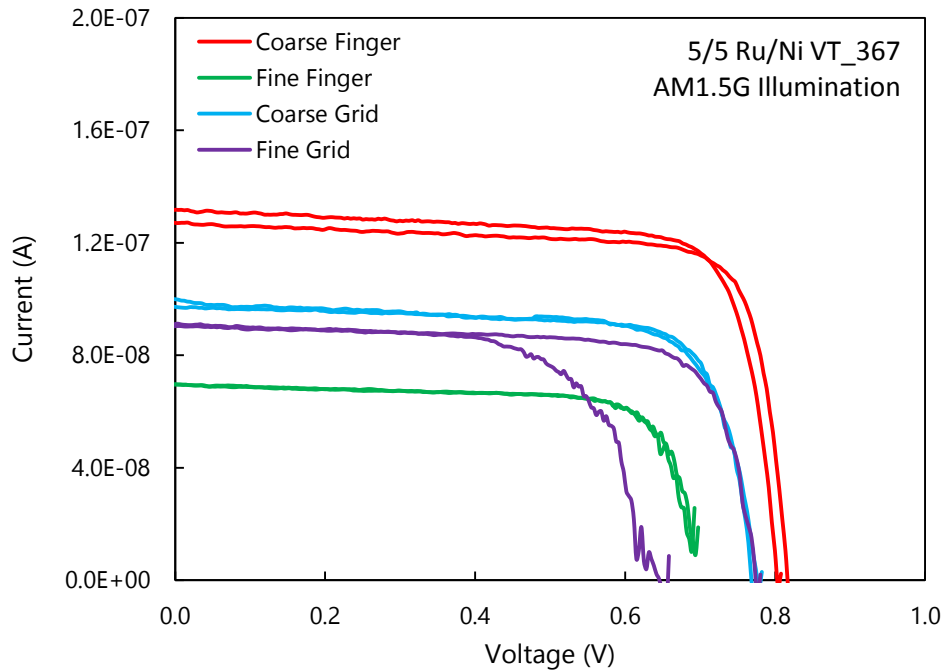
Figure 4.22. I-V characteristics for the best two solar cells from each geometry on 5/5 RuNi VT_367 under AM1.5G illumination.

With regard to open circuit voltage, it is obvious that 5/5 RuNi VT_367 solar cells have the largest values among the three cases under study. This behavior is not surprising given the Schottky barrier parameters reported in Section 4.1.1. The barrier height x ideality factor products follow the order: RuNi = 1.89 / NiAu = 1.44 / Pt = 1.19 eV. With regard to device geometry, the CF configuration remains the best choice in terms of I_{SC} x V_{OC} product (CF = 0.11 / CG = 0.08 / FG = 0.07 / FF = 0.05 μW).

5. ANALYSIS & DISCUSSION

All of the GaInN/GaN MQW Schottky solar cells described herein exhibit measureable photo-response accompanied by well-behaved I-V characteristics; the latter of which is evidenced in Table 5.1 by fill factors in the 70% range. Unfortunately, other aspects of device performance are not competitive with the best published results for GaInN p-*i*-n junction solar cells. First of all, short-circuit current densities, J_{SC}, are much too small. A second obvious problem is low open-circuit voltages. Taken together, these shortcomings give rise to power conversion efficiencies ~400x below the competition.

Schottky Electrode Material	V_{OC} (V)	J_{SC} (mA/cm^2)	Fill Factor	η
10 Pt	0.453	0.016	0.739	0.0053%
5/5 Ni/Au	0.461	0.006	0.654	0.0019%
5/5 Ru/Ni	0.772	0.012	0.747	0.0070%

Table 5.1. Experimental GaInN/GaN MQW solar cell parameters under AM1.5G illumination for each of three Schottky electrode materials (CG device geometry). The tabulated J_{SC} were obtained by dividing measured I_{SC} values by illuminated mesa areas.

In the remainder of this Chapter, an effort is made to determine to what extent the Schottky diode architecture, in combination with the chosen Schottky electrode materials, contribute to subpar device performance. Computer simulation of I-V characteristics, along with analytical treatment using circuit models, was performed to obtain benchmark solar cell parameters for comparison purposes.

5.1 Methods of Analysis

Computer simulations were done using APSYS. While APSYS is capable of 2D numerical analysis of semiconductor devices, 1D simulations were deemed adequate because device

geometry is clearly not the primary factor limiting solar cell performance. Within this framework, a broad-area Schottky electrode was implemented in the form of a "boundary condition" at the top surface of the GaInN/GaN absorber. This approach was employed – *instead of defining the Schottky electrode as a distinct material layer* – to achieve numerical convergence. The GaInN/GaN layer structure was specified using the most accurate materials parameters available in the literature [9, 53-61].

The impact on solar cell performance of two "parasitic" elements not addressed by APSYS simulations – *that is, electrical resistance associated with Schottky electrode materials and current leakage paths formed during crystal growth or device processing* – was evaluated using the circuit model shown in Figure 5.1.
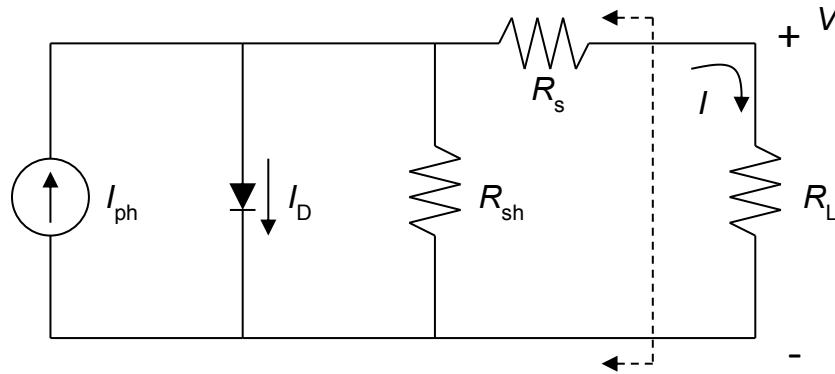
Figure 5.1. Equivalent circuit model for solar cell including both series resistance (R_s) and shunt resistance (R_{sh}).

Straightforward circuit analysis leads to Equation 5.1, which relates the current delivered to the load (I) to the voltage built up across the load (V).

$$I = I_{ph} - \left[ART^2 \left(e^{\frac{-q\varphi}{kT}} \right) \left(e^{\frac{q(V+R_S I)}{nkT}} - 1 \right) + \frac{V+R_S I}{R_{sh}} \right] \qquad (5.1)$$

Calculations were performed with different combinations of series resistance (R_s) and shunt resistance (R_{sh}) to determine when these factors begin to influence solar cell performance.

5.2 Factors Impacting J_{SC}

A benchmark I-V characteristic, obtained via APSYS computation, is shown in Figure 5.2 for a Schottky solar cell with the GaInN/GaN MQW absorber (VT_367). This *simulated representation of device performance* reflects the impact of several important physical mechanisms; such as, electron-hole pair generation (optical absorption) throughout the entire GaInN/GaN absorber, electron and hole separation (Coulomb attraction) within the junction depletion region, and electron and hole transport to device electrodes (ohmic and Schottky, respectively). Overall solar cell performance is summarized by the following extracted parameters: $J_{SC} = 0.051$ mA/cm^2, $V_{OC} = 0.50$ V, $FF = 0.559$, and $\eta = 0.014\%$. It is notable that the predicted J_{SC} is considerably larger than experimental values, which are summarized in Table 5.1 for comparison purposes. In this context, it is important to emphasize that this computer generated I-V characteristic does not account for some important factors:

1. Hole trapping at the Schottky electrode/semiconductor interface.
2. Optical losses (reflection, absorption) associated with the Schottky electrode.
3. Series resistance accompanying lateral current flow in the Schottky electrode.
4. Shunt conductance attributable to defects in the "as-grown" GaInN/GaN absorber or process flaws introduced during device fabrication.

The impact of each of these phenomena on GaInN/GaN Schottky solar cell performance is discussed in the following sections.
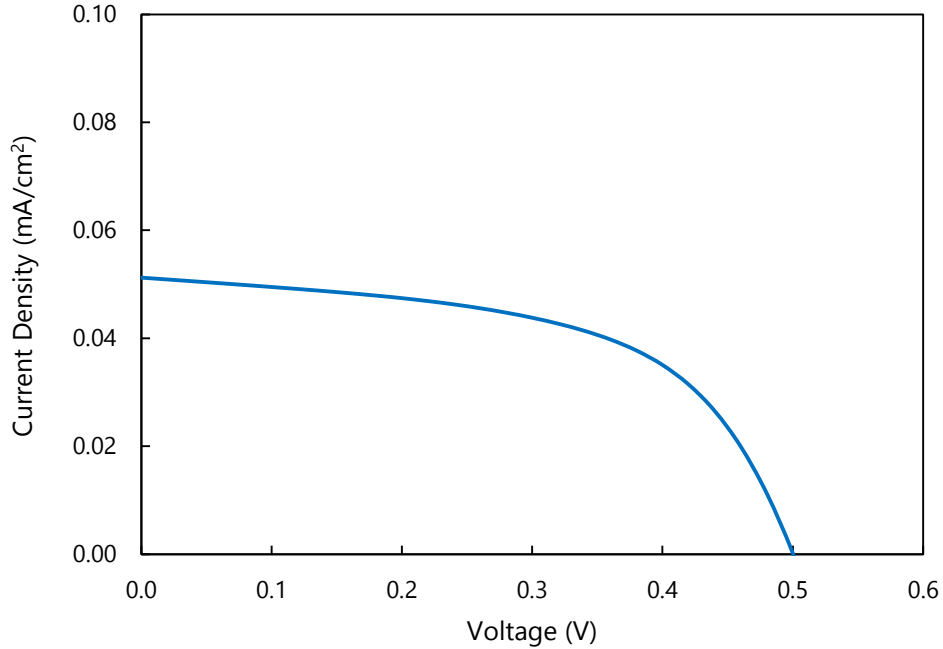
Figure 5.2. Computer simulated J-V curve for a GaInN/GaN Schotty solar cell under AM1.5G illumination. The device architecture consists of MQW absorber (VT_367) plus "ideal" Schottky barrier with $\varphi = 1.083$ eV.

5.2.1 Optical Filtering

A first order approximation can be made to include photon loss in the Schottky electrode by scaling J_{SC} using a theoretically derived correction factor. The total photo-generated current density is equal to the electron charge times the integral (over wavelength) of the product of the solar flux and the spectral response of the device structure. *For Schottky solar cells, the "spectral response" term includes electron-hole pair generation (optical absorption) plus electron/hole collection (carrier drift and diffusion) in both Schottky electrode and GaInN/GaN absorber.* If we consider an idealized case, however, in which *CCE* is unity in both the Schottky electrode and GaInN/GaN absorber, then scaling factors for "optical filtering" may be calculated using transmission spectra for Schottky electrodes, absorption coefficients for $Ga_{1-x}In_xN$ alloys [9], and the Beer-Lambert law. The latter is given by Equation 5.2, where *I* is the remaining light

intensity at distance, t, with incident intensity, I_0, transmitted through a material with absorption coefficient α (wavelength dependent).

$$I = I_0 e^{-\alpha t} \tag{5.2}$$

In order to allow for direct comparison, optical transmission data for all three Schottky electrodes were first normalized by the bare sapphire spectrum and then overlaid in Figure 5.3. These data show a clear preference for the 5/5 Ni/Au Schottky electrode, especially in comparison to the 10 Pt case.
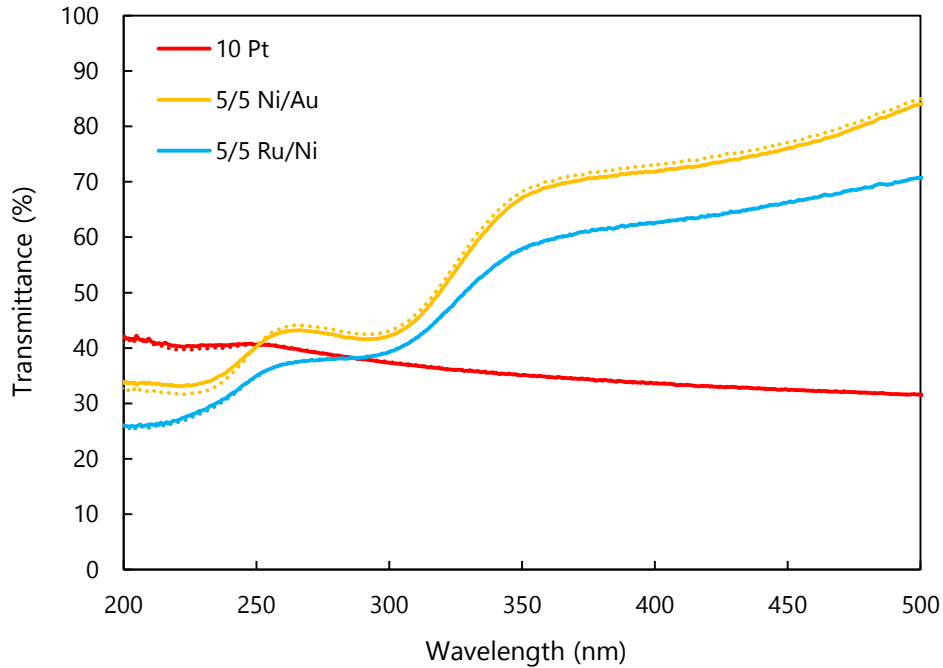
Figure 5.3. Corrected optical transmission spectra for 10 Pt, 5/5 Ni/Au, and 5/5 Ru/Ni Schottky electrodes. The raw (measured) data were normalized by the spectrum for a bare sapphire wafer.

Theoretical J_{SC} for all three Schottky solar cells (obtained by scaling the value from APSYS simulation) are given in Table 5.2. The predicted order of J_{SC} from lowest to highest is 10 Pt, 5/5 Ru/Ni, and 5/5 Ni/Au; however, such a trend is not observed experimentally for the actual

devices. The measured J_{SC} for the 10 Pt VT_367 solar cell is quite close to its theoretical (scaled) value suggesting that factors other than optical losses (associated with the Schottky electrode) do not have a strong influence on device performance in this particular case. In contrast, experimental J_{SC} values for both 5/5 NiAu VT_367 and 5/5 RuNi VT_367 solar cells are well below the corresponding theoretical predictions, especially for the 5/5 NiAu Schottky electrode case. The most plausible explanation for this difference is that *CCE* is significantly lower in both the 5/5 NiAu and 5/5 Ru/Ni solar cells compared to the 10 Pt case.

Schottky Electrode Material	Measured J_{SC} (mA/cm^2)	Scaled J_{SC} (mA/cm^2)	Ratio of J_{SC} (scaled) to J_{SC} (measured)
APSYS	–	0.051	–
10 Pt	0.016	0.018	1.13
5/5 Ni/Au	0.006	0.032	5.33
5/5 Ru/Ni	0.012	0.029	2.42

Table 5.2. Measured and scaled (theoretical) J_{SC} for GaInN/GaN MQW solar cells with Pt, Ni/Au, and Ru/Ni Schottky electrodes. Scaled values were derived through calculation of optical loss using the transparency spectra shown in Figure 5.3 and the J_{SC} derived from APSYS.

5.2.2 Carrier Collection

Given the much lighter effective mass of electrons in the GaInN material system compared to that of holes, as well as the absence of any potential barrier to electron transport at the interface between the GaInN/GaN MQW absorber and the n$^+$ GaN region, it is reasonable to posit that hole trapping at the Schottky interface is responsible for low *CCE* (and thus lower than predicted J_{SC}) in solar cells with oxidized Ni/Au and Ru/Ni Schottky electrodes. Further evidence of a Schottky interface related barrier to hole transport was found by examining two additional configurations that represent limiting cases for the Ru/Ni based devices. A set of GaInN/GaN MQW solar cells with *oxidized* Ru-only or Ni-only Schottky electrodes were prepared and tested

as described previously. I-V characteristics are shown in Figure 5.4 for 10 Ru VT_367 and 10 Ni VT_367 solar cells (along with original data from the 5/5 RuNi VT_367 case). Short-circuit current densities for 10 Ru and 5/5 RuNi solar cells are very similar, but J_{SC} for the 10 Ni case is extremely low. These observations support the claim that a NiO-to-GaN interface presents a substantial barrier to the collection of photo-generated holes.
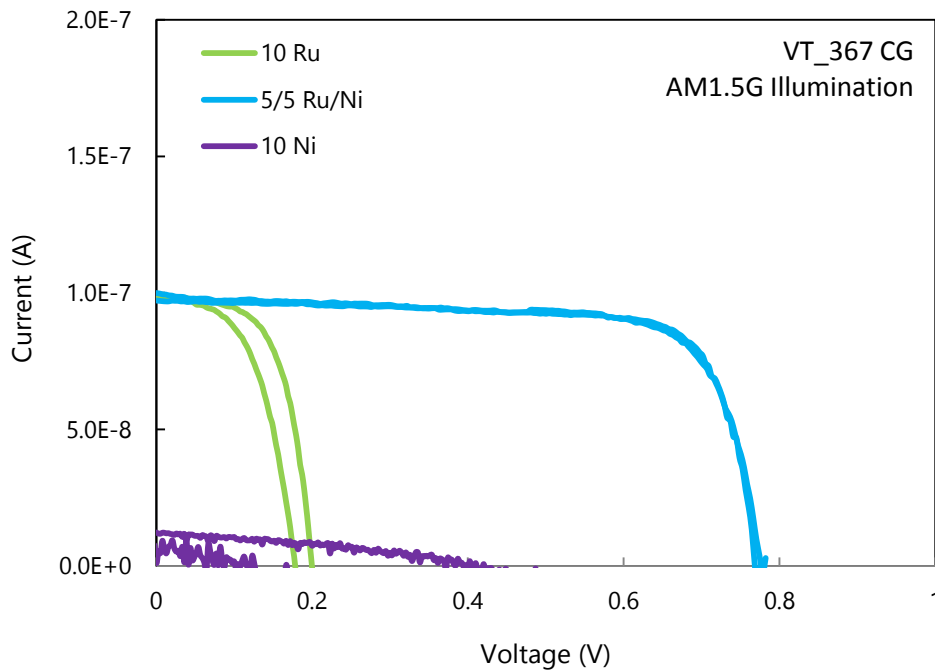
Figure 5.4. I-V Characteristics for the best two 10 Ru VT_367 and 10 Ni VT_367 solar cells under AM1.5G illumination (CG geometry). Additional I-V curves from 5/5 Ru/Ni VT_367 solar cells (CG) are overlaid for comparison.

Following the methodology described earlier, the impact on J_{SC} of *optical filtering* by oxidized Ru and Ni Schottky electrodes was calculated with the aid of transmittance spectra shown in Figure 5.5. The 10 nm Ru and 10 nm Ni films were *oxidized* in normal laboratory air at 600 °C (3 min) and 500 °C (3 min), respectively. It was proven empirically that these oxidation conditions give the lowest R_{SH} without sacrificing optical transparency. Note that the oxidized Ni (Ru) films are greater than 85% (45%) transparent for wavelengths longer than 365 nm.
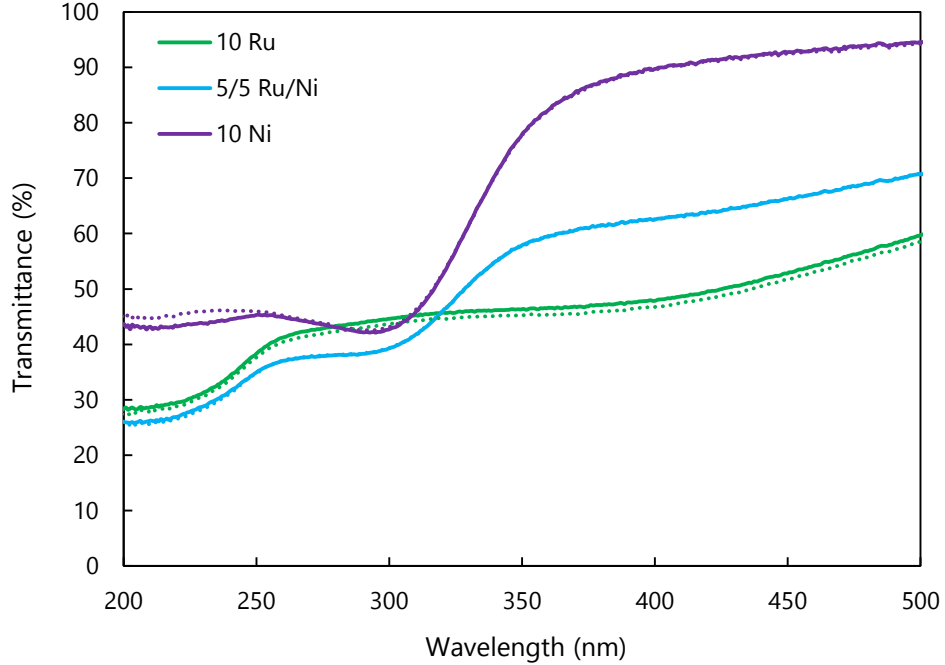
Figure 5.5. Corrected optical transmission spectra for 10 Ru and 10 Ni Schottky electrodes. For comparison, the correct optical transmission of the 5/5 Ru/Ni Schottky electrode is also provided. The raw (measured) data were normalized by the spectrum for a bare sapphire wafer.

The results of this analysis are summarized in Table 5.3. The scaled values of J_{SC} increase in order from 10 Ru, 5/5 Ru/Ni, to 10 Ni. The 10 Ru VT_367 solar cell appears to have a smaller barrier to hole transport compared to 5/5 RuNi VT_367, as their experimental J_{SC} values are similar despite higher transmittance of the Ru/Ni Schottky electrode. Once again, these findings support the notion that a NiO-to-GaN Schottky interface is detrimental to solar cell performance.

Schottky Electrode Material	Measured J_{SC} (mA/cm^2)	Scaled J_{SC} (mA/cm^2)	Ratio of J_{SC} (scaled) to J_{SC} (measured)
APSYS	–	0.051	–
10 Ru	0.012	0.023	1.92
5/5 Ru/Ni	0.012	0.029	2.42
10 Ni	-	0.039	2.42

Table 5.3. Measured and scaled (theoretical) J_{SC} for GaInN/GaN MQW solar cells with Ru-only and Ni-only Schottky electrodes. For comparison, the 5/5 Ru/Ni values are also provided. Scaled values were derived through calculation of optical loss using the transparency spectra shown in Figure 5.3 and the J_{SC} derived from APSYS.

Another key finding is that 10 Ni VT_367 solar cells have very poor fill factors, which is attributable to the enormous (lateral) series resistance associated with the NiO Schottky electrode. It was not possible to make reliable I-V measurements on 10 nm thick oxidized Ni test films (patterned in the TLM ladder configuration), because the 200 V compliance limit of the Keithley 2400 SMU was exceeded at the minimum source current of 50 pA. This implies that R_{SH} of such thin NiO films is greater than 10^{11} Ω/sq and correspondingly that 10 Ni VT_367 devices suffer from large "parasitic" series resistance.

5.2.3 Series Resistance

A large equivalent resistance connected in series between the solar cell proper and the load can suppress the net current delivered by the solar cell to the load, and thereby lead to a reduction in short-circuit current. If this were the case, however, then the overall I-V characteristic should be severely distorted which would be reflected by a sharp decrease in fill factor. In order to demonstrate this connection, a set of "theoretical" I-V curves was generated using Equation 5.1 with R_s as the variable parameter [62]. Figure 5.6 shows that as R_s approaches a value of 8.9 x 10^6 Ω, obtained from dividing V_{OC} by I_{SC}, it progressively makes more of an impact on solar cell performance. The resulting device parameters are summarized in Table 5.4 – the suppression of J_{SC} (and FF) is obvious. It is also interesting that increasing R_s from 1 to 10^5 Ω does not yield a large change in I-V curve shape or in extracted device parameters. Hence, unless the solar cell characteristic is really distorted, it is not particularly useful to compare R_s values obtained in this fashion.

Recall that sheet resistances for the Schottky electrodes examined herein are not very different with R_{SH} = 56, 28, and 171 Ω/sq for the 10 Pt, 5/5 Ni/Au, and 5/5 Ru/Ni cases, respectively. For the grid-style device geometry, with crossbar metal traces surrounding square tiles of Schottky

electrode material, these R_{SH} values can be taken as R_s (in ohms) for this component of the total series resistances.
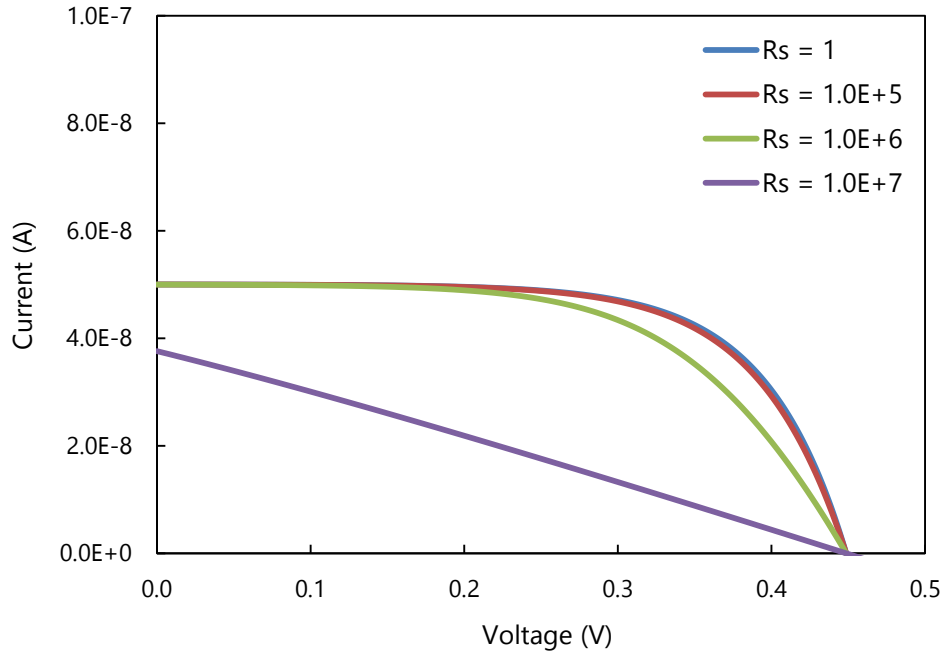
Figure 5.6. Theoretical I-V characteristics for different values of series resistance (R_s) in ohms.

The other contribution to series resistance comes from the bottom-side n$^+$ GaN layer with its R_{SH} value of roughly 32 Ω/sq. Once again, the square mesa shape of our devices means that R_s is about 32 Ω for this component of total series resistance. So, taken together these two contributions to R_s do not sum to more than a few hundred ohms. These findings explain why the fill factors are quite respectable for the 10 Pt VT_367, 5/5 NiAu VT_367, and 5/5 RuNi VT_367 solar cells.

R_s	I_{SC} (A)	V_{OC} (V)	Fill Factor	η
1	5.0×10^{-8}	0.446	0.667	0.0015%
1×10^5	5.0×10^{-8}	0.446	0.659	0.0015%
1×10^6	5.0×10^{-8}	0.446	0.586	0.0014%
1×10^7	3.8×10^{-8}	0.446	0.199	0.0003%

Table 5.4. Device parameters from calculated I-V curves for GaInN/GaN Schottky solar cells with different values of series resistance (R_s). Efficiency calculations assumed CG device geometry for current normalization.

Additional evidence that series resistance is not a significant issue is provided by the group of I-V characteristics plotted in Figure 5.7. One of the 10 Pt VT_367 CG solar cells was illuminated with increasing "concentration" of the AM1.5G spectrum, reaching a maximum I_{SC} equal to 35x the value at 1-Sun intensity. Even at this much higher value of photo-current, the fill factor is essentially unchanged – demonstrating that the I_{ph} x R_s product is not yet large enough to impact solar cell performance.
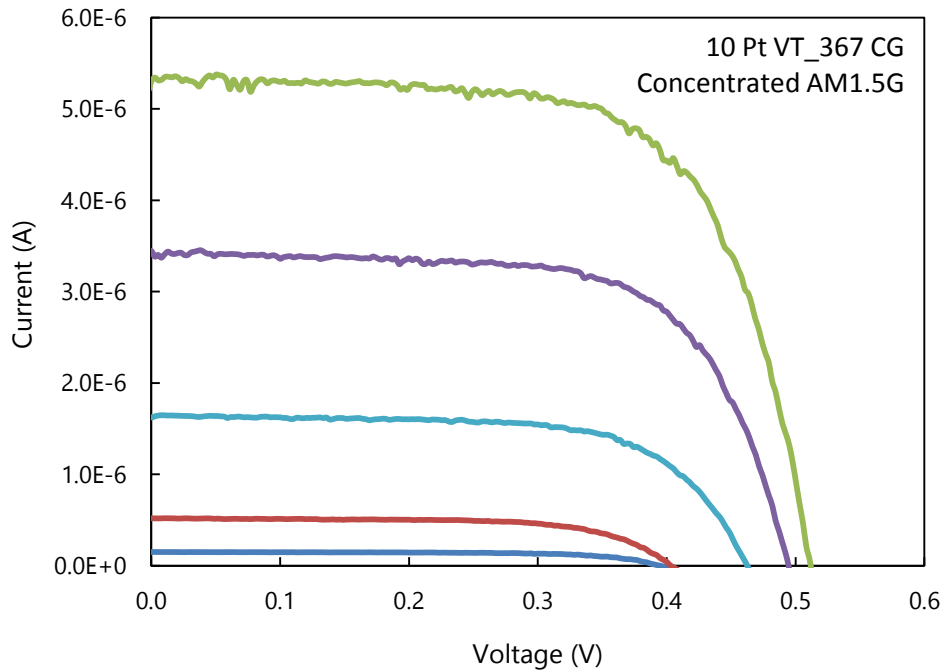
Figure 5.7. Series of I-V curves under different intensities of AM1.5G illumination. A Fresnel lens was used to focus the optical source onto the solar cell under test. These measurements were performed using the Newport solar simulator housed at MicroLink Devices.

Based on the foregoing analysis, the estimated (relatively low) values of total series resistance cannot explain the suppressed J_{SC} values observed in GaInN/GaN MQW solar cells with 5/5 Ni/Au and 5/5 Ru/Ni Schottky electrodes. These findings more firmly establish the importance of hole trapping at the NiO-to-GaN Schottky interface.

5.3 Factors Impacting V_{OC}

Another striking feature of the device parameters summarized in Table 5.1 is the large open-circuit voltage for the 5/5 RuNi VT_367 solar cell. In contrast, experimental values of V_{OC} for the 10 Pt VT_367 and 5/5 NiAu VT_367 devices are in close agreement with that found via APSYS simulation. In the following sections, consideration is given to the influence of Schottky barrier parameters and parasitic shunt resistance on the open-circuit voltage of Schottky solar cells.

5.3.1 Schottky Barrier

A useful analytical (closed-form) relationship between V_{OC} and I_{SC} for Schottky barrier solar cells can be found by combining Equations 3.8 and 3.9 and assuming that the ratio of I_{SC} to I_{sat} is much greater than unity. This condition holds for any solar cell in which I_{SC} is significantly larger than the forward dark current at $V = 0$. Rearrangement of this composite expression yields Equation 5.3 which shows a linear dependence of V_{OC} on the product of Schottky barrier height and diode ideality factor.

$$V_{OC} = n\varphi + \frac{nkT}{q}\ln\frac{I_{SC}}{ART^2} \qquad (5.3)$$

Since, I_{SC} does not change by large amounts and it only impacts V_{OC} by means of a weak logarithmic dependence, a first-order connection between open-circuit voltages and Schottky

barrier properties can be found by ignoring the second term in Equation 5.3. A comparison of experimental V_{OC} values for 10 Pt VT_367, 5/5 Ni/Au VT_367, and 5/5 Ru/Ni VT_367 solar cells against each other, and their barrier height x ideality factor products, is given in Table 5.5.

Schottky Material	n	φ (eV)	$n\varphi$	V_{OC} (V)
10 Pt	1.06	1.12 ± 0.02	1.19	0.453
5/5 Ni/Au	1.25	1.12 ± 0.04	1.40	0.461
5/5 Ru/Ni	1.78	1.06 ± 0.04	1.89	0.772

Table 5.5. Extracted V_{OC} values and barrier height x ideality factor products for each Schottky contact material.

It is noteworthy that the 5/5 RuNi VT_367 solar cell exhibits the largest V_{OC} even though its Schottky barrier height is slightly lower than those for the 10 Pt and 5/5 NiAu devices. Thus, in this case, Equation 5.3 does seem to explain the substantial increase in V_{OC} in comparison to the value predicted by APSYS simulation (which treats the Schottky barrier as ideal with $n = 1$). Unfortunately, the experimental values of V_{OC} for the 10 Pt and 5/5 Ni/Au samples are pretty similar, irrespective of their $n\varphi$ product and seem to rely only on Schottky barrier height. Some of this discrepancy may be attributable to the smaller I_{SC} observed in the 5/5 NiAu solar cell compared to the 10 Pt case; but this contribution should not be large enough to cancel out the difference in $n\varphi$ product.

5.3.2 Shunt Resistance

Parasitic high-conductance pathways connected in parallel with the solar cell proper (i.e., small values of *shunt resistance*) can in principle suppress the open-circuit voltage. This issue was explored by using Equation 5.2 to generate theoretical I-V characteristics for different values of shunt resistance (R_{sh}). As in the series resistance case, when R_{sh} becomes small enough to degrade V_{OC} it also causes a significant distortion of the entire I-V curve (and corresponding

reduction in *FF*). In this case, however I_{SC} remains unchanged. Such behavior was not observed

for any of the GaInN/GaN MQW solar cells reported herein.

6. PATHWAYS FOR IMPROVEMENT

The absolute efficiencies of GaInN/GaN Schottky solar cells presented thus far must be improved to be competitive with GaInN/GaN p-*i*-n junction designs. Deficiencies in both the short circuit current and open circuit voltage need to be addressed through optimization and application of novel techniques to increase power efficiency conversion.

6.1 Improvement of the Schottky Barrier

One pathway to improve the short circuit current is through identification of better Schottky electrode materials. An important observation coming from this research is that a NiO-to-GaN Schottky interface presents a substantial barrier to hole transport and extraction, compared to that of an ideal metal, resulting in low *CCE* and correspondingly low short-circuit current. This could be addressed by a TCO with smaller ionization potential and thus better alignment with the valence-band edge of the GaInN/GaN absorber structure.

APSYS simulations of VT_367 also suggest that enhancement of J_{SC} is possible through an increase in the Schottky barrier height. Such a change would increase the electric field through the depletion region resulting in higher *CCE*. This enhancement can be seen in Figure 6.1 where the short circuit current density increases with increasing Schottky barrier height. An increase in Schottky barrier height would also reduce the dark current and thereby increase the open-circuit voltage. This connection is also demonstrated by the J-V curves plotted in Figure 6.1.
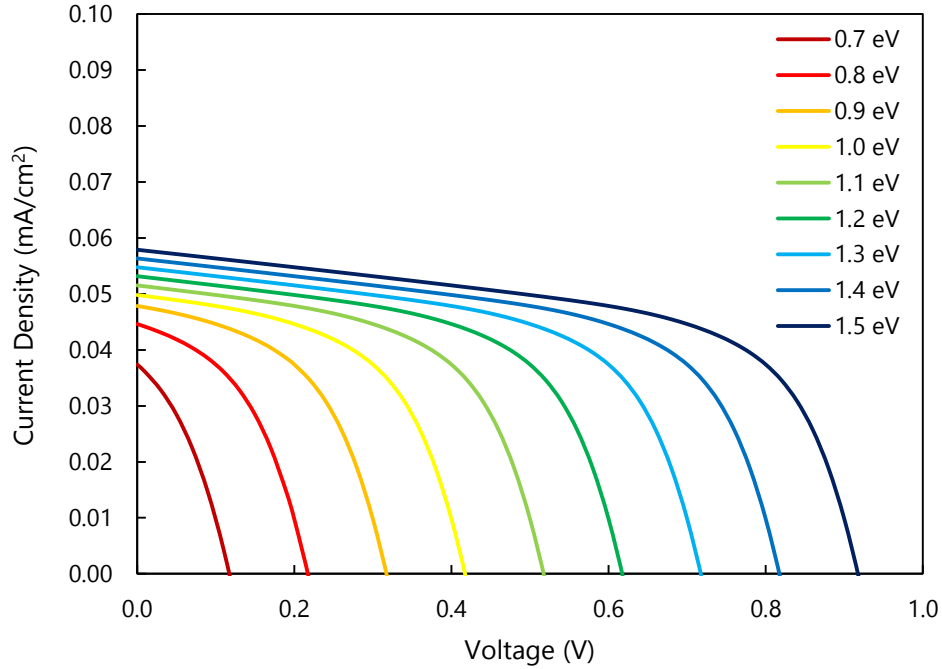
Figure 6.1. Simulated I-V curves of VT_367 under AM1.5G illumination and with the barrier height varied from 0.8 eV to 1.5 eV (with 0.1 eV stepping).

Additional enhancements to the barrier height can be realized through creation of very thin p-doped layers at the semiconductor surface. APSYS simulations were performed to verify this behavior (using GaAs due to numerical convergence issues with GaN). Figure 6.2 shows the *turn-on voltage* enhancement of a Schottky diode (top), and the same devices under solar cell illumination (bottom). These I-V curves show it may be possible to drive V_{OC} up to that of a p-n junction structure.
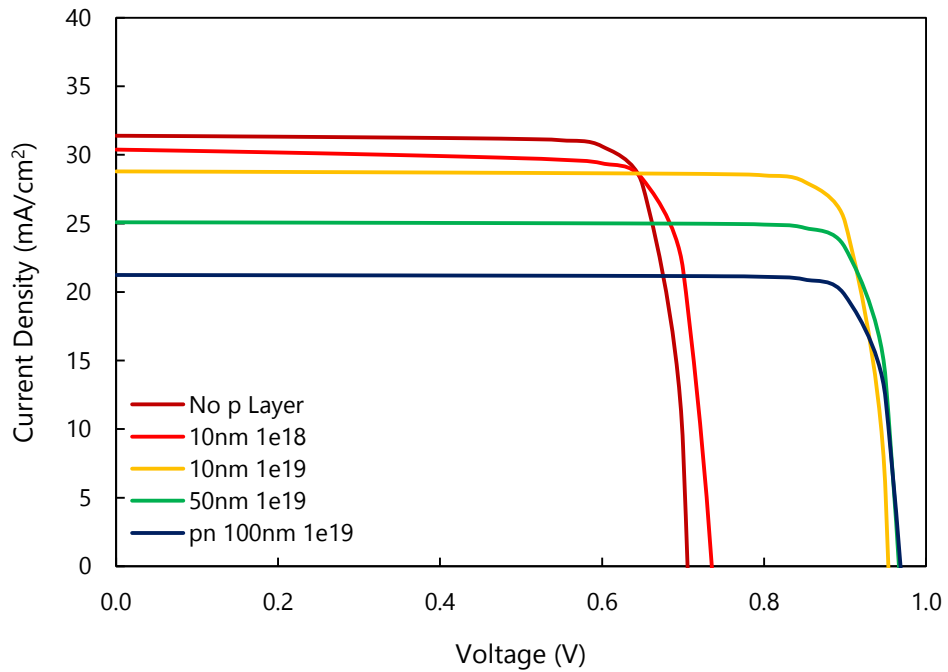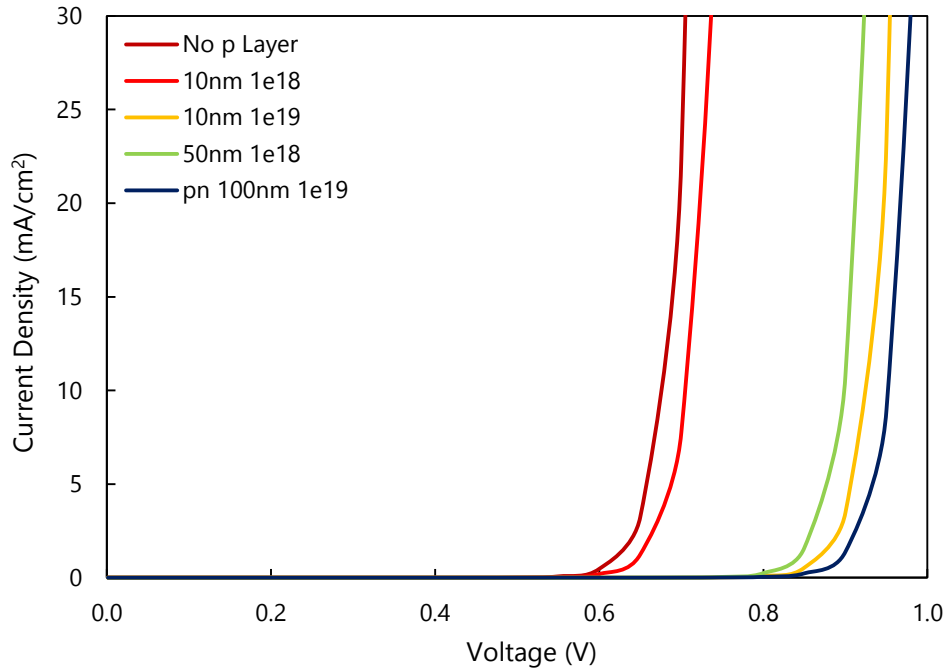
Figure 6.2. Simulated I-V curves of a forward biased GaAs Schottky diode (top) and a GaAs solar cell (bottom) assuming a 5.2 eV work function metal in contact with a thin p-layer of variable thickness and doping on a 0.5 μm thick n-type GaAs layer ($n = 5 \times 10^{16}$ cm^{-3}). The simulated I-V curve of a reference p-n diode and solar cell is also shown for comparison.

6.2 Improvement of GaInN/GaN Absorbers

Theoretical calculations indicate that VT_367 is only capable of absorbing 40% of the incident photons with energies above 3.02 eV (corresponding to the bandgap of $Ga_{0.9}In_{0.1}N$). The optical transmission spectrum for VT_367 confirms that a significant number of photons pass through the structure unabsorbed. Near-term improvements could be achieved by increasing the total thickness of the GaInN material and by increasing the indium concentration of the absorber region (the latter would result in a better bandgap match to the AM1.5G solar spectrum).

Efforts were undertaken to increase the number of QWs and raise the QW indium content of the absorbing medium. Three additional material structures were grown by Kopin Corporation (VT_365 and VT_367 were prepared in the same MOCVD reactor). The layer structures for all five GaInN/GaN samples are listed in Table 6.1.

Sample Name	Absorber Region
VT_365 DH Structure	200 nm $Ga_{0.1}In_{0.9}N$ Double Heterojunction (DH) Structure
VT_367 15x QW (Baseline Structure)	57 nm GaN + (15x 2.5 nm $Ga_{0.9}In_{0.1}N$ Quantum Wells + 14x 12 nm GaN Barriers) + 27 nm GaN
VT_391 15x QW (Repeat of 367)	57 nm GaN + (15x 2.5 nm $Ga_{0.9}In_{0.1}N$ Quantum Wells + 14x 12 nm GaN Barriers) + 27 nm GaN
VT_398 30x QW	57 nm GaN + (30x 2.5 nm $Ga_{0.9}In_{0.1}N$ Quantum Wells + 29x 12 nm GaN Barriers) + 27 nm GaN
VT_407 15x QW (Higher In Content)	57 nm GaN + (15x 2.5 nm GaInN Quantum Wells + 14x 12 nm GaN Barriers) + 27 nm GaN

Table 6.1. Absorber region structure of additional GaInN material structures grown to improve I_{SC}. For reference, the absorber region structure of VT_367 is also provided.

Based on theoretical calculations, the short circuit currents of VT_398 (more quantum wells) and VT_407 (higher indium content) should increase significantly in comparison to the reference

structure (VT_367). Sample VT_391 was included to verify material reproducibility as the growth run dates of VT_365 and VT_367 are separated from VT_391, VT_398, and VT_407 by approximately 2 years.

Schottky barrier solar cells were fabricated using each of these new GaInN/GaN material structures for comparison to 10 Pt VT_367. All of the devices were tested in house using 398 nm LED illumination to assess the quality of the GaInN/GaN MQW absorbing regions. Figure 6.3 shows I-V characteristics for the CG device geometry on 10 Pt VT_391. Unfortunately, there is a marked decrease the V_{OC}, dropping from about 0.4 V to less than 0.1 V. Furthermore, the uniformity across the sample is poor as both I_{SC} and V_{OC} span wide ranges of values and appear to be randomly distributed with respect to location on the sample.

There are two possible explanations for the large discrepancy in device performance for Pt based Schottky diodes made from VT_367 and VT_391. Either the fabrication process was carried out improperly (in the latter case) or the MOCVD process changed substantially during the two-year period of time between growth runs. Since multiple device fabrication runs have been executed using VT_367 and none of the solar cells perform as poorly as VT_391, it seems obvious that the latter explanation is correct. Nevertheless, solar cells with 10 nm thick Pt Schottky electrodes were fabricated using VT_398 and VT_407 in the hope that only growth run VT_391 was corrupted. I-V characteristics for these two devices proved to be similar to those shown in Figure 6.3, once again indicating poor material quality. Given these findings, no further work was done with VT_391, VT_398, or VT_407.
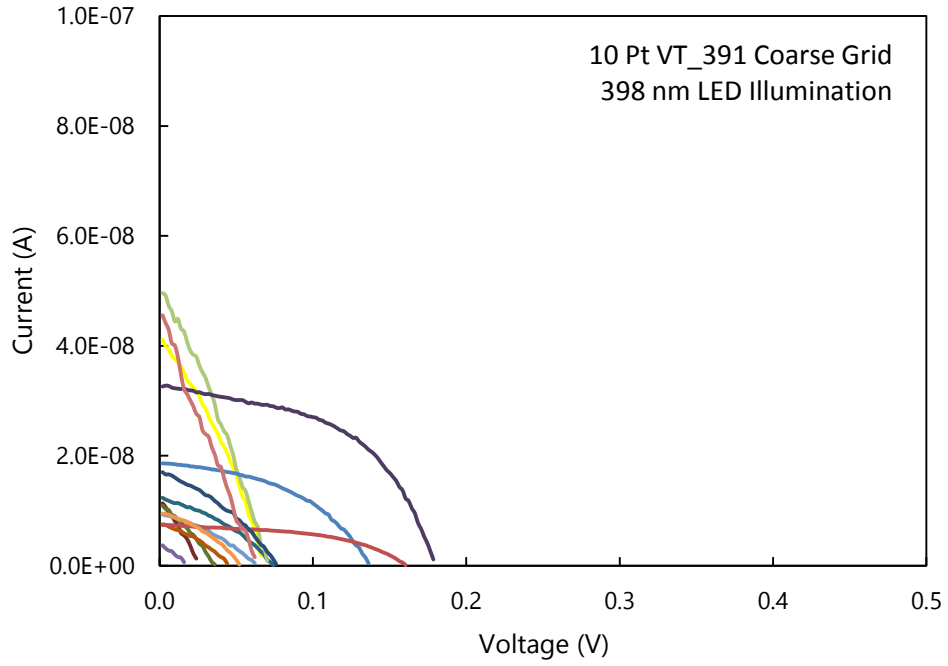
Figure 6.3. Measured I-V characteristics of the CG geometry on 10 Pt VT_391 (repeat of VT_367, baseline GaInN MQW) under 398 nm LED illumination.

7. SUMMARY AND CONCLUSIONS

Operational GaInN/GaN Schottky barrier solar cells have been demonstrated using *n-type only semiconductor layer structures* combined with three different Schottky electrode materials: *platinum* (a noble metal), *oxidized Ni/Au* (a wide bandgap semiconductor embedded with gold nanoparticles), and *oxidized Ru/Ni* (a bilayer structure in which ruthenium oxide is in direct contact with the semiconductor surface and nickel oxide serves as an encapsulation layer). Open-circuit voltages for all three solar cell types are consistent with expectations, and the trend with respect to Schottky electrode materials can be explained using a simple analytical formulation. The short-circuit currents, however, remain quite small in comparison to theoretical predictions.

Two different GaInN/GaN layer structures were evaluated one containing a MQW absorber (fifteen 2.5 nm thick $Ga_{0.9}In_{0.1}N$ quantum wells separated by sixteen 12 nm thick GaN barriers) and the other having a DH absorber (single 200 nm thick $Ga_{0.9}In_{0.1}N$ alloy layer). The DH structure was found to be of poor material quality as evidenced by the non-rectifying nature of platinum based Schottky diodes made therefrom and thus was not studied further. Two alternative device geometries were evaluated in an effort to minimize series resistance associated with the ultra-thin Schottky electrodes: a *finger*-style and a *grid*-style, each with two different pitch values (*course* = 150 μm / *fine* = 75 μm) for finger mesa separation or grid trace line spacing. The *course-grid* geometry consistently gives the highest power conversion efficiency.

The best overall solar cell presented in this work employs the GaInN/GaN MQW absorber with an oxidized 5 nm Ru / 5 nm Ni bilayer as the Schottky electrode material. Electrical testing of this device under AM1.5G illumination yields the following metrics: J_{SC} of 1.2 x 10^{-2} mA/cm^2, V_{OC} of 0.77 V, and *FF* of 0.75, resulting in conversion efficiency η of 0.007%. In comparison to

the best published results for GaInN/GaN p-*i*-n junction solar cells ($\eta = 2 - 3\%$), the efficiency for solar cells reported herein is several hundred fold smaller.

Comparing the calculated short circuit current density for VT_367 assuming 100% *CCE* under AM1.5 illumination (0.49 mA/cm^2) to the APSYS simulated J_{SC} (0.051 mA/cm^2), shows that the *CCE* is low, approximately 10% for the GaInN/GaN MQW absorber. Increasing the overlap between the internal electric field and the spatial distribution of photo-generated carriers should yield significant increases in *CCE*. Best published results have achieved peak internal quantum efficiencies of greater than 90% [34], demonstrating that a nine-fold increase in *CCE* is possible.

Calculations for J_{SC} (assuming 100% *CCE* and absorption through a Ru/Ni electrode) yield a value of $J_{SC} = 0.28$ mA/cm^2, representing the maximum theoretical J_{SC} for a Ru/Ni electrode. This approximation *does not* include effects resulting from a barrier to hole transport at the Schottky electrode–semiconductor interface. However, a value for J_{SC} (0.11 mA/cm^2) to include this effect can be derived by assuming a nine-fold improvement in the measured J_{SC} (resulting from improvements in material structure). A ratio of these two values − J_{SC} (100% *CCE*, barrier effects *not included*) / J_{SC} ("optimized" material structure, barrier effects *included*) = 2.5x − indicates that an improvement of greater than two-fold for J_{SC} can be achieved through optimization of the Schottky electrode–semiconductor interface.

Increasing the thickness of the absorbing medium should also yield significant returns. Calculations indicate that VT_367 is only capable of generating 40% of the current compared to the case of complete photon absorption. A higher indium mole fraction will also yield a better bandgap match to the AM1.5 spectrum, resulting in a larger J_{SC}. By doubling the indium

composition from 10% to 20%, an almost three fold increase in the short circuit current should be possible.

Surface roughening or the use of an anti-reflective coating to reduce reflection losses should also yield an increase in the short circuit current. Other workers have shown a 60% increase in I_{SC} by roughening the surface to reduce optical loss from surface reflection [37].

Incorporating an additional p-type (surface) doping profile as part of the device fabrication process, should lead to a two-fold gain in V_{OC}, approaching the published results for GaInN/GaN p-i-n junction devices (1.5 to 2 V). This increase in V_{OC} may also come with an increase in J_{SC}, due to increased CCE resulting from a larger electric field distributed across the depletion width.

Implementation of all of these design concepts and process techniques should yield results competitive with the best published data for p-i-n GaInN/GaN solar cells. Moreover, GaInN/GaN Schottky barrier designs consisting of only n-type semiconductors are more easily adapted for use with multi-crystalline or amorphous materials. Should mc-GaInN or a-GaInN Schottky barrier solar cells perform at levels similar to their single-crystal counterparts, a real competitor to existing Class 3 solar cell technologies would emerge, potentially revolutionizing the photovoltaic industry.

REFERENCES

[1]   US EPA (2014, August), *Sources of Greenhouse Gasses*, [online]. Available: http://www.epa.gov/climatechange/ghgemissions/sources.html

[2]   Lynch, Patrick (2014, May 12), *The "Unstable" West Antarctic Ice Sheet: A Primer*, [online]. Available: http://www.nasa.gov/jpl/news/antarctic-ice-sheet-20140512

[3]   Calculation done assuming the Earth's radius is 6378 km and the total solar energy in space as 1400 W/m^2

[4]   US Energy Information and Administration (2014, August), *International Energy Statistics*, [online]. Available http://www.eia.gov/cfapps/ipdbproject/iedindex3.cfm?tid=2&pid=2&aid=12&cid=ww,&syid=2008&eyid=2012&unit=BKWH

[5]   NREL (2014, March), Best Research Cell Efficiencies, [online]. Available: http://www.nrel.gov/ncpv/images/efficiency_chart.jpg

[6]   J. Wu, W. Walukiewicz, E. E. Haller, H. Lu, W. Schaff, Y. Saito, and Y. Nanishi, "Unusual properties of the fundamental band gap of InN," *Applied Physics Letters*, vol. 80, pp. 3967-3969, 2002.

[7]   V. Y. Davydov, A. A. Klochikhin, R. P. Seisyan, V. V. Emtsev, S. V. Ivanov, F. Bechstedt, J. Furthmuller, H. Harima, A. V. Mudryi, J. Aderhold, O. Semchinova, and J. Graul, "Absorption and Emission of Hexagonal InN. Evidence of Narrow Fundamental Band Gap," *Physica Status Solidi (b)*, vol. 229, pp. R1-R3, 2002.

[8]   Y. Nanishi, Y. Saito, and T. Yamaguchi, "RF-Molecular Beam Epitaxy Growth and Properties of InN and Related Alloys," *Japanese Journal of Applied Physics*, vol. 42, pp. 2549-2559, 2003.

[9]   G. F. Brown, J. W. Ager III, W. Walukiewicz, and J. Wu, "Numerical Simulations of Novel InGaN Solar Cells," *34th IEEE Photovoltaics Specialists Conference*, pp. 001958-001962, 2009.

[10]   J. Wu and W. Walukiewicz, "Band gaps of InN and group III nitride alloys," *Superlattices and Microstructures*, vol. 34, pp. 63-75, 2003.

[11]   J. Wu, "When group-III nitrides go infrared: New properties and perspectives," *Journal of Applied Physics*, vol. 106, pp. 011101, 2009.

[12]   J. Wu, W. Walukiewicz, K. M. Yu, W. Shan, J. W. Ager III, E. E. Haller, H. Lu, W. Schaff, W. K. Metzger, and S. Kurtz, "Superior radiation resistance of $In_{1-x}Ga_xN$ alloys: Full-solar-spectrum photovoltaic material system," *Journal of Applied Physics*, vol. 94, pp. 6477-6482, 2003.

[13]   C. Boney, I. Hernandez, R. Pillai, D. Starikov, and A. Bensaoula, "InGaN Devices for High Temperature Photovoltaic Applications," *35th IEEE Photovoltaic Specialists Conference*, pp. 002522-2527, 2010.

[14]   J. W. Ager and W. Walukiewicz, "High efficiency, radiation-hard solar cells," Lawrence Berkeley National Laboratory, Berkeley, CA, Rep. Technical Report LBNL# 56326, 2004.

[15]   D. Holec, P. M. F. J. Costa, M. J. Kappers, and C. J. Humphreys, "Critical thickness calculations for InGaN/GaN," *Journal of Crystal Growth*, vol. 303, pp. 314-317, 2007.

[16]   D. Holec, Y. Zhang, D. V. Rao, M. J. Kappers, C. McAleese, and C. J. Humphreys, "Equilibrium critical thickness for misfit dislications in III-nitrides," *Journal of Applied Physics*, vol. 104, pp. 123514, 2008.

[17]   Q. Deng, X. Wang, H. Xiao, C. Wang, H. Yin, H. Chen, D. Lin, L. Jiang, C. Feng, J. Li, Z. Wang, and X. Hou, "Comparison of as-grown and annealed GaN/InGaN : Mg samples," *Journal of Physics D: Applied Physics*, vol. 44, pp. 345101, 2011.

[18]   W. Gotz, N. M. Johnson, J. Walker, D. P. Bour, and R. A. Street, "Activation of acceptors in Mg doped GaN grown by metalorganic chemical vapor deposition," *Applied Physics Letters*, vol. 68, pp. 667-669, 1996.

[19]   D. J. Kim, D. Y. Ryu, N. A. Bojarczuk, J. Karasinski, S. Guha, S. H. Lee, and J. H. Lee, "Thermal activation energies of Mg in GaN:Mg measured by the Hall effect and admittance spectroscopy," *Journal of Applied Physics*, vol. 88, pp. 2564-2569, 2000.

[20]   C. Yang, X. Wang, H. Xiao, J. Ran, C. Wang, G. Hu, X. Wang, X. Zhang, J. Li, and J. Li, "Photovoltaic effects in InGaN structures with p-n junctions," *Physica Status Solidi (a)*, vol. 204, pp. 4288-4291, 2007.

[21]   Mahboob, I., T. D. Veal, C. F. McConville, H. Lu and W. J. Schaff, "Intrinsic Electron Accumulation at Clean InN Surfaces," *Physical Review Letters,* vol. 92, pp. 036804, 2004.

[22]   X. Chen, K. D. Matthews, D. Hao, W. J. Schaff, and L. F. Eastman, "Growth, fabrication, and characterization of InGaN solar cells," *Physica Status Solidi (a)*, vol. 205, pp. 1103-1105, 2008.

[23]   B. Cai and D. A. Drabold, "Ab initio models of amorphous InN," *Physical Review B*, vol. 79, pp. 195204, 2009.

[24]   B. Cai and D. A. Drabold, "Properties of amorphous GaN from first principles simulations," *Physical Review B*, vol. 84: pp. 075216, 2011.

[25]   E. Ahalstrom and W. W. Gartner, "Silicon Surface-Barrier Photocells," *Journal of Applied Physics*, vol. 33, pp. 2602-2606, 1962.

[26]   W. A. Anderson and A. E. Delahoy, "Schottky Barrier Diodes for Solar Energy Conversion," *Proceedings of the IEEE*, vol. 60, pp. 1457 -1458, 1972.

[27]   M. A. Green, "The depletion layer collection efficiency for pn junction, Schottky diode, and surface insulator solar cells," *Journal of Applied Physics*, vol. 47, pp. 547-554, 1976.

[28]   R. F. McQuat and D. L. Pulfrey, "A model for Schottky-barrier solar cell analysis," *Journal of Applied Physics*, vol. 47, pp. 2113-2119, 1976.

[29]   R. R. King, D. C. Law, K. M. Edmondson, C. M. Fetzner, G. S. Kinsey, H. Yoon, D. D. Krut, J. H. Ermer, R. A. Sherif, and N. H. Karam, "Advances in High-Efficiency III-V Multijunction Solar Cells", *Advances in Optoelectronics*, vol. 2007, pp. 1-8, 2007.

[30]   J.F. Geisz, Sarah R. Kurtz, M.W. Wanlass, J.S. Ward, A. Duda, D.J. Friedman, J.M. Olson, W.E. McMahon, T.E. Moriarty, J.T. Kiehl, M.J. Romero, A.G. Norman, and K.M. Jones, "Inverted GaInP / (In)GaAs / InGaAs Triple-Junction Solar Cells with Low-Stress Metamorphic Bottom Junctions", *33rd IEEE Photovoltaic Specialists Conference*, pp. 1-5, 2008.

[31]   A. G. Bhuiyan, K. Sugita, A. Hashimoto, A. Yamamoto, "InGaN Solar Cells: Present State of the Art and Important Challenges," *IEEE Journal of Photovoltaics*, vol. 2, pp. 276-293, 2012.

[32]   L. Sang, M. Liao, N. Ikeda, Y. Koide, and M. Sumiya, "Enhanced performance of InGaN solar cell by using a super-thin AlN interlayer," *Applied Physics Letters*, vol. 99, pp. 161109, 2009

[33]   M.-T. Chu, W.-Y. Liao, R.-H. Horng, T.-Y. Tsai, T.-B. Wu, S.-P. Liu, M.-H. Wu, and R.-M. Lin, "Growth and Characterization of p-InGaN/i-InGaN/n-GaN Double-Heterojunction Solar Cells on Patterned Sapphire Substrates," *IEEE Electron Device Letters*, vol. 32, pp. 922-924, 2011.

[34]   E. Matioli, C. Neufeld, M. Iza, S. Cruz, A. A. Al-Heji, X. Chen, R. M. Farrell, S. Keller, S. DenBaars, U. Mishra, S. Nakamura, S. Speck, and C. Weisbuch, "High internal and external quantum efficiency InGaN/GaN solar cells," *Applied Physics Letters*, vol. 98, pp. 021102, 2011.

[35]   J. R. Lang, C. J. Neufeld, C. A. Hurni, S. C. Cruz, E. Matioli, U. K. Mishra, and J. S. Speck, "High external quantum efficiency and fill-factor InGaN/GaN heterojunction solar cells grown by NH$_3$-based molecular beam epitaxy," *Applied Physics Letters*, vol. 98, pp. 131115, 2011.

[36]   R. Dahal, J. Li, K. Aryal, J. Y. Lin, and H. X. Jiang, "InGaN/GaN multiple quantum well concentrator solar cells," *Applied Physics Letters*, vol. 97, pp. 073115, 2010.

[37]   R. M. Farrell, C. J. Neufeld, S. C. Cruz, J. R. Lang, M. Iza, S. Keller, S. Nakamura, S. P. DenBaars, U. K. Mishra, and J. S. Speck, "High quantum efficiency InGaN/GaN multiple quantum well solar cells with spectral response extending out to 520 nm," *Applied Physics Letters*, vol. 98, pp. 201107, 2011.

[38]   T. Fujii, Y. Kuwahara, D. Iida, Y. Fujiyama, Y. Morita, T. Sugiyama, Y. Isobe, M. Iwaya, T. Takeuchi, S. Kamiyama, I. Akasaki, and H. Amanao, "GaInN-based solar cells using GaInN/GaInN superlattices," *Physica Status Solidi C*, vol. 8, pp. 2463-2465, 2011.

[39]   J.-J. Xue, D.-J. Chen, B. Liu, Z.-L. Xie, R.-L. Jiang, R. Zhang, and Y.-D. Zheng, "Au/Pt/InGaN/GaN Heterostructure Schottky Prototype Solar Cell," *Chinese Physics Letters*, vol. 26, pp. 098102, 2009.

[40]   "Electron Work Function of the Elements," in *CRC Handbook of Chemistry and Physics, 95th Edition (Internet Version 2015)*, CRC Press/Taylor and Francis, Boca Raton, FL, 2015.

[41]   J.-K. Ho, C.-S. Jong, C. C. Chiu, C.-N. Huang, C.-Y. Chen, and K.-K. Shih, "Low-resistance ohmic contacts to p-type GaN," *Applied Physics Letters*, vol. 75, pp. 1275-1277, 1999.

[42]   J.-K. Ho, C.-S. Jong, C. C. Chiu, C.-N. Huang, C.-Y. Chen, and K.-K. Shih, "Low-resistance ohmic contacts to p-type GaN achieved by the oxidation of Ni/Au films," *Journal of Applied Physics*, vol. 86, pp. 1275-1277, 1999.

[43]   L.-C. Chien, F.-R. Chen, J.-J. Kai, L. Chang, J.-K Ho, C.-S. Jong, C. C. Chiu, C.-N. Huang, C.-Y. Chen, and K.-K. Shih, "Microstructural investigation of oxidized Ni/Au ohmic contact to p-type GaN," *Journal of Applied Physics*, vol. 86, pp. 3826-3832, 1999.

[44]   W. C. Chong and K. M. Lau, "Comparison of Ni/Au, ITO, and ATO-based current spreading layers for near-ultraviolet light-emitting diodes," *Physica Status Solidi C*, vol. 4, pp. 2646-2649, 2007.

[45]   W. Mtangi, P. J. Janse van Rensburg, M. Diale, F. D. Auret, C. Nyamhere, J. M. Nel, and A. Chawanda, "Analysis of current-voltage measurements on Au/Ni/n-GaN Schottky contacts in a wide temperature range," *Material Science and Engineering B*, vol. 171, pp. 1-4, 2010.

[46]   S. Dogan, S. Duman, B. Gurbulak, S. Tuzemen, and H. Morkoc, "Temperature variation of current-voltage characteristics of Au/Ni/n-GaN Schottky diodes," *Physica E*, vol. 41, pp. 646-651, 2009.

[47]   A. Motayed, A. V. Davydov, L. A. Bendersky, M. C. Wood, M. A. Derenge, D. F. Wang, K. A. Jones, S. N. Mohammad, "High-transparency Ni/Au bilayer contacts to n-type GaN," *Journal of Applied Physics*, vol. 92, pp. 5218-5227, 2002.

[48]   H. W. Jang, and J.-L. Lee, "Transparent Ohmic contacts of oxidized Ru and Ir on p-type GaN," *Journal of Applied Physics*, vol. 93, pp. 5416-5421, 2003.

[49]   H. W. Jang, W. Urbanek, M. C. Yoo, and J.-L. Lee, "Low-resistant and high-transparent Ru/Ni ohmic contact on p-type GaN," *Applied Physics Letters*, vol. 80, pp. 2937-2939, 2002.

[50]   Z. Fan, S. N. Mohammad, W. Kim, O. Aktas, A. E. Botchkarev, K. Suzue, and H. Morkoc, "Ohmic Contacts and Schottky Barriers to n-GaN," *Journal of Electronic Materials*, vol. 25, pp. 1703-1708, 1996.

[51]   A. C. Schmitz, A. T. Ping, M. A. Khan, Q. Chen, J. W. Yang, and I. Adesida, "Metal Contacts to n-type GaN", *Journal of Electronic Materials*, vol. 27, pp. 255-260, 1998.

[52] "Electrical Resistivity of Pure Metals," in *CRC Handbook of Chemistry and Physics, 95th Edition (Internet Version 2015)*, CRC Press/Taylor and Francis, Boca Raton, FL, 2015.

[53] I. Vurgaftman and J. R. Meyer, "Band parameters for III-V compound semiconductors and their alloys," *Journal of Applied Physics*, vol. 89, pp. 5815-5874, 2001.

[54] I. Vurgaftman and J. R. Meyer, "Band parameters for nitrogen-containing semiconductors," *Journal of Applied Physics*, vol. 94, pp. 3675-3696, 2003.

[55] J. Wu, "When group-III nitrides go infrared: New properties and perspectives," *Journal of Applied Physics*, vol. 106, pp. 011101, 2009.

[56] B. Foutz, S. K. O'Leary, M. S. Shur, and L. F. Eastman, "Transient electron transport in wurtzite GaN, InN, and AlN," *Journal of Applied Physics*, vol. 85, pp. 7727-7734, 1999.

[57] Y. C. Yeo, T. C. Chong, and M. F. Li, "Electronic band structures and effective-mass parameters of wurtzite GaN and InN," *Journal of Applied Physics*, vol. 83, pp. 1429-1436, 1998.

[58] A. F. Wright, "Elastic properties of zinc-blende and wurtzite AlN, GaN, and InN," *Journal of Applied Physics*, vol. 82, pp. 2833-2839, 1997.

[59] G. F. Brown, J. W. Ager III, W. Walukiewicz, and J. Wu, "Finite element simulations of compositionally graded InGaN solar cells," *Solar Energy Materials & Solar Cells*, vol. 94, pp. 478-483, 2010.

[60] Appendix B gives a detailed listing of key phiscal parameters and equations from our customized APSYS material file.

[61] The effects of quantum confinement, spontaneous polarization, and piezoelectric polarization were not considered in this dissertation.

[62] Values of $I_{sc} = 5.0 \times 10^{-8}$ A, $I_{Sat} = 8.89 \times 10^{-12}$ A (corresponding to $\varphi = 1.1$ eV), and $n = 2.0$ were used for calculation.

APPENDIX A. DEVICE FABRICATION

All fabricated electrical, optical, and solar cell samples were fabricated at Virginia Tech in the Micron cleanroom facility. Fabrication involved the use of many tools including the Kurt Lesker PVD-250 Metal Evaporation System, Karl Suss MA-6 Mask Alignment System, Trion Reactive Ion Etcher with Inductive Plasma Etching capability, and more. Fabrication steps and recipes are outlined here in detail.

A.1 – Solar Cell Fabrication (Ni/Au Electrode Example)

Cleaning
 Acetone/IPA/DI H_2O Clean using Ultrasonic Agitation
 10 Mins in Aqua Regia (3 HCl : 1 HNO_3)
 10 Mins in HF
 DI H_2O Rinse and N_2 Dry
 10 Min Dehydrate

Create Nickel Mask for Mesa Etch
 Spin on AZ-9260, 15 sec @ 400 RPM, 45 sec @ 2000 RPM
 Softbake at 124 ℃ setting (surface at 115 ℃) on Hotplate for 3.5 Mins
 Expose using Mesa Mask
  Clear at Mesa, Opaque else where
  12.2 mW/cm^2 for 38 seconds
 Develop in 3 H_2O : 1 AZ400k Developer
 Do a quick descum using one of the following
  5 seconds in SAMCO
  15 seconds in Asher
 Deposit 2000A of Ni
 Liftoff with Acetone and clean sample with Acetone/IPA/DI H_2O

Etch Sample
 Run RIE Clean for 10 mins
 Run Etch on dummy Si sample for 5 mins
 Run RIE Clean for 10 mins
 Etch Sample using RIE
  Pressure 12 mTorr
  ICP 300W
  RIE 100W
  BCl_3 20 sccm
  Cl_2 10 sccm
 Target Etch Depth – 10000A
  Past results: 6250A in 438 seconds using a Ni mask (~850 A/min)
  Past results: 9500A in 887 seconds using a Ni mask (~650 A/min)

Remove sample from Coolgrease and clean with Acetone/IPA/DI H_2O
5 Mins in Aqua Regia (3 HCl : 1 HNO_3)
5 Mins in Acetone w/ Ultrasonic
5 Mins in Aqua Regia (3 HCl : 1 HNO_3)
5 Mins in Acetone w/ Ultrasonic
Clean with Acetone/IPA/DI H_2O
10 Min Dehydrate

Deposit Ohmic Contact
Spin on AZ-9260, 15 sec @ 400 RPM, 45 sec @ 2000 RPM
Softbake at 124 ℃ setting (surface at 115 ℃) on Hotplate for 3.5 Mins
Expose using Ohmic Contact Mask
Clear at contact pads, Opaque else where
12.2 mW/cm^2 for 38 seconds
Develop in 3 H_2O : 1 AZ400k Developer
Do a quick descum using one of the following
5 seconds in SAMCO
15 seconds in Asher
30 Second Buffered Oxide Etch Dip
Deposit 300A of Ti, 4000A of Al
Liftoff with Acetone and clean sample with Acetone/IPA/DI H_2O
Anneal for 600 ℃, 5 mins in H-Ar balanced forming gas.

Deposit Transparent Conducting Oxide
Spin on AZ-9260, 15 sec @ 400 RPM, 45 sec @ 2000 RPM
Softbake at 124 ℃ setting (surface at 115 ℃) on Hotplate for 3.5 Mins
Expose using TCO Contact Mask
Clear at slightly smaller than mesa, Opaque else where
12.2 mW/cm^2 for 42 seconds
Develop in 3 H_2O : 1 AZ400k Developer
Do a quick descum using one of the following
5 seconds in SAMCO
15 seconds in Asher
30 Second Buffered Oxide Etch Dip
Deposit 50A of Ni, 50A of Au
Liftoff with Acetone and clean sample with Acetone/IPA/DI H_2O
Anneal for 500 ℃, 10 mins in Air

Deposit Top Ni Conducting Metal
Spin on AZ-9260, 15 sec @ 400 RPM, 45 sec @ 2000 RPM
Softbake at 124 ℃ setting (surface at 115 ℃) on Hotplate for 3.5 Mins
Expose using Top Contact Mask
Clear at slightly smaller than mesa, Opaque else where
12.2 mW/cm^2 for 38 seconds
Develop in 3 H_2O : 1 AZ400k Developer
Do a quick descum using one of the following
15 seconds in Asher
Deposit 500A of Ni, 4000A of Ag
Liftoff with Acetone and clean sample with Acetone/IPA/DI H_2O

A.2 – TLM Pattern Fabrication (Ni/Au Electrode Example)

Processing Overview for Transparent Conducting Oxides TLM Patterns

Cleaning

        Acetone/IPA/DI H_2O Clean using Ultrasonic Agitation
        10 Mins in Aqua Regia (3 HCl : 1 HNO_3)
        10 Mins in HF
        DI H_2O Rinse and N_2 Dry
        10 Min Dehydrate

Create Nickel Mask for Mesa Etch

        Spin on AZ-9260, 15 sec @ 400 RPM, 45 sec @ 2000 RPM
        Softbake at 124 ºC setting (surface at 115 ºC) on Hotplate for 3.5 Mins
        Expose using Mesa Mask, 12.2 mW/cm^2 for 38 seconds
        Develop in 3 H_2O : 1 AZ400k Developer
        Quick descum, 10 seconds in Asher
        Deposit 1500A of Ni (at < 3 A/sec, ~2e-6 Torr)
        Liftoff with Acetone (and soak in Acetone for 5+ mins)
        Gently clean sample with Acetone/IPA/DI H_2O

Etch Sample

        Run RIE Clean for 10 mins
        Run Etch on dummy Si sample for 5 mins
        Run RIE Clean for 10 mins
        Etch Sample using RIE

Pressure	12 mTorr
ICP	300W
RIE	100W
BCl_3	20 sccm
Cl_2	10 sccm
Time	1200s
Past results: ~6000A using a Ni mask (~300 A/min)	

        5 Mins in Aqua Regia (3 HCl : 1 HNO_3)
        5 Mins in Acetone w/ Ultrasonic
        5 Mins in Aqua Regia (3 HCl : 1 HNO_3)
        5 Mins in Acetone w/ Ultrasonic
        Clean with Acetone/IPA/DI H_2O
        10 Min Dehydrate

Deposit Transparent Conducting Oxide

        Spin on AZ-9260, 15 sec @ 400 RPM, 45 sec @ 2000 RPM
        Softbake at 124 ºC setting (surface at 115 ºC) on Hotplate for 3.5 Mins
        Expose using TCO Contact Mask, 12.2 mW/cm^2 for 38 seconds
        Develop in 3 H_2O : 1 AZ400k Developer
        Quick descum, 10 seconds in Asher
        30 Second BOE Dip
        Deposit 100A of Ni (D: 8.91, Z: 0.331), 100A of Au (D: 19.30, Z: 0.381) @ ~1 A/sec, ~2e-6 Torr
        Liftoff with Acetone (Let it soak for 5+ mins in Acetone)
        Clean sample very well with Acetone/IPA/DI H_2O

Anneal for 500 ºC, 3 mins in Air

Deposit Top Ni Conducting Metal
        Spin on AZ-9260, 15 sec @ 400 RPM, 45 sec @ 2000 RPM
        Softbake at 124 ºC setting (surface at 115 ºC) on Hotplate for 3.5 Mins
        Expose using Top Contact Mask, 10 mW/cm^2 for 42 seconds
        Develop in 3 H$_2$O : 1 AZ400k Developer
        NO DESCUM, NO HCl/BOE DIP
        Deposit 500A of Ni (D: 8.91, Z: 0.331) @ < 3 A/sec, ~2e-6 Torr,
                4000A of Ag (D: 10.50, Z: 0.529) @ < 5 A/sec, ~2e-6 Torr
        Liftoff with Acetone and clean sample with Acetone/IPA/DI H$_2$O

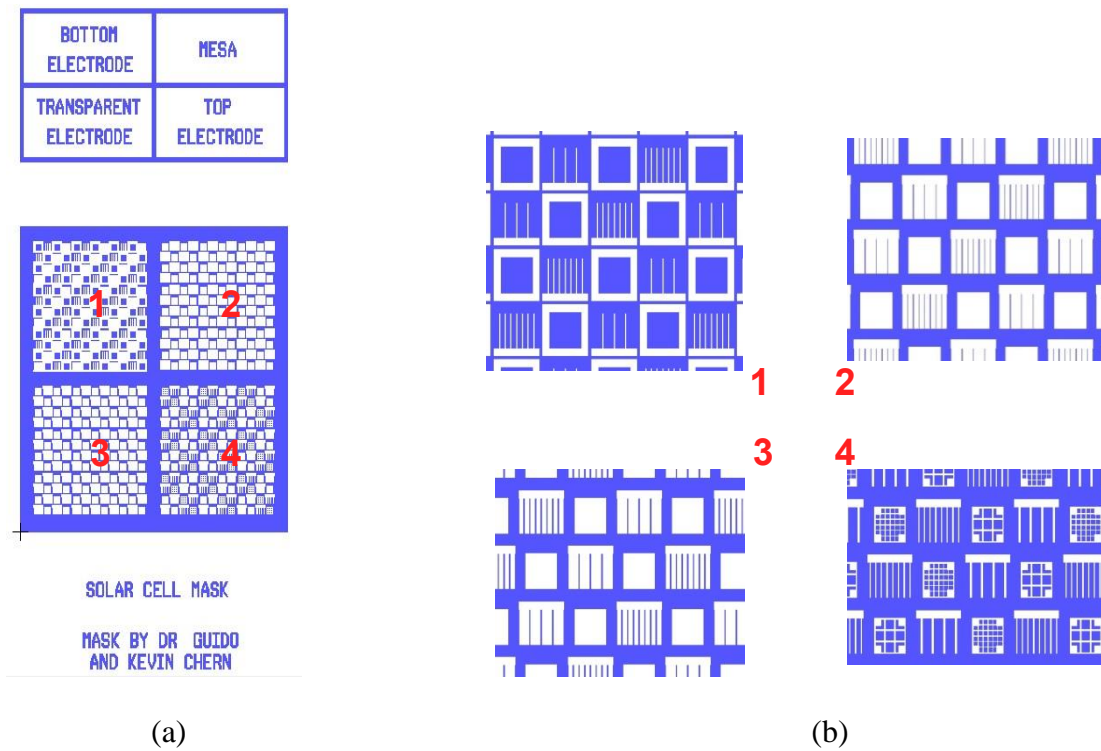## A.3 – Solar Cell Fabrication Photolithographic Mask

(a)

(b)

Figure A.1. Picture of mask as seen in L-Edit by Tanner Tools with a close up of each individual field. Mask was printed by Advance Reproductions on a 4" soda-lime plate for photolithography. Blue areas are opaque while white areas are transparent.

APPENDIX B – APSYS GAINN SIMULATION MATERIAL FILE

The default Apsys material file for GaInN had a few outdated parameters, most notably the end point for InN was still set to 1.6 eV and the absorption coefficients were noticeably lower than published literature ($\sim 10^3$ cm^{-1}). This custom material file for GaInN pulls together the generally accepted best material parameters from multiple review articles [9, 53-59], compiled into one material file for simulation in Apsys.

```
$ Revised macro for In(x)Ga(1-x)N w/ absorption
begin_macro ingan_revised
material type=wurtzite band_valleys=(1 1) &&
 el_vel_model=beta hole_vel_model=beta
$
$ - Lattice Parameter
$   Vegard's Law (Linear Relationship)
$   GaN = 3.189 A
$   InN = 3.545 A
$
$   Assume material is grown strained on GaN (3.189)
$
lattice_base value=3.189
lattice_bulk variation=function
function(x,temper)
3.189*(1-x)+3.545*x
end_function
$
$ - Bandgap (w/ Varshni Formula)
$   Eg = Eg0 - [ alpha/(T+beta) * T^2 ]
$
$   GaN = 3.51 (@ 0K), 3.503 (@ 300K)
$       alpha = 0.909e-3
$       beta = 830
$   InN = 0.78 (@ 0K), 0.778 (@ 300K)
$       alpha = 0.245e-3
$       beta = 624
$
$   Bowing Parameter = 1.4
$
eg0_bulk variation=function
function(x,temper)
eg0gan=3.51;
eg0inn=0.78;
eg0gan_alpha=0.909d-3;
eg0gan_beta=830;
eg0inn_alpha=0.245d-3;
eg0inn_beta=624;
eggan=eg0gan-eg0gan_alpha*temper**2/(eg0gan_beta+temper);
eginn=eg0inn-eg0inn_alpha*temper**2/(eg0inn_beta+temper);
```

```
bowing=1.4;
(1.0-x)*eggan+eginn*x-bowing*x*(1-x)
end_function
$
$ - Bulk Wurtzite Valence Band Effective Mass Parameters
$   Using Vegard's Law for Interpolation
$         GaN  ,  InN
$   A1 =  -7.21, -8.21
$   A2 =  -0.44, -0.68
$   A3 =   6.68,  7.57
$   A4 =  -3.46, -5.23
$   A5 =  -3.40, -5.11
$   A6 =  -4.90, -5.96
$   A7 = 0.0937,    0   (May not be implemented/used)
$
a1_bulk variation=function
function(x,temper)
inn=-8.21;
gan=-7.21;
gan+(inn-gan)*x
end_function
$
a2_bulk variation=function
function(x,temper)
inn=-0.68;
gan=-0.44;
gan+(inn-gan)*x
end_function
$
a3_bulk variation=function
function(x,temper)
inn=7.57;
gan=6.68;
gan+(inn-gan)*x
end_function
$
a4_bulk variation=function
function(x,temper)
inn=-5.23;
gan=-3.46;
gan+(inn-gan)*x
end_function
$
a5_bulk variation=function
function(x,temper)
inn=-5.11;
gan=-3.4;
gan+(inn-gan)*x
end_function
$
a6_bulk variation=function
function(x,temper)
inn=-5.96;
gan=-4.9;
gan+(inn-gan)*x
end_function
$
```

```
$a7_bulk variation=function
$function(x,temper)
$inn=0;
$gan=0.0937;
$gan+(inn-gan)*x
$end_function
$
$ - Wurtzite Energy Parameter in eV
$   Using Vegard's Law for Interpolation
$                                 GaN    , InN
$   delta1 (delta_cr)        0.0100, 0.0400
$   delta2 (1/3rd delta_so)  0.0057, 0.0017
$   delta3 (delta2)          0.0057, 0.0017
$
delta1_bulk variation=function
function(x,temper)
gan=0.010;
inn=0.040;
gan+(inn-gan)*x
end_function
$
delta2_bulk variation=function
function(x,temper)
gan=0.0057;
inn=0.00017;
gan+(inn-gan)*x
end_function
$
delta3_bulk variation=function
function(x,temper)
gan=0.0057;
inn=0.00017;
gan+(inn-gan)*x
end_function
$
$ - Wurtzite Conduction Band Effective Mass
$   Using Vegard's Law for Interpolation
$
$   mass_gamma_bulk (parallel to c-axis)
$     GaN = 0.20, InN = 0.07
$   tmass_gamma_bulk (perpendicular to c-axis)
$     GaN = 0.20, InN = 0.07
$
mass_gamma_bulk variation=function
function(x)
gan=0.20;
inn=0.07;
gan+(inn-gan)*x
end_function
$
tmass_gamma_bulk variation=function
function(x)
gan=0.20;
inn=0.07;
gan+(inn-gan)*x
end_function
$
```

94

```
$ - Wurtzite Sheer Deformation Potential
$   Using Vegard's Law for Interpolation
$
$   a  (interband), total hydrostatic deformation potential in eV
$   ac (=1/2a), conduction part of hydrostatic deformation potential
$   a1 combined hydrostatic deformation potentials
$      for transitions between conduction and valence bands
$   a2 combined hydrostatic deformation potentials
$      for transitions between conduction and valence bands
$
$   Need to verify a = a1, ac = a2 (probably not true)
$
$   D1-D6 Deformation Potential Constants
$              GaN  , InN
$   a  (a1) =  -4.90, -3.50
$   ac (a2) = -11.30, -3.50
$   D1 =       -3.70, -3.70
$   D2 =        4.50,  4.50
$   D3 =        8.20,  8.20
$   D4 =       -4.10, -4.10
$   D5 =       -4.00, -4.00   (May not be implemented/used)
$   D6 =       -5.50, -5.50   (May not be implemented/used)
$
d1_bulk variation=function
function(x,temper)
gan=-3.7;
inn=-3.7;
gan+(inn-gan)*x
end_function
$
d2_bulk variation=function
function(x,temper)
gan=4.5;
inn=4.5;
gan+(inn-gan)*x
end_function
$
d3_bulk variation=function
function(x,temper)
gan=8.2;
inn=8.2;
gan+(inn-gan)*x
end_function
$
d4_bulk variation=function
function(x,temper)
gan=-4.1;
inn=-4.1;
gan+(inn-gan)*x
end_function
$
a_bulk variation=function
function(x,temper)
gan=-4.9;
inn=-3.5;
gan+(inn-gan)*x
end_function
```

```
$
ac_bulk variation=function
function(x,temper)
gan=-11.3;
inn=-3.5;
gan+(inn-gan)*x
end_function
$
$ - Wurtzite Elastic Stiffness Constant
$   Using Vegard's Law for Interpolation
$
$        GaN, InN
$   c11  390, 223   (May not be implemented/used)
$   c12  145, 115   (May not be implemented/used)
$   c13  106,  92
$   c33  398, 224
$   c44  105,  48   (May not be implemented/used)
$
c13_bulk variation=function
function(x,temper)
gan=106;
inn=92;
gan+(inn-gan)*x
end_function
$
c33_bulk variation=function
function(x,temper)
gan=398;
inn=224;
gan+(inn-gan)*x
end_function
$
$c11_bulk variation=function
$function(x,temper)
$gan=390;
$inn=223;
$gan+(inn-gan)*x
$end_function
$
$c12_bulk variation=function
$function(x,temper)
$gan=145;
$inn=115;
$gan+(inn-gan)*x
$end_function
$
$c44_bulk variation=function
$function(x,temper)
$gan=105;
$inn=48;
$gan+(inn-gan)*x
$end_function
$
$ - End Wurtzite Parameters
$ - Begin Electronic Material Paramters
$
$ - Diaelectric Constant
```

```
$    Using Vegard's Law for Interpolation
$
$    GaN = 10.5, InN = 8.9
$
dielectric_constant variation=function
function(x,temper)
gan=10.5;
inn=8.9;
gan+(inn-gan)*x
end_function
$
$ - Electron Affinity
$    GaN Electron Affinity = 4.07
$    Valence band offset GaN/InN = -0.50 eV
$    Bowing = 1.4
$    Assume VBO is linearly related to x
$
affinity variation=function
function(x,temper)
eg0gan=3.51;
eg0inn=0.78;
eg0gan_alpha=0.909d-3;
eg0gan_beta=830;
eg0inn_alpha=0.245d-3;
eg0inn_beta=624;
eggan=eg0gan-eg0gan_alpha*temper**2/(eg0gan_beta+temper);
eginn=eg0inn-eg0inn_alpha*temper**2/(eg0inn_beta+temper);
bowing=1.4;
egx=(1.0-x)*eggan+eginn*x-bowing*x*(1-x);
$
vbo=0.50*x;
gan=4.07;
gan+(eggan-egx-vbo)
end_function
$
$ Using Walukewicz's parameters for absorption
$ coeffcient as a function of composition
$
$  x        a         b
$  1        0.69642   0.46055
$  0.83     0.66796   0.68886
$  0.69     0.58108   0.66902
$  0.57     0.60946   0.62182
$  0.5      0.51672   0.46836
$  0        0.35217   -0.6571
$
absorption variation=function
function(x,temper,wavelength)
$
ephoton=1.24/wavelength;
$
eg0gan=3.51;
eg0inn=0.78;
eg0gan_alpha=0.909d-3;
eg0gan_beta=830;
eg0inn_alpha=0.245d-3;
eg0inn_beta=624;
```

```
eggan=eg0gan-eg0gan_alpha*temper**2/(eg0gan_beta+temper);
eginn=eg0inn-eg0inn_alpha*temper**2/(eg0inn_beta+temper);
bowing=1.4;
abs_bandgap=(1.0-x)*eggan+eginn*x-bowing*x*(1-x);
$
if (x<0)
a_abs=3.52517;
b_abs=-0.6571;
else (x<0.5)
a_abs=0.51672;
b_abs=0.46836;
else (x<0.57)
a_abs=0.60946;
b_abs=0.62182;
else (x<0.69)
a_abs=0.58108;
b_abs=0.66902;
else (x<0.83)
a_abs=0.66796;
b_abs=0.68886;
else
a_abs=0.69642;
b_abs=0.46055;
endif
k=a_abs*(ephoton-abs_bandgap)+b_abs*((ephoton-abs_bandgap)**2)
if (k<0)
k=0
endif
1e7*(k**0.5)
end_function
$
$   Electron mobility parameters
$   Mostly from Walukiewicz Group
$                                GaN                 InN
$   u_e_max (max_electron_mob)   55 cm2V-1s-1        30 cm2V-1s-1
$   u_e_min (min_electron_mob)   1000 cm2V-1s-1      1100 cm2V-1s-1
$   gamma_e (alpha_n)            1                   1
$   Ng_e (electron_ref_dens)     2e17 cm-3           3e18 cm-3
$   u_h_max (max_hole_mob)       170                 170
$   u_h_min (min_hole_mob)       3                   3
$   gamma_h (alpha_p)            2                   2
$   Ng_h (hole_ref_dens)         3e17 cm-3           3e17 cm-3
$
max_electron_mob variation=function
function(x,temper)
gan=1000d-4;
inn=1100d-4;
gan+(inn-gan)*x
end_function
$
min_electron_mob variation=function
function(x,temper)
gan=55d-4;
inn=30d-4;
gan+(inn-gan)*x
end_function
$
```

```
alpha_n value=1
beta_n value=1.
$
electron_ref_dens variation=function
function(x,temper)
gan=2e23;
inn=3e24;
gan+(inn-gan)*x
end_function
$
max_hole_mob value=170d-4
min_hole_mob value=3d-4
alpha_p value=2
beta_p value=1.
hole_ref_dens value=3e23
$
lifetime_n value=1.e-9
lifetime_p value=1.e-9
$
radiative_recomb value=1d-15
$
$ - Leftover constants from previous definitions
$
electron_sat_vel value=1.d5
hole_sat_vel value=1.d5
norm_field value=2.1e7
tau_energy value=1.d-13
auger_n value=1.d-46
auger_p value=1.d-46
$
real_index variation=function
function(x,temper)
gan=2.5067;
inn=3.4167;
gan+(inn-gan)*x
end_function
$
$ rough estimate for thin layers:
thermal_kappa value=10.
$
end_macro ingan_revised
```